Quaternary ammonium cations are a useful tool to investigate viral potassium channels

Vom Fachbereich Biologie der Technischen Universität Darmstadt

zur Erlangung des akademischen Grades

eines Doctor rerum naturalium

genehmigte Dissertation von

M. Sc. Tobias Winterstein

aus Darmstadt

1. Referent: Prof. Dr. Gerhard Thiel
2. Referent: Prof. Dr. Adam Bertl

Darmstadt 2019

TECHNISCHE
UNIVERSITÄT
DARMSTADT

Winterstein, Tobias: Quaternary ammonium cations are a useful tool to investigate viral potassium channels

Darmstadt, Technische Universität Darmstadt
Jahr der Veröffentlichung der Dissertation auf TUprints: 2020
URN: urn:nbn:de:tuda-tuprints-113240
Tag der mündlichen Prüfung: 09.12.2019

Success is the ability
to go from one failure to another
with no loss of enthusiasm.

Winston Churchill

Table of Contents

Summary

Potassium channels enable the selective and passive transport of potassium ions through membranes. They are involved in a variety of cellular and physiological processes. These include the contraction of muscle cells or the generation and transmission of action potentials. It is therefore of interest to elucidate the structure and function of these proteins. In this work, viral potassium channels of the ATCV-1 family are used for an analysis of structure function correlates. The monomers of these channels are with 82 amino extremely small but represent in spite of their miniature size still the most important structural and functional features of the pore module of complex potassium channels.

In the first part of this thesis structural differences of the two channels Kcv_{NTS} and Kcv_{S} are investigated with the help of quaternary ammonium cations (QA). Despite a sequence identity of 90%, these two channels show electrophysiological differences. These differences are due to an inner gate in Kcv_{S}, which produces long-lived closed phases and thus significantly reduces the open probability. This gate is mediated by an intrahelical hydrogen bridge of Ser^{77}. Intracellularly added QAs cause in planar lipid bilayer recordings of both channels a voltage-dependent block, which becomes slower with increasing size of the blocker. The analysis of single channel gating in absence and presence of different QA blockers shows that the affinity of Kcv_{S} is twice as high as that of Kcv_{NTS}. It can be shown that this difference is due to the inner gate, which is apparently able to trap the QAs in the cavity through the aromatic side chain. Due to the minor differences in the association rate constants between different blockers of the two channels, no conclusions can be drawn about the pore diameter.

Goal of the second part was the engineering of a light switchable viral K^+ channel by modular design. The molecule MAL-AZO-QA was bound to the Kcv_{NTS} channel by means of a maleimide bond. As a result, the charged head group should be able to block the channel in a light dependent manner. In a first step sensitivity of the channel towards Tetraethylammonium (TEA) was increased by specific mutations just outside of the selectivity filter. The consequent reduction of unitary conductance was in the next step significantly increased by a further mutation just below the filter region in the area of the cavity. In the next step the amino acid cysteine was introduced into the protein at various positions within the extracellular loop. This should ensure coupling of the light-switchable molecule to the channel at an appropriate distance to the pore. While all these preparatory steps were successful it was not possible to find the expected light sensitive blocking of the channel.

The third part of the project was dedicated to a methodological improvement of the lipid bilayer technique. In this context we examined the advantages and disadvantages of photolithographic generated pores in the epoxide ADEX as septum for lipid bilayer experiments. The functional properties of these pores for channels recording were compared to conventional septa generated in Teflon foils. The data show that the functional properties of the Kcv_{NTS} channels as a test system are identical in both septa. While the photolithographic technique allowed the generation of apertures with diameters as small as 30 µm they provided no advantages in terms of capacity or signal-to-noise ratio over larger apertures with 100 µm in Teflon. However, the advantages of the ADEX films are that they can be cleaned with acetone for frequent reuse. Even more beneficial is the observation that they are more suitable for long-term measurements since the stability of the bilayer is not compromised by pipetting of the measuring solution.

Zusammenfassung

Kaliumkanäle ermöglichen den selektiven und passiven Transport von Kaliumionen über Membranen. Sie sind an einer Vielzahl von zellulären und physiologischen Prozessen beteiligt. Dazu gehören die Kontraktion von Muskelzellen oder die Erzeugung und Übertragung von Aktionspotenzialen. Es ist daher von Interesse, die Struktur und Funktion dieser Proteine aufzuklären. In dieser Arbeit werden virale Kaliumkanäle der ATCV-1-Familie für eine Analyse von Struktur und Funktion verwendet. Die Monomere dieser Kanäle sind mit 82 Aminosäuren extrem klein, stellen aber trotz ihrer geringen Größe immer noch die wichtigsten strukturellen und funktionellen Merkmale des Porenmoduls komplexer Kaliumkanäle dar.

Im ersten Teil dieser Arbeit werden strukturelle Unterschiede der beiden Kanäle Kcv_{NTS} und Kcv_S mit Hilfe von quaternären Ammoniumkationen (QAs) untersucht. Trotz einer Sequenzidentität von 90% zeigen diese beiden Kanäle elektrophysiologische Unterschiede. Diese Unterschiede sind auf ein inneres Gate in Kcv_S zurückzuführen, das langlebige geschlossene Phasen erzeugt und damit die Offenwahrscheinlichkeit deutlich reduziert. Dieses Gate wird durch eine intrahelikale Wasserstoffbrücke von Ser^{77} vermittelt. Intrazellulär zugegebene QAs bewirken im planaren Lipid-Bilayer bei beiden Kanälen einen spannungsabhängigen Block, der mit zunehmender Größe des Blockers langsamer wird. Die Analyse des Kanalschaltens in Abwesenheit und Anwesenheit verschiedener QA-Blocker zeigt, dass die Affinität von Kcv_S doppelt so hoch ist wie die von Kcv_{NTS}. Es kann gezeigt werden, dass dieser Unterschied auf das innere Gate zurückzuführen ist, das anscheinend in der Lage ist, die QAs durch die aromatische Seitenkette in der Kavität einzufangen. Aufgrund der geringen Unterschiede in den Assoziationsratenkonstanten zwischen den verschiedenen Blockern der beiden Kanäle können keine Rückschlüsse auf den Porendurchmesser gezogen werden.

Ziel des zweiten Teils war die Entwicklung eines lichtschaltbaren viralen Kaliumkanals in Modulbauweise. Das Molekül MAL-AZO-QA wurde über eine Maleimidbindung an Kcv_{NTS} gebunden. Daher sollte die geladene Kopfgruppe in der Lage sein den Kanal lichtabhängig zu blockieren. In einem ersten Schritt wurde die Empfindlichkeit des Kanals gegenüber Tetraethylammonium (TEA) durch spezifische Mutationen außerhalb des Selektivitätsfilters erhöht. Die damit verbundene Reduktion der Leitfähigkeit wurde im nächsten Schritt durch eine weitere Mutation unmittelbar unterhalb der Filterregion im Bereich der Kavität signifikant erhöht. Im nächsten Schritt wurde die Aminosäure Cystein an verschiedenen Stellen innerhalb des extrazellulären Loops in das Protein eingebracht. Dadurch sollte die Kopplung des lichtschaltbaren Moleküls an den Kanal in einem angemessenen Abstand zur Pore

gewährleistet sein. Obwohl alle diese Vorbereitungsschritte erfolgreich waren, war es nicht möglich, die erwartete lichtempfindliche Blockierung des Kanals zu erreichen.

Der dritte Teil des Projekts widmete sich einer methodischen Verbesserung der Lipid-Bilayer-Technik. In diesem Zusammenhang wurden die Vor- und Nachteile photolithographisch erzeugter Poren im Epoxid ADEX als Septum für Lipid-Bilayer untersucht. Die funktionellen Eigenschaften dieser Poren wurden mit konventionellen Septen aus Teflonfolie verglichen. Die Daten zeigen, dass die funktionellen Eigenschaften von Kcv_{NTS} als Testsystem in beiden Septen identisch sind. Während die photolithographische Technik die Erzeugung von Aperturen mit Durchmessern von nur 30 µm erlaubte, boten sie gegenüber größeren Aperturen mit 100 µm in Teflon keine Vorteile in Bezug auf Kapazität oder Signal-Rausch-Verhältnis. Die Vorteile der ADEX-Folien liegen jedoch darin, dass sie bei häufiger Wiederverwendung mit Aceton gereinigt werden können. Noch vorteilhafter ist die Beobachtung, dass sie für Langzeitmessungen besser geeignet sind, da die Stabilität der Membran durch das Pipettieren der Messlösung nicht beeinträchtigt wird.

1 General Introduction

1.1 Cell membranes

The cell membrane, also called plasma- or cytoplasmic membrane, is a biological membrane that separates the inside of the cell from the environment (Singleton, 1999). It consists of a lipid bilayer and integrated proteins. The task of the lipid bilayer is to separate the distinct milieu of the cytoplasm from the external solution. The composition of the phospholipid bilayer is variable and changes depending on the environment and during the different phases of the cell cycle. In particular, cholesterol levels fluctuate for example in primary human neuronal cell membranes and influence fluidity during developmental stages (Noutsi et al., 2016). Three classes of amphipathic lipids; phospholipids, glycolipids and sterols are the main components of the cell membrane. The amount of each component varies depending on the cell type, but most of the dominating component are usually phospholipids with more than 50% (Lodish et al., 2000a). The membrane consists only to 2% of glycolipids, the rest are sterols. Only about 40% of the volume of the cell membrane consists of lipids; proteins take up to 60%. While the outer mitochondrial membrane consists of 48% lipids and 52% proteins, the inner mitochondrial membrane has a significantly different composition. Here, only a quarter of the volume are lipids and three quarters are proteins (Comte et al., 1976). Also, the same membrane in different organisms can differ in composition. In the case of liver cells of rats and mice, the membrane of rats comprises 42% lipid, while that of mice is 54% (Ray et al., 1969).

Membrane proteins are responsible for many biological activities. They are involved in various cellular processes such as cell adhesion, ion transport or cell-cell signal transduction. For example, one third of all genes in yeasts code for membrane proteins (Lodish et al., 2000b). Integral- or transmembrane proteins cross the membrane. Many of them can interact with cytosolic molecules. Important parts of membrane proteins are built of hydrophobic domains, which are located inside the membrane. In the case of proteins in the plasma membrane these hydrophobic domains exhibit mainly as an α-helical fold. Furthermore, membrane proteins often also contain a hydrophilic extracellular domain with which they can get into contact with external molecules. Examples for transmembrane proteins with these structural features are ion channels, ATPases or G-protein coupled receptors. One example is the gamma-aminobutyric acid (GABA), which is the endogenous ligand for $GABA_A$ receptors and plays a major role as an inhibitory transmitter in the central nervous system (Wu et al., 2015).

Another class of structural membrane proteins are lipid-bound proteins. They are covalently bound to one or more lipid molecules, which in turn are anchored to the membrane. The protein itself is not in contact with the membrane. A third class of proteins are peripheral membrane proteins. They adhere only temporarily to the membrane. They either bind to

integral membrane proteins or penetrate peripheral regions of the lipid bilayer. Once they have fulfilled their function, they dissociate from the membrane into the cytoplasm. They include various enzymes and hormones.

1.2 Ion channels

Pore-forming membrane proteins that enable ions to overcome the high energy barrier of the lipid bilayer of the cell membrane, are called ion channels. Their function is important for the maintenance of the resting potential, the generation of action potentials or other electrical signals and the regulation of the cell volume. This is achieved by allowing ions to flow through the water-filled pore along their electrochemical gradient (Hille, 2001). In contrast, pumps transport ions against their electrochemical gradient, across the membrane using metabolic energy in the form of ATP. This is called active transport in contrast to the passive transport of ion channels. The transport rate through the channel is up to 10^7 ions per second, which is approximately the rate at which ions diffuse in water (Hille, 2001). Even though ion channels can be seen as water-filled tunnels within the membrane, they can still discriminate between ions of different size or charge. Consequently, ion channels are divided into different groups according to their selectivity. If, for example, a channel conducts mainly potassium and can be blocked by the ion barium, which has an almost identical ionic radius, it is referred to as a potassium channel.

If an ion channel is in a closed (non-conductive) state, it is impermeable to ions and cannot conduct any electrical current. If it is in an open state, ions can pass through the open pore across the plasma membrane. As a result of the stochastic switching of the channel between closed and open, an electric current can flow through the membrane. This process of transformation from a non-conductive to a conductive conformation is called gating (Hille, 2001). The term gating has its origin in the idea that a channel pore has a so-called gate or several gates inside the protein tunnel or at the pore entrance. These must be in an open position in order to ensure free ion flux through the pore. A multitude of factors can control this process. Depending on the type of ion channels, changes in voltage or temperature, ligands such as hormones, but also mechanical forces can influence the state of the gates (Sigg, 2017). These mechanisms will be described later on in more detail.

Ion channels are an important feature for the nervous system as they play a major role in the transmission of impulses in nerve cells (Lodisch et al., 2000a). Transmitter-activated channels also mediate the conduction of stimuli via the synapses. As a result, various organisms have developed toxins that disrupt the status quo of organisms by modulating the kinetics or conductivity of ion channels. For example, the neurotoxin apamin from the venom of honeybees blocks the voltage-dependent potassium channel Kv1.3 (Voos et al., 2017).

Genetic and autoimmune dysfunctions of ion channels or proteins, which are regulating them, are called channelopathies (Ashcroft, 2005). A high number of channel dysfunctions can be attributed to mutations in genes of ion channels. These genes or certain domains are in general highly conserved and even point mutations can lead to disturbed kinetics of the channel (Rose et al., 1998). Channelopathies lead to a number of diseases such as cardiac arrhythmia and epilepsy (Levine et al., 2008; Fisher et. al., 2005).

1.3 Potassium channels

Potassium channels are the most common type of ion channels and occur in every living organism (Littleton & Ganetzky, 2000). In addition, they can be found in almost every cell type and in the membrane of many organelles. With this ubiquitous distribution they control a multitude of cell functions (Hille, 2001). Their main task is to transport potassium ions rapidly and selectively across the membrane in the direction of their electrochemical gradient. They are able to determine the resting potential in many cells. Moreover, potassium channels regulate cellular processes such as the secretion of hormones. One well studied example is the K^+ channel mediated secretion of insulin in beta cells of the pancreas. With this central role it is not surprising that dysfunctions of K^+ channels can lead to diseases such as diabetes (Tarasov et al., 2006).

There are four main groups of potassium channels. Calcium activated potassium channels such as the BK channel open due to the presence of calcium and are inhibited by an increased intracellular calcium concentration (Schiller et al., 1997). Inward rectifying potassium channels allow more ions to flow into the cell than out. The closure of ATP-dependent Kir channels, for example, is caused by a high intracellular ATP level in pancreas cells. Thus, they induce the aforementioned release of insulin (Ashcroft & Rorsman, 1989). The so-called two-pore domain potassium channels are constitutively open and are responsible for maintaining the negative membrane potential in neurons (Enyedi et al., 2010). The last group consists the voltage-dependent potassium channels to which the hERG channel belongs. The gating of these channels depends on the membrane voltage (Abbot et al., 1999).

There are over 80 mammalian genes coding for subunits of potassium channels. However, in terms of their molecular structure, bacterial potassium channels are the best studied ion channels. The amino acid sequence of the K^+ channel from *Streptomyces lividans* (KcsA K^+ channel) is similar to that of other K^+ channels including vertebrate and invertebrate voltage dependent K^+ channels, K^+ channels from plants and bacteria, and cyclic nucleotide-gated cation channels (Doyle et al., 1998). Potassium channels have a tetrameric structure and are composed of two or four identical subunits, each containing four or eight, or two or six

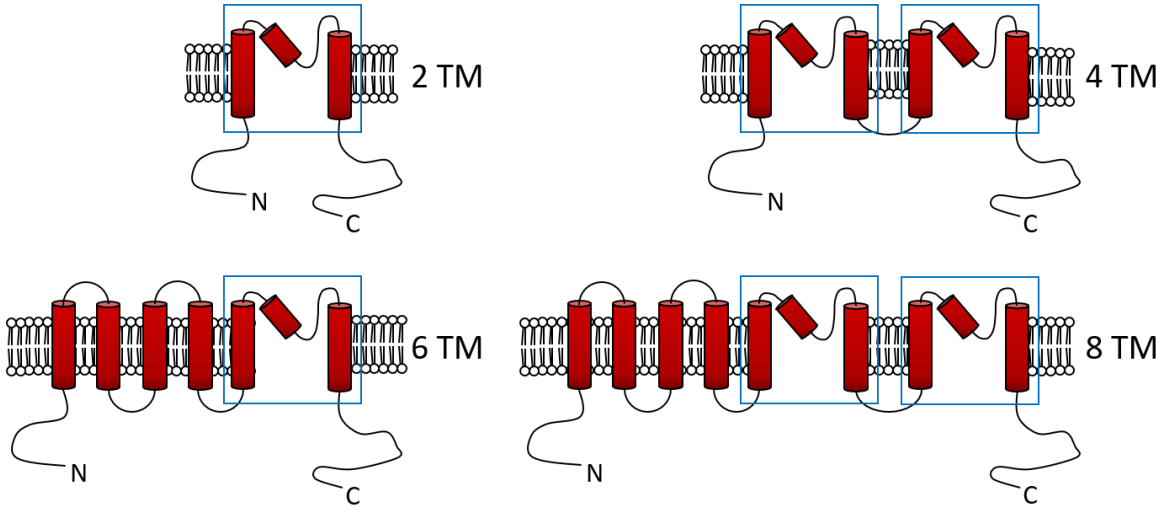

Figure 1.1: Topologies of K^+ channel subunits. Two transmembrane helices and a P-loop form the pore of potassium channels (blue square). A functional channel is built either of one tetramer with two or six transmembrane helices or a dimer of 4 or 8 transmembrane helices, respectively. N and C indicate the amino- and carboxy-terminus of the subunit. (Modified from Thiel et al., 2011)

transmembrane domains (Fig. 1.1; Thiel et al., 2011). Thus, the simplest K^+ channels consist of only two TMs per subunit. These simple K^+ channels include the K^+ inward rectifier (Kir channels; Hibino et al., 2010) or the bacterial K^+ channels KirBac and KcsA (Doyle et al., 1998; Kuo et al., 2003). Other K^+ channels have six TMs per subunit, with the pore region between the fifth and sixth TM. The voltage-dependent K^+ channels belong to this family; they possess a voltage sensor, which is composed of four TMDs of which the fourth TM contains many cationic amino acids for sensing electrical field changes (Long et al., 2005). These positive amino acids move in the electric field when the membrane voltage changes. This conformational change causes channel opening and closing (Hille, 2001; Yellen, 2002).

In addition to these major architectures of channels, there are so-called tandem channels in which two subunits form a functional channel. The unique feature of these channels is that they possess four TMs per subunit, the first and second TM and the third and fourth TM each being connected by a pore helix (Fig. 1.2). These channels are called two-pore domain (K2P) K^+ channels (Lesage & Lazdunski, 2000). Tandem K^+ channels consist of eight TMs with two pore helices. An example of such a K^+ channel is the TOK1 channel from *Saccharomyces cerevisiae* (Ahmed et al., 1999).

Common to all types of K^+ channels is, that each channel forming subunit has a characteristic pore loop which is responsible for potassium-selective permeability. The so-called selectivity filter is essentially formed by the highly conserved consensus sequence TXXXTXGY/FG (X any AS) (Heginbotham et al. 1994). Each chemical component or biomolecule dissolved in

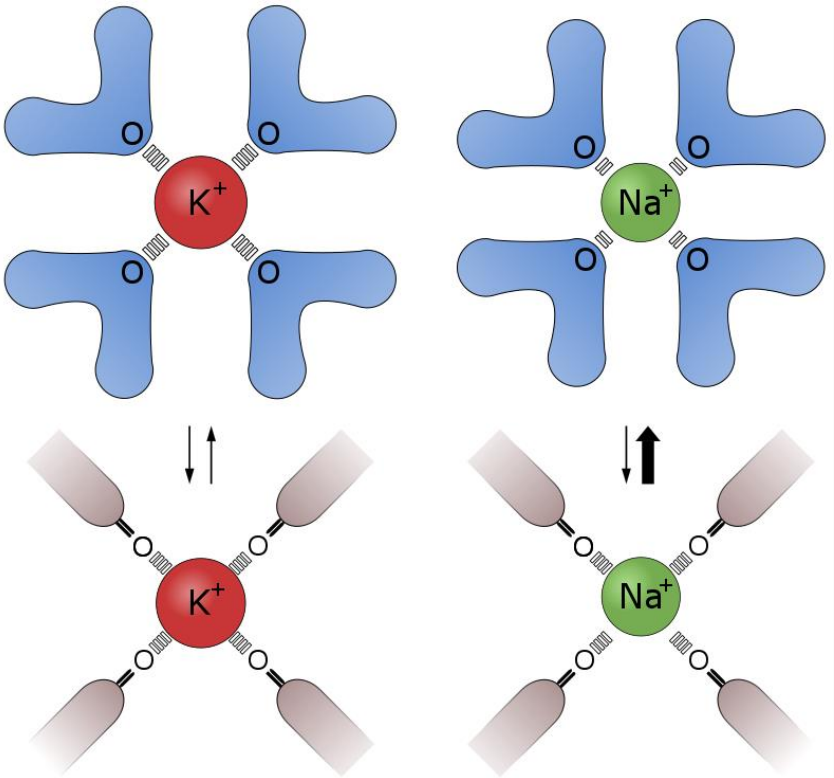

Figure 1.2: Potassium selectivity. The size of the hydration shell of potassium (K^+) and sodium (Na^+) varies due to the charge (upper row). The radius of the potassium ion hydration shell is identical to the filter of a potassium channel. Therefore, no energy is needed to switch from a hydrated state into the pore of the protein. On the other hand, because of the smaller ion radius, sodium is not fully coordinated by the carboxylic groups of the filter. Entering the pore is therefore energetically not favored. (Modified from Roux, 2017)

water has a hydrate shell at the interface of water and molecule. The electronegative oxygen atoms of the water molecules, for example, enclose a positively charged metal ion. Before potassium ions can penetrate the water-filled pore of the ion channel, the hydrate shell must be removed first (Fig. 1.2). The carbonyl oxygen of the four subunits of the selectivity filter protrude into the pore and perfectly mimic the hydrate shell of potassium ions. The distance between the carbonyl oxygens and the potassium ions is identical to the distance of the hydrate shell in aqueous solution and is therefore energetically favorable. This is why potassium transport through the channel is so efficient.

In contrast, the slightly smaller sodium ion is not able to bind to all four carbonyl oxygen residues at the same time (Fig. 1.2). Thus, the removal of the hydrate shell and the binding to the ion channel is energetically not favorable. As consequence sodium ions are less able to penetrate the selectivity filter and their transport through the pore is much slower than for potassium ions (Roux, 2017).

1.4 Gating

The functional behavior of ion channels is based on two fundamental processes: permeation and gating (Hille, 2001). Permeation is responsible for the selective and efficient translocation of ions across the membrane, whereas gating tightly controls the transfer of ions through the permeation pathway, effectively determine channel activity (Fig. 1.3). The timing of gating is crucial and is the reason why ion channels can play major roles in such diverse physiological processes. In many channels there are sensor domains, which control the gating process. Once activated, they promote transition of the channel from the open to closed state or vice versa. The transition from the non-conductive to the conductive state is due to a conformational change in the protein. The activation gate of most Kv channels for example opens in response to a membrane depolarization (Kuang et al., 2015). The voltage sensing domain controls this activation. In *Shaker* channels, four arginine residues of the S4 helix are displaced during depolarization of the membrane (Grizel et al., 2014). This movement leads to an opening of the channel.

On the cytoplasmic site of many K^+ channel proteins the inner transmembrane domains form a hydrophobic constriction, which acts as an intracellular gate. It is created by the so-called bundle-crossing mechanism, which leads to a crossover of the C-terminal ends of the inner transmembrane domains (Doyle et al., 1998; Perozo et al., 1999). In the closed state, the diameter of the intracellular gate is smaller than the diameter of hydrated potassium ions. Dehydration of the ions is not possible because there are no hydrophilic amino acids in the pore entrance. Hence, when the intracellular gate is in the closed state, potassium ions cannot pass this constriction (Williamson et al., 2003). The open state of the inner gate in a K^+ channel was observed in the calcium-gated MthK channel, a protein from *Methanobacterium thermoautotrophicum*. The crystal structure of the channel was determined in the presence of Ca^{2+} in order to bring the channel into the open state (Jiang et al., 2003). The inner helices in MthK bend under these activating conditions outwards at a glycine. As a result, the hydrophobic barrier is removed and the permeation path for K^+ is cleared.

C-type inactivation is a gating phenomenon originally observed as a conductance decrease that occurs in many voltage-gated K^+ channels after activating the channels with a depolarizing step (Hoshi & Armstrong, 2013). This gating mechanism is associated with the extracellular mouth of the channel (Baukrowitz & Yellen, 1995). The slow C-type inactivation was suggested to involve structural rearrangements in the outer pore leading to a loss of K^+ coordination sites in the selectivity filter (Consiglio et al., 2003). An important example for a C-type inactivating channel is the human ERG (hERG) or Kv1.1 channel, which is responsible for terminating the plateau phase of action potentials in cardiac ventricular cells (Keating et al., 2001). The biophysical hallmarks of C-type inactivation are reflected by high

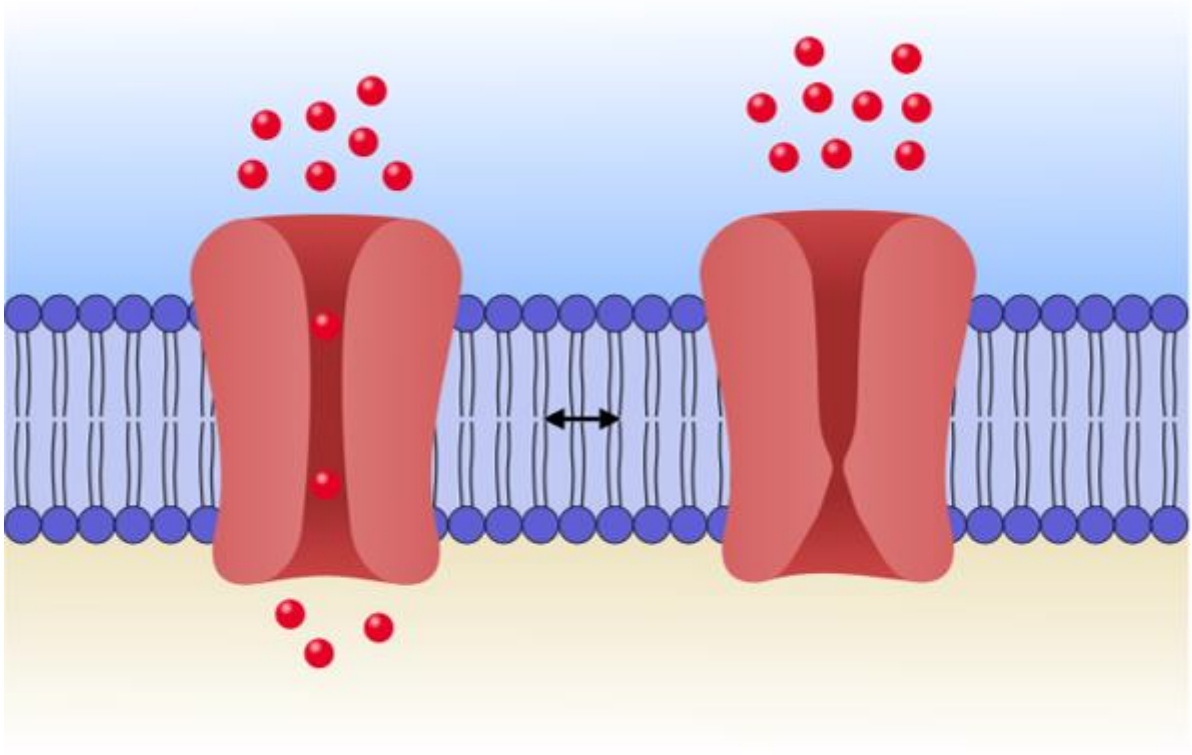

Figure 1.3: Ion channel gating. Potassium channels can dynamically switch between a non-conductive (left) and a conductive state (right). This process is called gating and is the response to external stimuli such as voltage, temperature, or pH.

external K^+ or external TEA (Choi et al., 1991). These features have been interpreted as a `foot in the door´ mechanism, in which occupancy of an ion binding site by K^+ or TEA at the external filter entrance slows or prevents the conformational changes required for C-type inactivation (Kurata & Fedida, 2006). In contrast, C-type inactivation is quite distinct from N-type inactivation, which is usually more rapid, and occurs by a ball and chain mechanism that involves the entry of the N-terminus of the channel protein into the channels inner mouth from the cytoplasmic side (Zagotta et al., 1990).

1.5 Kcv channels

Phycodna viruses form a family of large double-stranded DNA viruses with a genome of 160 to 560 kb, which infect marine and freshwater algae (Wilson et al., 2009). They code for many proteins that also exist in prokaryotes and eukaryotes (van Etten & Dunigan, 2013; Thiel et al., 2011). Among these viral gene products there are small proteins that form functional potassium channels (Plugge et al., 2000). The most studied viral potassium channel is from

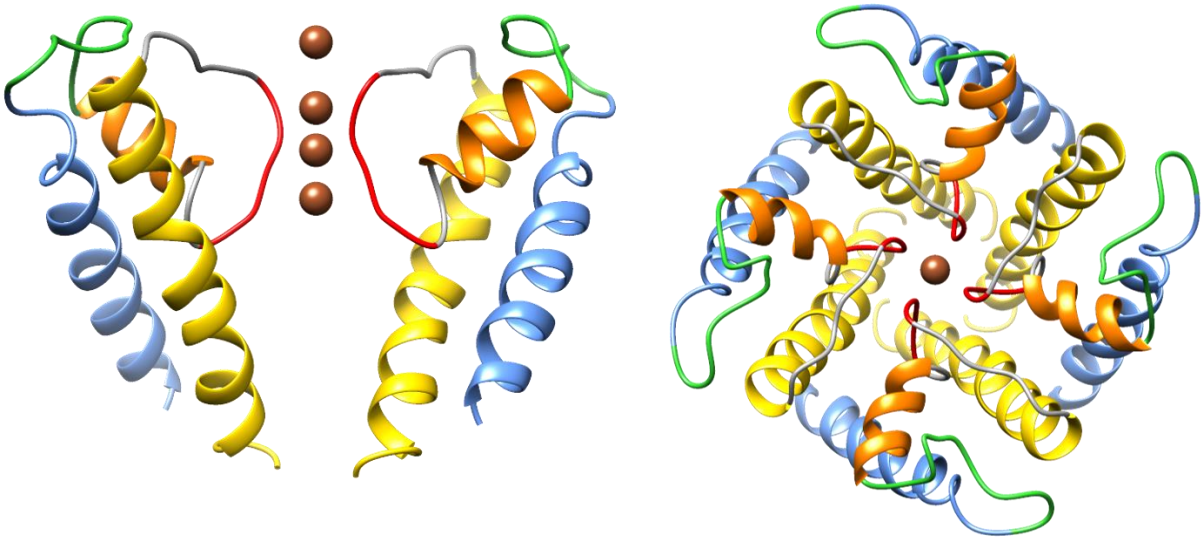

Figure 1.4: Homology model of the viral potassium channel Kcv_{NTS}. Shown are two opposing subunits of Kcv_{NTS} (left). Each subunit consists of: inner transmembrane domain (yellow), short loop (green), pore helix (orange), selectivity filter (red) and outer transmembrane domain (blue). The spheres (brown) represent potassium ions. Top view of all four subunits of Kcv_{NTS} (right). The homology model was generated with Swissmodel[1] (Biasini et al., 2004) and is based on the structure of KirBac1.1 [PDB: 1P7B] (Rauh et al., 2017). The image was made with Chimera[2].

Paramecium bursaria chlorella virus-1 (PBCV-1). It consists of four monomers, which form a central water filled pore. This architecture is identical to the pore module of all complex K^+ channels from pro- and eukaryotes. Because each subunit of the viral channel has only 94 amino acids it belongs to the smallest known potassium channels.

PBCV-1 probably requires the potassium channel to infect the alga host. During the early infection phase, the virus membrane containing the channel fuses with the plasma membrane of the host which with the effect that the latter depolarizes (Greiner et al., 2009). This is achieved by the increase in K^+ conductance in the host membrane. A subsequent efflux of K^+ from the host results in a decrease of internal turgor pressure in the algae, which makes it easier for the virus to eject its DNA into the algae (Thiel et al., 2010).

A subfamily of viral potassium channel, very similar to that of Kcv from PBCV1, is the ATCV-1 like family. The archetype of this group is encoded by the chlorella virus ATCV-1 (*Acanthocystis turfacea Chlorella virus-1;* Fitzgerald et al., 2007). These channels consist of only 82 amino acids per subunit; they lack any cytosolic or extracellular loop. With this architecture they are fully embedded in the lipid membrane (Braun et al., 2014). The full genomic sequencing of many ATCV type viruses has over the last decade provided a large library of

[1] http://swissmodel.expasy.org/

[2] https://www.cgl.ucsf.edu/chimera/

homologous sequences (Siotto et al., 2017). The interesting finding from an electrophysiological characterization of some of these channels is that they exhibit distinct functional differences in spite of their similarity in the primary amino acid sequence (Rauh et al., 2017). Due to their easy handling (Winterstein et al., 2018) and the fact that the structure is representative for the architecture of the pore module of complex K^+ channels (Kang et al., 2004), ATCV-1 like channels are an ideal model system to investigate basic channel properties.

1.6 Optogenetics

It has been mentioned in the previous chapters that ion channels can translate signals into an opening and closing of their conducting pore (Latorre et al., 2010). Thus, the channel is able to change the membrane potential in responds to different stimuli. One attractive stimulus is light, because it operates with a high spatial and temporal resolution (Häusser, 2014). In particular, the discovery of the light gated channels and pumps has paved the way to allow remote manipulation of many cellular processes, like neuronal firing and hormone release by light. These seminal experiments have inspired the rapid growth of a new experimental technology, termed optogenetics, in which cellular events are controlled by light is summarized (Deisseroth et al., 2006).

The discovery of bacteriorhodopsin by Oesterhelt & Stoeckenius (1971) was the first step towards optogenetics. This rhodopsin-like protein can pump protons under illumination. Further discoveries of additional members of the opsin family such as the Halorhodopsin (Shugiyama & Mukohata, 1984) and the Channelrhodopsin (Nagel et al., 2002) followed and extended the spectrum of light sensitive membrane transporters. In particular, the discovery of Channelrhodopsin from *Chlamydomonas reinhardtii* was a major breakthrough (Nagel et al., 2002; Boyden et al., 2005). By expressing this light sensitive protein in cells, it was now possible to activate firing of neurons by light; expression of the aforementioned light sensitive pumps had the opposite effect in that they hyperpolarized cells and silenced them (Guru et al., 2015).

Opsins belong to a family of retinal-binding proteins. They are light-sensitive, consist of seven transmembrane domains and are encoded by opsin genes. They exist ubiquitously in all organisms, including eukaryotes and bacteria where they function as light-responsive ion pumps and sensory receptors. The opsin genes are divided into two families. One branch contains microbial opsins (type I). They are found in prokaryotes, algae and fungi. Their characteristic feature is the binding of retinal exclusively in the *trans* configuration. They capture light energy and use it to either actively pumping ions across the cell membrane, or they open channels for passive cation transport across the cell membrane.

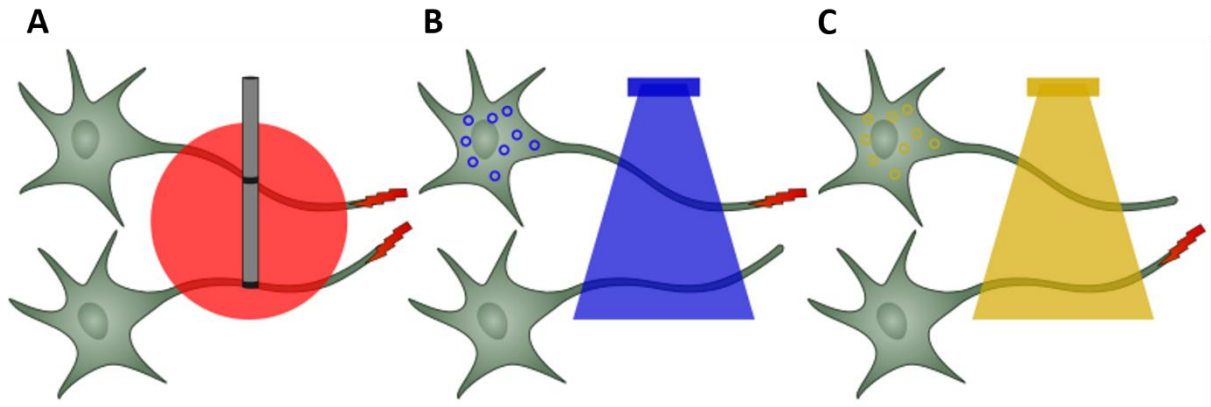

Figure 1.5: Principle of Optogenetics (A) Electric stimulation with an electrode leads to an activation (red lightning) of every ion in the stimulated area. (B) Only the upper neuron, which gained a function can be stimulated with the blue light source. Neuronal activity can be controlled with light using channelrhodopsin. (C) Optogenetic inhibition due to the loss of function of the upper neuron. Anion channelrhodopsins can be used to specifically and rapidly inhibit neural systems involved in *Drosophila* locomotion or wing expansion. (Modified from Deisseroth, 2006)

In contrast, animal opsins (type II) bind retinal in the 1,1-*cis* configuration. This type only occurs in higher eukaryotes and is mainly responsible for vision. They are also known as G-protein coupled receptors (GPCRs). Their sensitivity towards light is several times higher than that of microbial opsins. The reason lies in the amplification of the light signal by the G-protein coupled cascades.

Today, optogenetics is a technology that allows optical modulation of individual cells within complex tissues. This is possible by introducing natural or engineered proteins containing photoreceptive domains coupled to biological functions. For example, target proteins can be inhibited by a laser, which is referred to as "loss of function" (Schmucker et al., 1994). Conversely, a laser can also directly stimulate neurons to control genetically modified cells ("gain of function", Fork, 1971).

However, classical optogenetic proteins also have deficits, such as poor expression in mammalian cells or low light-sensitivity. Nevertheless, a toolbox with improved protein properties has been created in recent years (Liu & Tucker, 2017).

Concerning ion channels, some modified or even synthetically generated light-gated K^+ channels have already been developed. In 2004 Banghart et al. were able to control the activity of the potassium channel *Shaker* H4 by the coupling with a cofactor. Another example is the light activation of the inwardly rectifying potassium channel Kir2.1 by the incorporation of a photoreactive UAA into the pore (Kang et al., 2013). A third example for an engineering of light gated channels is related to the abovementioned viral potassium channel Kcv_{PBCV-1}. This channel was fused to the LOV2-Jα photosensory region of a plant blue-light receptor to create a single-component light-gated K^+ channel (Cosentino et al., 2015).

1.7 Quaternary ammonium cations

The light-gated ion channel developed by Banghart et al. (2004) described above functions by coupling an azo compound to the channel, which is able to block the channel in a light dependent manner. For this approach, a special feature of K^+ channels was employed (Blaustein et al., 2000) namely their sensitivity to external Tetraethylammonium (TEA) (MacKinnon & Yellen, 1990). The light sensitivity of the designed channel builds on a molecule with a TEA head group. This blocker inhibits or opens the channel pore in a light-dependent manner.

In addition to such engineering approaches, symmetrical tetraalkylammonium cations (TAA) can be used to obtain information about the structure of channel proteins. They belong to the chemical class of quaternary ammonium compounds (QAs). They are defined by a fourfold bound nitrogen atom, which is coupled as amine or imine to 4 organic residues. Thus, the central nitrogen is positively charged and the organic compounds can vary in length and configuration (Fig. 1.6). In addition to use QAs as K^+ channel blockers in channel research, these compounds are also used as phase-transfer catalysts or ionic liquids (Asai et al., 1993; Bhowmik et al., 2014). Since the middle of the last century, smaller QAs in particular have been investigated for their hydration structure (Bhowmik, 2011; Nightingale, 1959). Their names derive from the length of their alkyl chains: Tetramethylammonium (TMA) < Tetraethylammonium (TEA) < Tetrapropylammonium (TPrA), etc.

Table 6.1 shows the commonly used diameter values, which were obtained by Robinson & Stokes (1959) and which are also used in this work. Marcus (2008) summarized the Stokes diameter of the different QAs. These were calculated by infinite ionic conductivities.

One of the features of these compounds it that their solubility increases with increasing chain length. For example, the solubility of TPeA is so low that larger QAs are assumed of being almost insoluble in water (Dubini-Paglia et al., 1970). Nevertheless, there are exact values for the solubility of QA salts (Nakayama, 1981 and 1989). Table 6.2 shows that the solubility of QA chlorides does not gradually decrease at constant temperature. In addition, the corresponding anion also plays a role in solubility. Accordingly, the solubility of QA salts increases with smaller halide anions $F^- > Cl^- > B^- > I^-$ (Nakayama, 1989). Concerning QA chlorides, the solubility increases up to TPeA and then decreases strongly.

Basic research on the block of K^+ channels by QA ions was done by Clay Armstrong. In his work he demonstrated the basic features of the block. He could show that the extension of the action potential in squid axons after the injection of TEA is due to the blocking of K^+ channels (Armstrong & Binstock, 1965). He argued that QA ions can penetrate the open pore. He also observed that TEA can block K^+ channels not only from the cytosolic side but also from the extracellular side. Since the block effects vary, Armstrong and coworker assumed an asymmetric architecture of the two pore entrances (Armstrong et al., 1971).

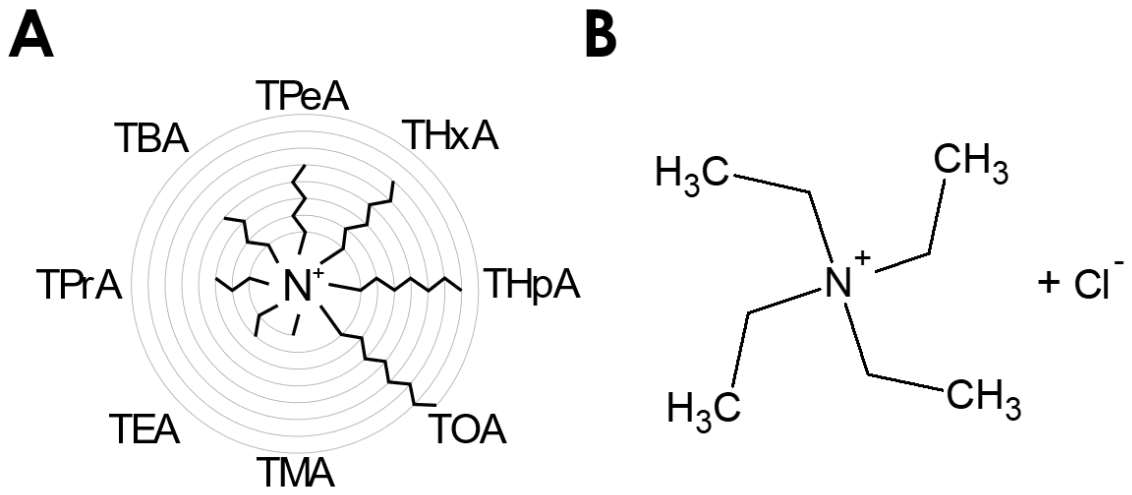

Figure 1.6: Nomenclature and chain length of different QAs. Four organic residues are bound to a positively charged nitrogen atom. (A) Tetramethylammonium (TMA) is the smallest QA with a chain length of only one methyl group. The largest QA shown here is Tetraoctylammonium (TOA). (B) Sketch of Tetraethylammonium (TEA) with all four residues.

Subsequent work has shown that almost all K^+ channels can be inhibited by QA ions (Hille, 2001; Lenaeus et al., 2005). The reason for the ubiquitous effect of QA ions on K^+ channels is explained by their physical similarity to hydrated alkali metals. With their similarity to K^+ they can presumably bind inside the cavity near the selectivity filter. The model K^+ channel KcsA has been crystallized in the presence of TEA and TBA (Lenaeus et al., 2014). In the crystal structures it was found that the QA binding site lies within the dehydration transition site of the K^+ ions. At this position the ions strip off their hydrate shell and enter the selectivity filter. However, TEA and larger QAs are unable to enter the selectivity filter and instead occlude its entrance (Lenaeus et al., 2005).

1.8 Aim of work

The following work will provide information on the cytosolic pore structure of the two viral potassium channels Kcv_{NTS} and Kcv_S. A further aim is to generate a light-dependent K^+ channel based on Kcv_{NTS}. Furthermore, the epoxide ADEX was investigated regarding its functionality as a septum for lipid bilayer.

The first part of the work is inspired by the fact that the two viral K^+ channels possess a nearly identical primary structure but differ in their electrophysiological properties. This functional

difference is due to an intracellular gate in Kcv_S but not in Kcv_{NTS} (Rauh et al., 2017). To better understand the mechanisms of this gate the intracellular pore structure was investigated using quaternary ammonium cations. Since they have defined diameters, it is possible to draw conclusions about the diameter of the pore (French & Shoukimas, 1981). The data show, that the intracellular gate has no influence on the diameter of the pore entrance, but the structure of the QA binding site is altered.

In the second part of the work a light-dependent K^+ channel was engineered. The small size and the profound knowledge of structure and function relations makes viral K^+ channels, excellent building elements for engineering of channels with new sensor properties (Cosentino et al., 2015). Inspired by the work of Banghart et al. (2004) the synthetic molecule MAL-AZO-QA was coupled to Kcv_{NTS}. The goal was to use this light-sensitive tether molecule to block and unblock the channel in a light dependent manner. In the process of this endeavor the sensitivity of the channel against TEA had to be improved by mutations. Furthermore, the conductivity of the channel could also be increased by another mutation. The available database on a large number of Kcv variants with different functional properties were a great advantage in these experiments.

The last part presents strategies for optimizing the free-standing vertical lipid-bilayer method. The commonly used Teflon foil as septum was replaced by a thin-film epoxy resist ADEX. Defined apertures with diameters between 30 µm and 100 µm were micro-fabricated by photolithography. While ADEX offers no advantages in terms of capacitance and signal-to- noise ratio, it enables long-term experimental recordings while the stability of the lipid bilayer is not compromised by pipetting solutions in and out of the recording chamber. Another advantage is that ADEX foiled can be cleaned with acetone for further applications.

1.9 References

Abbott G. W., F. Sesti, I. Splawski, M. E. Buck, M. H. Lehmann, K. W. Timothy, M. T. Keating, and S. A. Goldstein (1999) MiRP1 forms IKr potassium channels with HERG and is associated with cardiac arrhythmia. *Cell 97: 175–187*

Ahmed, A., F. Sesti, N. Ilan, T.M. Shih, S.L. Sturley, and S.A. Goldstein (1999) A molecular target for viral killer toxin: TOK1 Potassium Channels. *Cell 99(3): 283-291*

Alberts B, A. Johnson, and J. Lewis *(2002) Molecular Biology of the Cell (4th ed.). New York: Garland Science. ISBN 978-0-8153-3218-3.*

Armstrong C. M. (1971) Interaction of tetraethylammonium ion derivatives with the potassium channels of giant axons. *J. Gen. Physiol.*, *58*(4), 413–437.

Armstrong C. M., and L. Binstock (1965) Anomalous Rectification in the Squid Giant Axon Injected with Tetraethylammonium Chloride. *J. Gen. Physiol.*, *48*(5), 859–872.

Asai S., H. Nakamura, M. Tanabe, and K. Sakamoto (1993) Distribution and dissociation equilibria of phase-transfer catalysts, tetrabutylammonium salts. *Ind. Eng. Chem. Res.*, *32*(7), 1438–1441.

Ashcroft F. M., and P. Rorsman (1989) Electrophysiology of the pancreatic beta-cell. *Prog Biophys Mol Biol 54:87–143*

Ashcroft F. M. (2005) Review series ATP-sensitive potassium channelopathies : focus on insulin secretion., *115*(8), 2047–2058.

Bakker E., and P. Bu (1997) Carrier-Based Ion-Selective Electrodes and Bulk Optodes . 1 . General Characteristics., *2665*(94).

Banghart M., K. Borges, E. Isacoff, D. Trauner, and R. H. Kramer (2004) Light-activated ion channels for remote control of neuronal firing. *Nat Neurosci.*, *7*(12), 1381–1386.

Baukrowitz T., and G. Yellen (1995) Modulation of K + Current by Frequency and External [K+]: A Tale of Two Inactivation Mechanisms. *Neuron*, *15*, 951–960.

Bhowmik D., N. Malikova, G. Me, O. Bernard, and P. Turq (2014) Aqueous solutions of tetraalkylammonium halides : ion hydration , dynamics and ion – ion interactions. *R. Soc. Chem.*, *16*(13477), 10–15.

Biasini M., S. Bienert, A. Waterhouse, K. Arnold, G. Studer, T. Schmidt, F. Kiefer, T. G. Cassarino, M. Bertoni, L. Bordoli, and T. Schwede (2014) SWISS-MODEL : modelling protein tertiary and quaternary structure using evolutionary information. *Nucleic Acids Res.*, *42*(April), 252–258.

Blaustein R. O., P. A. Cole, C. Williams, and C. Miller (2000) Tethered blockers as molecular "tape measures" for a voltage-gated K+channel. *Nat. Struct. Biol.*, *7*(4), 309–311.

Bhowmik, D. (2011) Study of microscopic dynamics of complex fluids containing charged hydrophobic species by neutron scattering coupled with molecular dynamics simulations, *Paris.*

Bondi A. (1964) van der Waals Volumes and Radii. *J. Phys. Chem.*, *68*(3), 441–451.

Boyden E. S., F. Zhang, E. Bamberg, G. Nagel, and K. Deisseroth (2005) Millisecond-timescale , genetically targeted optical control of neural activity. *Nat. Neurosci.*, *8*(9), 1263–1268.

Braun C. J., C. Lachnit, P. Becker, L. M. Henkes, C. Arrigoni, S. M. Kast, A. Moroni, G. Thiel, and I. Schroeder (2014) Biochimica et Biophysica Acta Viral potassium channels as a robust model system for studies of membrane – protein interaction ☆ , ☆☆. *BBA - Biomembr.*, *1838*(4), 1096–1103.

Choi K. L., R. W. Aldricht, and G. Yellen (1991) Tetraethylammonium blockade distinguishes two inactivation mechanisms in voltage-activated Ki channels. *Proc. Natl. Acad. Sci U.S.A.*, *88*(June), 5092–5095.

Comte J., M. Bernard, and D. C. Gautheron (1976) Lipid Composition and Protein Profiles of Outer and Inner Membranes from Pig Heart Mitochondria. *Biochim. Biophys. Acta*, *419*, 271–284.

Consiglio J. F., P. Andalib, and S. J. Korn (2003) Influence of Pore Residues on Permeation Properties in the Kv2 . 1 Potassium Channel . Evidence for a Selective Functional Interaction of K^+ with the Outer Vestibule., *121*(February).

Cosentino C., L. Alberio, S. Gazzarrini, M. Aquila, E. Romano, S. Cermenati, P. Zuccolini, J. Petersen, M. Beltrame, J. L. Van Etten, J. M. Christie, G. Thiel, and A. Moroni (2014) Engineering ofa light-gated potassium channel. *Science (80-.)*., *9844*(2011).

Deisseroth K., G. Feng, A. K. Majewska, G. Miesenböck, A. Ting, and M. J. Schnitzer (2006) Next-Generation Optical Technologies for Illuminating GeneticallyTargeted Brain Circuits. *J. Neurosci. Methods*, *26*(41).

Doyle D. A., J. Morais Cabral, R. A. Pfuetzner, A. Kuo, J. M. Gulbis, S. L. Cohen, B. T. Chait, and R. MacKinnon (1998) The structure of the potassium channel: molecular basis of K+ conduction and selectivity. *Science*, *280*(5360), 69–77.

Dubini-Paglia E., and T. Mussini (1971) Behaviour of Solutions of Tetraalkylammonium Salts in Ethyl Bromide as Liquid Membranes. *Zeitschrift Für Naturforsch.*, *26*(1), 154–158.

Enyedi P., and G.Czirjak (2010) Molecular background of leak K+ currents: two-pore domain potassium channels. *Physiol Rev 90(2):559– 605. doi:10.1152/physrev.00029.2009*

Fisher R. S., W. Van Emde Boas, W. Blume, C. Elger, P. Genton, P. Lee, and J. Engel (2005) Epileptic seizures and epilepsy: Definitions proposed by the International League Against Epilepsy (ILAE) and the International Bureau for Epilepsy (IBE). *Epilepsia*, *46*(4), 470–472.

Fitzgerald L. A., M. V Graves, X. Li, J. Hartigan, A. J. P. Pfitzner, E. Hoffart, and J. L. van Etten (2007) NIH Public Access. *Virology*, *362*(2), 350–361.

French, R.J., and J.J. Shoukimas (1981) Blockage of squid axon potassium conductance by internal tetra-N-alkylammonium ions of various sizes. *Biophysical Journal 34 (2), 271–291.*

Grizel A. V, G. S. Glukhov, and O. S. Sokolova (2014) Mechanisms of Activation of Voltage-Gated Potassium Channels. *Acta Nat.*, *6*(23), 10–26.

Guru A., R. J. Post, Y. Ho, and M. R. Warden (2015) Making Sense of Optogenetics. *Int. J. Neuropsychophamacology*, 1–8.

Häusser M. (2014) Optogenetics : the age of light. *Nat. Publ. Gr.*, *11*(10), 1012–1014.

Heginbotham L., Z. Lu, T. Abramson, and R. MacKinnon (1994) Mutations in the K+ channel signature sequence. *Biophys. J.*, *66*(4), 1061–1067.

Hibino, H., A. Inaobe, S. Murakami, I.Findlay, and Y. Kurachi (2010) Inwardly rectifying potassium channels: their structure, function, and physiological roles. *Physiol. Rev. 90(1): 291-366*

Hille (2001) Ion channels of excitable membranes. *Sinauer Associates, Inc*.

Hoshi T., and C. M. Armstrong (2013) C-type inactivation of voltage-gated K + channels: Pore constriction or dilation? *J. Gen. Physiol.*, *141*(2), 151–160.

Jiang, Y., A. Lee, J. Chen, V. Ruta, M. Cadene, B.T. Chait, and R. MacKinnon (2003) X-ray structure of a voltage-dependent K+ channel. *Nature 423(6935): 33-41*

Kang J., D. Kawaguchi, I. Coin, Z. Xlang, D. D. M. O'Leary, A. P. Slesinger, and L. Wang (2013) In vivo Expression of a Light-activatable Potassium Channel Using Unnatural Amino Acids. *Neuron*, *16*(80).

Kang M., A. Moroni, S. Gazzarrini, D. DiFrancesco, G. Thiel, M. Severino, and J. L. Van Etten (2004) Small potassium ion channel proteins encoded by chlorella viruses. *Proc. Natl. Acad. Sci. U. S. A.*, *101*(15), 5318–5324.

Keating M. T., M. C. Sanguinetti, and H. Hughes (2001) Molecular and Cellular Mechanisms of Cardiac Arrhythmias. *Cell*, *104*, 569–580.

King E. J. (1969) Absolute Partial Molar Ionic Volumes by. *J. Phys. Chem.*, *2219*(1962), 4590–4592.

Kuang Q., P. Purhonen, and H. Herbert (2015) Structure of potassium channels. *Cell. Mol. Life Sci.*, *72*(19), 3677–3693.

Kurata H. T., and D. Fedida (2006) A structural interpretation of voltage-gated potassium channel inactivation. *Biophys. Mol. Biol.*, *92*, 185–208.

Lagowski, J.J., (1976) The chemistry of nonaqueous solvents V4: Solution Phenomena and Aprotic Solvents. *Academic Press, New York, 1 online resource*

Latorre R., F. J. Morera, and C. Zaelzer (2010) Allosteric interactions and the modular nature of the voltage- and Ca 2 + -activated (BK) channel. *J Physiol*, *17*, 3141–3148.

Lenaeus M. J., M. Vamvouka, P. J. Focia, and A. Gross (2005) Structural basis of TEA blockade in a model potassium channel. *Nat. Struct. Mol. Biol.*, *12*(5), 454–459.

Lenaeus, M.J., D. Burdette, T. Wagner, P.J. Focia, and A. Gross (2014) Structures of KcsA in complex with symmetrical quaternary ammonium compounds reveal a hydrophobic binding site. *Biochemistry 53 (32), 5365–5373. 10.1021/bi500525s.*

Lesage, F., and M. Lazdunski (2000) Molecular and functional properties of two-pore-domain potassium channels. *Am. J. Physiol. Renal Physiol. 279(5): F793-801*

Levine E., S. Z. Rosero, A. S. Budzikowski, A. J. Moss, W. Zareba, and J. P. Daubert (2008) Congenital long QT syndrome: considerations for primary care physicians. *Cleve.Clin J Med.*, *75*(8), 591–600.

Littleton J. T., and B. Ganetzky (2000) Ion Channels and Synaptic Organization. *Neuron*, *26*(1), 35–43.

Liu Q., and C. L. Tucker (2017) Engineering genetically-encoded tools for optogenetic control of protein activity. *Curr Opin Chem Biol 2017, 40:17-23.*

Lodish H., A. Berk, and L. S. Zipursky *(2000a) Biomembranes: Structural Organization and Basic Functions. Molecular Cell Biology (4th ed.). New York: Scientific American Books. ISBN 978-0-7167-3136-8.*

Lodish H., A. Berk, S. L. Zipursky, P. Matsudaira, D. Baltimore, and J. Darnell *(2000b) Biomembranes: Structural Organization and Basic Functions. Molecular Cell Biology (4th ed.).*

Long, S. B., E. B. Campbell, and R. MacKinnon (2005) Crystal structure of a mammalian voltage-dependent Shaker family K^+ channel. *Science 309(5736): 897-903*

MacKinnon R., and G. Yellen (1990) Mutations Affecting TEA Blockade and Ion Permeation in Voltage-Activated K + Channels m). *Sciene*, *250*(4978), 276–279.

Marcus Y. (2008) Tetraalkylammonium Ions in Aqueous and Non-aqueous Solutions. *J. Solut. Chem.*, *37*, 1071–1098.

Nagel G., D. Ollig, M. Fuhrmann, S. Kateriya, A. M. Musti, E. Bamberg, and P. Hegemann (2002) Channelrhodopsin-1 : A Light-Gated Proton Channel in Green Algae. *Science (80-.).*, *296*(June), 2395–2399.

Nakayama, H. (1981) Solid-liquid and liquid-liquid phase equilibria in the symmetrical tetraalkylammonium halide-water systems. *BULL CHEM SOC JPN*. 54. 3717-3722. 10.1246/bcsj.54.3717.

Nakayama H., H. Kuwata, N. Yamamoto, Y. Akagi, and H. Matsui (1989) Solubilities and dissolution states of a series of symmetrical tetraalkylammonium salts in Water. *BULL CHEM SOC JPN*. 62. 985-992. 10.1246/bcsj.62.985.

Nighingale E. R. (1959) Phenomenological Theory of Ion Solvation. Effective Radii of Hydrated Ions. *J. Phys. Chem.*, *63*(9), 1381–1387.

Noutsi P., E. Gratton, and S. Chaieb (2016) Assessment of membrane fluidity fluctuations during cellular evelopment reveals time and cell type specificity. *PLoS One 11, e0158313.*

Oesterhelt D., and W. Stoeckenius (1971) Rhodopsin-like Protein from the Purple Membrane of Halobacterium halobium. *Nat. New Biol.*, *233*(149), 52.

Perozo E., D. M. Cortes, and L. G. Cuello (1999) Structural rearrangements underlying K+-channel activation gating. *Science*, *285*(5424), 73–78.

Rauh O., M. Urban, L. M. Henkes, T. Winterstein, T. Greiner, J. L. Van Etten, A. Moroni, S. M. Kast, G. Thiel, and I. Schroeder (2017) Identification of Intrahelical Bifurcated H-Bonds as a New Type of Gate in K+Channels. *J. Am. Chem. Soc.*, *139*(22), 7494–7503.

Ray T. P., V. P. Skipski, M. Bacclay, E. Essner, and F. M. Archibald (1969) Lipid Composition of Rat Liver Plasma Membranes *. *J. Biol. Chem.*, *224*(20), 5528–5536.

Robinson, R.A., and R. H. Stokes (1959) Electrolyte solutions, *2nd ed. Butterworth, London*

Rose M. R. (1998) Neurological channelopathies. *British MedicalJournal, vol. 316, no. 7138, pp. 1104–1105, 1998.*

Roux, B. (2017) Ion channels and ion selectivity. *Essays Biochem. 61(2): 201-209*

Rowe J. M., D. D. Dunigan, G. Blanc, J. R. Gurnon, Y. Xia, and J. L. Van Etten (2013) Evaluation of higher plant virus resistance genes in the green alga , Chlorella variabilis NC64A , during the early phase of infection with Paramecium bursaria chlorella virus-1. *Virology*, *442*(2), 101–113.

Schiller, J., Y. Schiller, G. Stuart, and B. Sakmann (1997). Calcium action potentials restricted to distal apical dendrites of rat neocortical pyramidal neurons. *J. Physiol. 505, 605–616. doi: 10.1111/j.1469-7793.1997.605ba.x*

Sigg D. (2017) Modeling ion channels: past, present, and future. *J Gen Physiol. 1442014; :7–26.*

Singleton P. *(1999) Bacteria in Biology. Biotechnology and Medicine (5th ed.). New York: Wiley. ISBN 978-0-471-98880-9.*

Siotto F., C. Martin, O. Rauh, J. L. Van Etten, I. Schroeder, A. Moroni, and G. Thiel (2014) Viruses infecting marine picoplancton encode functional potassium ion channels. *Virology*, *466–467*, 103–111.

Sugiyama Y., and Y. Mukohata (1984) Isolation and Characterization of Halorhodopsin from Halobacterium Chromoprotein. *J. Biol. Chem.*, *96*(2), 413–420.

Tarasov A. I., C. A. J. Girard, and F. M. Ashcroft (2006) Intact and Permeabilized Pancreatic - Cells. *Diabetes*, *55*(September).

Thiel G., D. Baumeister, I. Schroeder, S. M. Kast, J. L. Van Etten, and A. Moroni (2011) Minimal art: Or why small viral K+ channels are good tools for understanding basic structure and function relations. *Biochim. Biophys. Acta - Biomembr.*

Voos P., M. Yazar, R. Lautenschläger, O. Rauh, A. Moroni, and G. Thiel (2017) The small neurotoxin apamin blocks not only small conductance Ca2+activated K+channels (SK type) but also the voltage dependent Kv1.3 channel. *Eur. Biophys. J.*, *46*(6), 517–523.

Williamson I. M., S. J. Alvis, J. M. East, and . G. Lee (2003) The potassium channel KcsA and its interaction with the lipid bilayer. *Cell. Mol. Life Sci.*, *60*(8), 1581–1590.

Wilson W. H., J. L. Van Etten, and M. J. Allen (2009) The Phycodnaviridae: The story of how tiny giants rule the world. *Curr. Top. Microbiol. Immunol.*, *328*, 1–42.

Winterstein L. M., K. Kukovetz, O. Rauh, D. L. Turman, C. Braun, A. Moroni, and I. Schroeder (2018) Reconstitution and functional characterization of ion channels from nanodiscs in lipid bilayers. *J. Gen. Physiol.*, *150*(4), 637–646.

Wu C., and D. Sun (2015) GABA receptors in brain development , function , and injury. *Metab Brain Dis*, *30*, 367–379.

Zagotta W. N., T. Hoshi, and R. W. Aldrich (1990) Restoration of Inactivation in Mutants of Shaker Potassium Channels by a Peptide Derived from ShB. *Science (80-.)*., *250*(4980), 568–571.

2 Properties of the inner pore region of Kcv_{NTS} and Kcv_S revealed by block with quaternary ammonium ions

2.1 Abstract

Quaternary ammonium cations (QAs) are ideal molecules to draw conclusions about the pore structure of ion channels. They can also be used to study transport mechanisms. The two viral potassium channels Kcv_{NTS} and Kcv_S differ in their electrophysiological properties despite their almost identical amino acid sequence. The reason for this is an additional (inner) gate in Kcv_S. The intracellular block of QAs of different sizes is on the one hand voltage-dependent. On the other hand, the sensitivity increases and the speed of the block decreases with increasing molecule diameter. Especially for the small blockers TEA and TPrA the two channels show differences in sensitivity, which is due to a changed blocker dissociation and association rate. The elimination of the inner gate in Kcv_S leads to a drastic increase in blocker dissociation, as the bulky aromatic side chain of the gate might leads to a trapping of the QAs within the cavity. If only the kink of the gate is mutated, the channel Kcv_S S77G has identical block properties as Kcv_{NTS}. The pore diameter of the two viral potassium channels could not be defined, as the there was no marked difference in the association rates for blockers of different size.

2.2 Introduction

Viral potassium channels of the ATCV subfamily consist of only 82 amino acids per subunit, and are thus among the smallest known potassium channels. They represent only the pore module of complex potassium channels and have no cytosolic or intracellular domains (Braun et al., 2014a). Like other K^+ channels, they form tetramers. Despite their small size, they have similar functional properties to large K^+ channels. This includes for example, potassium selectivity or sensitivity against block by barium ions (Thiel et al., 2011). Although, they have a high AA identity, the two channels of this subfamily investigated here have different electrophysiological properties (Rauh et al., 2017). The most prominent difference is caused by a gate at the inner transmembrane domain, which is present in Kcv_S and absent in Kcv_{NTS}. Serine at position 77 in Kcv_S forms an intrahelical hydrogen bond with the carboxyl oxygen of Ile^{73}. Due to the swing of the resulting kink, the aromatic rings of Phe^{78} move into the cavity and then block the ion flux (Fig. 2.1). Ser^{77} is absent in Kcv_{NTS}, where it is replaced by a glycine, resulting in a permanently open cytosolic gate. On the background of this gate it is of interest to analyze the structural differences between the two channels further.

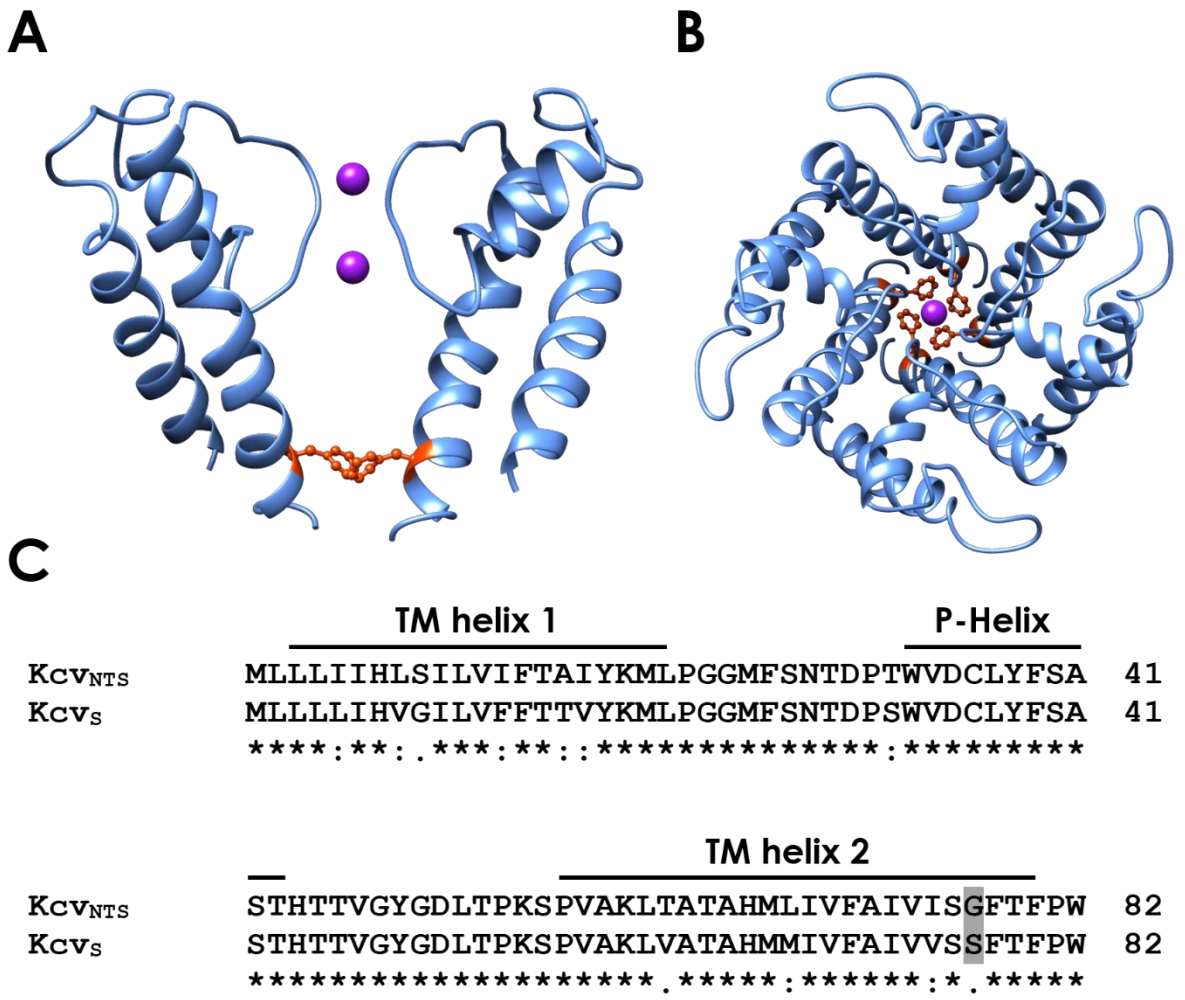

Figure 2.1: **Comparison of the two viral potassium channels Kcv_{NTS} and Kcv_S.** (A) Side view of a homology model of Kcv_{NTS} (only two opposing monomers are displayed). (B) Top view from extracellular side of the full tetrameric channel. Residue Phe^{78} is highlighted in orange, potassium ions are shown as purple spheres (C) Sequence alignment of the two viral encoded K^+ channels. Identical amino acids are labeled with stars. Conservative and semi-conservative amino acid differences are labeled with colons or dots, respectively. The crucial position 77 is highlighted in grey. The homology model was generated with Swissmodel (Biasini et al., 2004) and is based on the structure of KirBac1.1 [PDB: 1P7B] (Rauh et al., 2017).

Membrane proteins are difficult to crystallize due to their partially hydrophobic surface, flexibility and lack of stability (Carpenter et al., 2008). Attempts have been made to crystallize Kcv channels. However, either crystallization could not be achieved or the diffraction of the crystals was too weak (personal communication of Gerhard Thiel). Another method to elucidate protein structures has been established in recent years known as cryo-EM. This method is based on the principle of imaging radiation-sensitive specimens in a transmission electron microscope under cryogenetic conditions (Milne et al., 2013). Although many protein

structures have already been resolved with this method, viral K^+ channels are too small to be analyzed with cryo-EM.

At this point structural information on Kcv channels stems mostly from homology models, which were generated on the basis of the structure of KirBac1.1 (PDB code: 1P7B Kuo et al., 2003) as template. The actual structural differences between the two similar channels cannot be fully clarified with these methods or with the homology structures.

Molecules which are able to block pores can provide information about the permeation pathway and gating properties. Quaternary ammonium ions (QAs) belong to a family of K^+ channel blockers that have been successfully used in structure and function studies (Hille, 2001). In particular, they provide information and properties of the pore (French & Shoukimas, 1981; Guo & Lu, 2001). They have also been used to understand the first mechanism of an activation gate in a voltage dependent K^+ channel (Armstrong & Hille, 1972). The available data advocate a model in which these compounds block the ion pathway and thus prevent the movement of the K^+ ions. Specifically, the internal block is based on the hydrophobicity of the blockers. The permeating ions also play an important role in the binding of the blocker. This occurs either by direct competition for the binding site or by electrostatic repulsion (Hille & Schwarz, 1978; Thompson & Begenisich, 2000). The cytosolic pore must have at least a diameter of 9 Å for TEA to enter (Armstrong, 1971). Subsequent studies used increasingly larger symmetrical and asymmetrical QA ions to probe the pore of K^+ channel. They found out that even larger blockers can enter the pore (Armstrong & Hille, 1972; French & Shoukimas, 1981).

In this study, different QA derivatives with variable diameters will be used to gain information about the structure of the intracellular pore entrance and of the cavity of the viral potassium channels Kcv_{NTS} and Kcv_S. This method has already been used to examine the *Shaker* Δ6-46 channel, a member of the Kv family (Choi et al., 1993; Piechotta et al., 2011), the Kir channels IRK1 and ROMK-1 (Guo & Lu, 2001; Oliver et al., 1998; Piechotta et al., 2011; Spassova & Lu, 1998) and three K2P channels (Piechotta et al., 2011). Furthermore, the intracellular pore entrance of the TRPV-1 channel before a crystal structure existed was investigated with this method (Jara-Oseguera et al., 2008). QAs have also been used to elucidate the unique pore properties of the BK channel (Li & Aldrich, 2004).

2.3 Results and Discussion

Orientation of viral potassium channels in planar lipid bilayer

Before quaternary ammonium cations can be used to examine the intracellular pore entrance of viral potassium channels, the orientation of the channel in planar lipid bilayer must be determined first. It has to be clarified whether the intracellular part of the protein is oriented towards the *cis* or *trans* chamber. In measurements of Kcv channel activity with the planar lipid bilayer method, the characteristic flicker gating of the viral potassium channels always occurs at negative voltages. It results in a decrease of the apparent current amplitude and has its origin in a medium fast gating behavior of the channel with dwell-times in the closed state between 40 to 150 µs. This gating beyond the corner frequency of the set-ups low-pass filter (1 kHz) can no longer directly be resolved by the recording equipment. Instead it causes an increased open channel noise (Gazzarrini et al., 2009; Schroeder, 2015; Rauh et al., 2017 & 2018). The exclusive occurrence of this fast gating at negative voltages after adding the protein from the *trans* side leads to the conclusion that the channels always insert in the same way into the membrane. From the bilayer recordings alone, it cannot be said whether the flicker gating reflects inward or outward current. But when the bilayer data are compared with measurements of the same channels in mammalian cells it occurs that the electrical properties of the channel in the bilayer are equivalent to those in cells when we assume that the channel protein enters the membrane preferentially with the cytosolic ends of the protein first (Rondelli et al., 2018). Hence the intracellular part of the protein is oriented towards the *cis* chamber.

A chemical modification method was used to confirm this hypothesis. Methanethiosulfonates are common water-soluble sulfhydryl-modifying reagents that can react with cysteine residues (Rassendren et al., 1997). A cysteine was introduced at either the intra- or extracellular pore entrance of Kcv_{NTS} (Fig 2.2A). In the context of the aforementioned orientation this means, that the mutant Kcv_{NTS} T53C has the cysteine directed towards the extracellular side and thus to the *trans* chamber. On the other hand, the mutant W82C has its cysteine oriented towards the cytosol, which should face the *cis* chamber. After the successful incorporation of the channel protein into the bilayer the cation (2-(trimethylammonium)ethyl) methanethiosulfonate (MTSET; bromide salt) was added into either the *cis* or *trans* chamber.

After the addition of 0.4 mM MTSET on the *trans* side, the inflow and outflow of Kcv_{NTS} T53C was almost completely blocked (Fig. 2.2B). In contrast, when MTSET was added on the *cis* side, no reduction of the current could be observed (not depicted). Therefore, MTSET only reduces the current flow when it is added on the side where the accessible cysteine is near the pore entrance. This confirms that Thr^{53} is indeed located within the *trans* chamber.

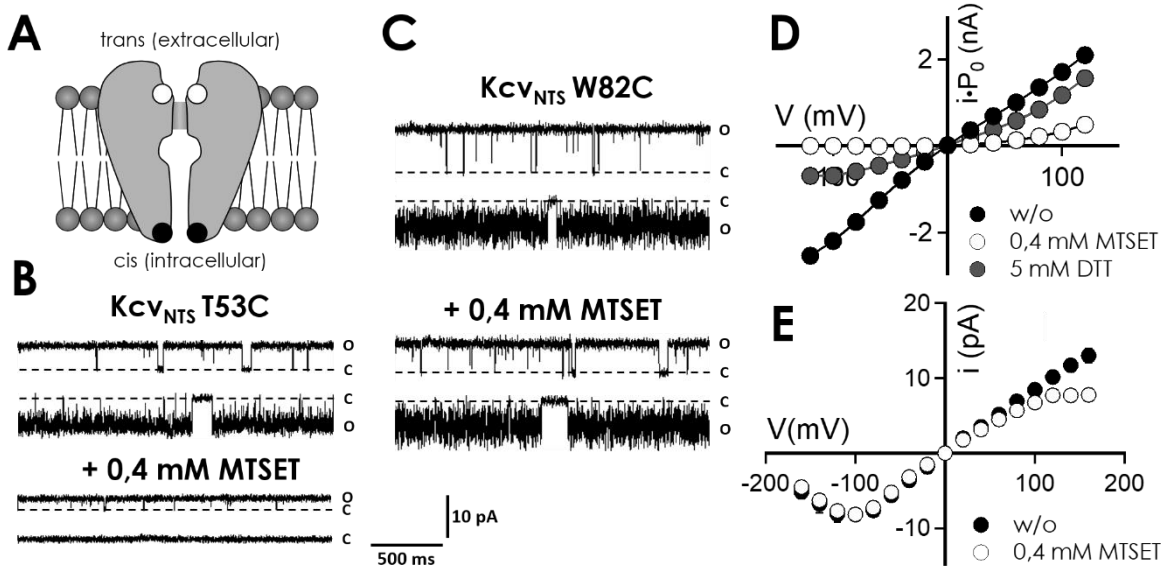

Figure 2.2: Orientation of Kcv channels in planar lipid bilayer. (A) Sketch of the orientation in the membrane. Position 53 is marked with the white circles and position 82 is marked with the black circles. Single channel fluctuations in planar lipid bilayers of Kcv_{NTS} T53C (B) and Kcv_{NTS} W82C (C) w/o and with MTSET. The closed **C** and open **O** levels are indicated along the current traces. The membrane voltage for the upper traces is 120 mV and -120 mV for the lower traces. (D) Steady-state I/V relations from multichannel measurement of Kcv_{NTS} T53C before (black) and after (white) addition of 0.4 mM MTSET into the *trans* chamber. After adding 5 mM DTT on the extracellular side (grey) the amplitude partially recovers. (E) i/V-relations of single channel measurements of Kcv_{NTS} W82C before (black) and after (white) treatment with 0.4 mM MTSET in the *cis* chamber. Raw data of D can be found in the appendix.

Previously, the reduction of channel conductance after the addition of extracellular MTSET has already been observed in the related viral potassium channel Kcv_{PBCV-1} with the mutation L70C in the extracellular loop (Tan et al., 2012). The current was reduced by 78% after addition of 0.2 mM MTSET.

Since the currents of Kcv_{NTS} T53C were almost entirely blocked by MTSET, the exact reduction of current was determined using multichannel measurements. This is also possible with the planar lipid bilayer technique (Winterstein et al., 2018). For this issue, the concentration of the protein solution has to be increased by a factor of approximately 100. By using this technique, it is now possible to record currents that otherwise would be hidden in the noise of the single channel recordings. Fig. 2.2D shows current voltage relations of multichannel measurements of Kcv_{NTS} T53C after the addition of MTSET to the (extracellular) *trans* chamber. In agreement with the single-channel recordings, the inward current is completely inhibited at negative voltages. In contrast, the outward current at positive voltages is still observable, in agreement with the minuscule outward current in the single-channel recordings (Fig. 2.2.B). In terms of percentage, the channel is blocked by MTSET at 120 mV by 80% and at -120 mV by 100% in the multichannel recordings.

As an additional control, DTT can be used to disrupt the disulfide bridge between the sulfur atom of the cysteine residue and the reactive group of the MTSET (Fig. 2.2D). As a consequence, the conductance can be partially rescued. In control measurements with the wt-Kcv_{NTS} channel, no change in the conductance could be registered after the addition of MTSET (not depicted). This fact suggests that MTSET cannot react with the wt-Kcv_{NTS}, and that residue 53 at the extracellular pore entrance is oriented towards the *trans* chamber.

To confirm these results, the mutant Kcv_{NTS} W82C was investigated in further experiments. Theoretically, position 82 is arranged at the intracellular pore entrance and should only be accessible from the *cis* chamber. After the addition of 0.4 mM MTSET in the *cis* chamber, a reduction of the conductivity can only be observed at high positive voltages (above 100 mV) (Fig. 2.2E); the relative block at 160 mV is ~ 40%. At negative voltages, there was no block of Kcv_{NTS} W82C by internal MTSET.

Control experiments show that the wt-channels is not sensitive against intracellular MTSET (not depicted), ruling out the possibility that MTSET penetrates the pore and reduces conductivity because of steric reasons. Therefore, the inhibition of the current by MTSET is actually caused by the binding to the free cysteine on the cytosolic side of the channel. In further control measurements MTSET showed no influence on the conductivity of Kcv_{NTS} W82C when added on the *trans* side (not depicted).

Collectively, the results from these experiments have shown that the extracellular part of the protein is oriented towards the *trans* chamber while the cytosolic part is oriented towards the *cis* chamber.

Quaternary ammonium ions block of Kcv channels is voltage dependent

After identifying the orientation of the viral K^+ channels in the planar lipid bilayer, different QAs were used in the following section to investigate structural differences between Kcv_{NTS} and Kcv_S. Specifically, TEA, TPrA, TBA, TPeA, and THxA were employed to determine the effect of the block properties on the blocking kinetics. The diameters of the QA molecules vary from 8 Å for TEA to 11.2 Å for THxA (Table 6.1). The smallest QA TMA was not investigated because the required concentrations would have been higher than the prevailing potassium concentration. Two molecules even larger than THxA found in the literature were also not used. THpA was not available as a Cl^- salt and TOA bears the hazard of artifacts due to its low solubility (Table 6.2).

Fig. 2.3A shows single channel measurements of Kcv_{NTS} before and after the addition of different QAs to the cytosolic solution. All blockers carry a single positive charge and therefore result in a voltage-dependent block, which is stronger at positive membrane voltages. This is illustrated in Fig. 2.3D by means of the time-averaged current (the product of single-channel current (Fig. 2.3B) and open probability (Fig. 2.3C)). This result seems to be in line with the

expected movement of a positively charged blocker, whose movement from internal medium to the blocking site would be accelerated by the electric driving force. However, it will be shown below, that the picture is a little bit more complex. For instance, theoretical analyses show that this assumption is not justified in the case of QAs (Jogini & Roux, 2005). The voltage dependence probably reflects indirect effects caused by the permeating ions and/or the gating of the channel (Faraldo et al., 2007). Unpublished results (Gabriel et al., in preparation) of our group have shown that the ions accumulating at site S4 in the selectivity filter at negative voltages in the blocked state push the blocker away from its binding site, thus increasing the off-rate constant with increasing negative voltages. This voltage-dependence is investigated below.

The smaller blockers TEA and TPrA lead to a fast channel block, visible as a reduced apparent amplitude of the apparent single-channel current (Fig. 2.3B). This phenomenon is similar to the flicker-gating described earlier (Gazzarrini et al., 2009; Schroeder, 2015; Rauh et al., 2017 & 2018). The individual blocking events are shorter than the temporal resolution of the low pass filter. Thus, the actual current amplitude cannot be resolved. A lower amplitude of the apparent current combined with an unchanged open probability of slow gating (P_o) is typical for fast blockers (Hille, 2001). Nevertheless, the rate constants of the TEA and TPrA block can still be determined by extended beta distribution analysis even beyond the limit of direct determination of open-close transitions (Schroeder et al., 2015; Rauh et al., 2017 & 2018). This will be discussed below. After the addition of TEA, also the slow open probabilities are slightly reduced. This could indicate a second binding site with a longer dwell-time.

In contrast to the effect of the small QAs, the block is slower for the larger blockers TBA, TPeA, and THxA. The individual blocking events result in a reduction of the slow open probabilities (Fig. 2.3C).

In addition, the data in Fig. 2.3 also show that the affinity increases with blocker size. The concentration required to block the channel decreases drastically. For example, 2µM THxA suffice to almost completely block the channel at positive voltages, while 10 mM TEA are required for the same effect. Furthermore, the high affinities of the larger blockers argue that the pore entrance might be big enough for all QAs to enter.

Similar effects as listed above for Kcv_{NTS} can also be observed with Kcv_S (Fig. 2.4). Also, with this K^+ channel, the block is voltage dependent. The time-averaged currents are significantly reduced after the addition of QAs on the intracellular side of the channel. Furthermore, the small blockers also lead to an apparent reduction of the current amplitude. After addition of the blockers with a diameter > 9.5 Å (TBA and TPeA) the reduction of the slow open probabilities is detectable due to deceleration of the block.

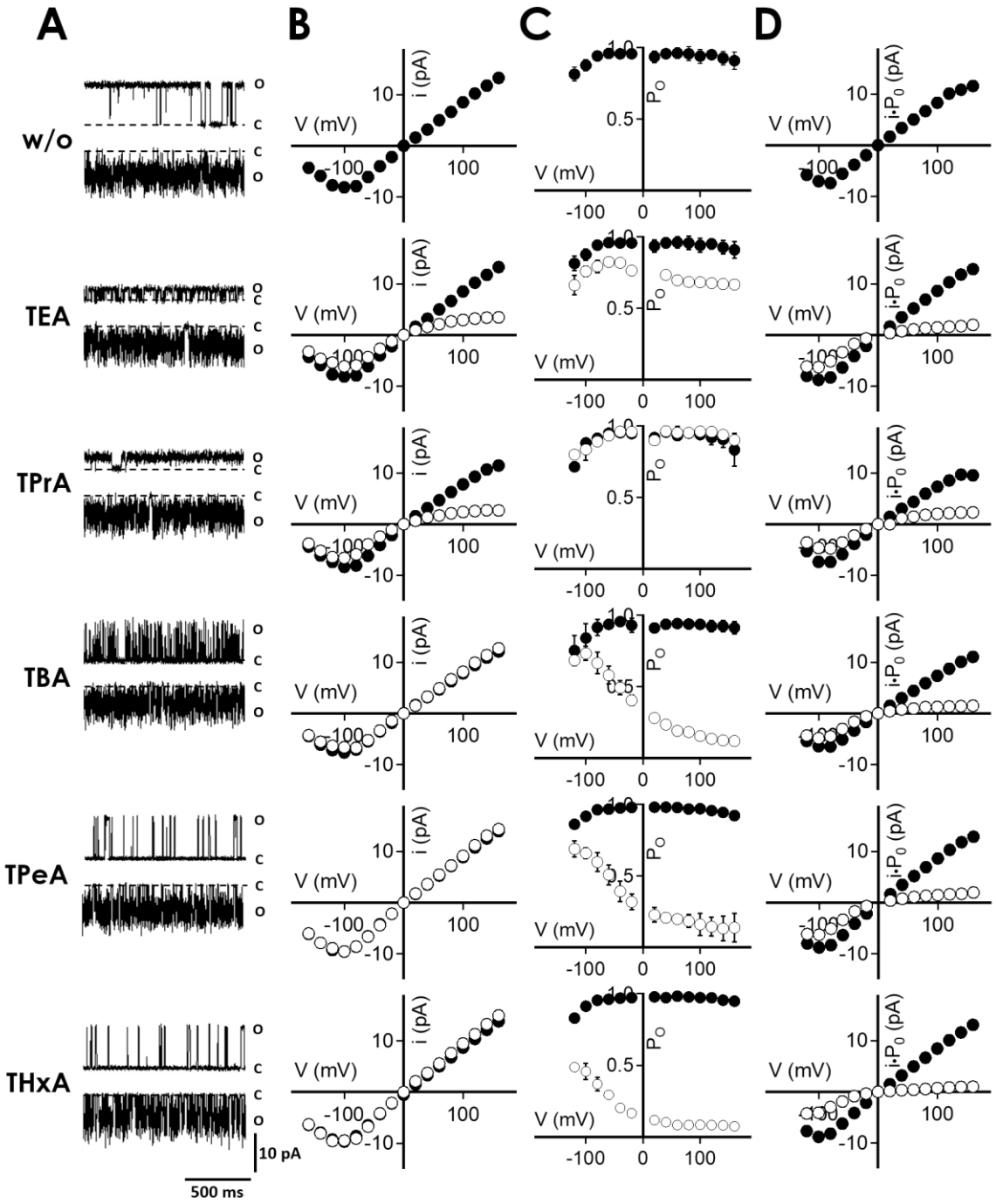

Figure 2.3: Block properties of Kcv_{NTS} by QAs from the cytosolic side. (A) Single channel fluctuations in planar lipid bilayer of Kcv_{NTS} without and with different QAs. The closed **C** and open **O** levels are indicated along the current traces. The membrane voltage for the upper traces is 120 mV and -120 mV for the lower traces. All QAs were added to the *cis* chamber, which faces the intracellular site of the protein. The blocker concentrations are: 10 mM TEA, 1 mM TPrA, 20 µM TBA, 1 µM TPeA, and 2 µM THxA. (B) Unitary channel i/V-relations without (black) and with (white) blocker. (C) Corresponding mean open probabilities and (D) Time-averaged I/V relations. The latter were obtained by multiplying data in B and C. Mean data ± s.d. are from 3 independent recordings. The different QAs block the K^+ channel Kcv_{NTS} in a voltage dependent manner. The larger the diameter of the blocker, the slower the block.

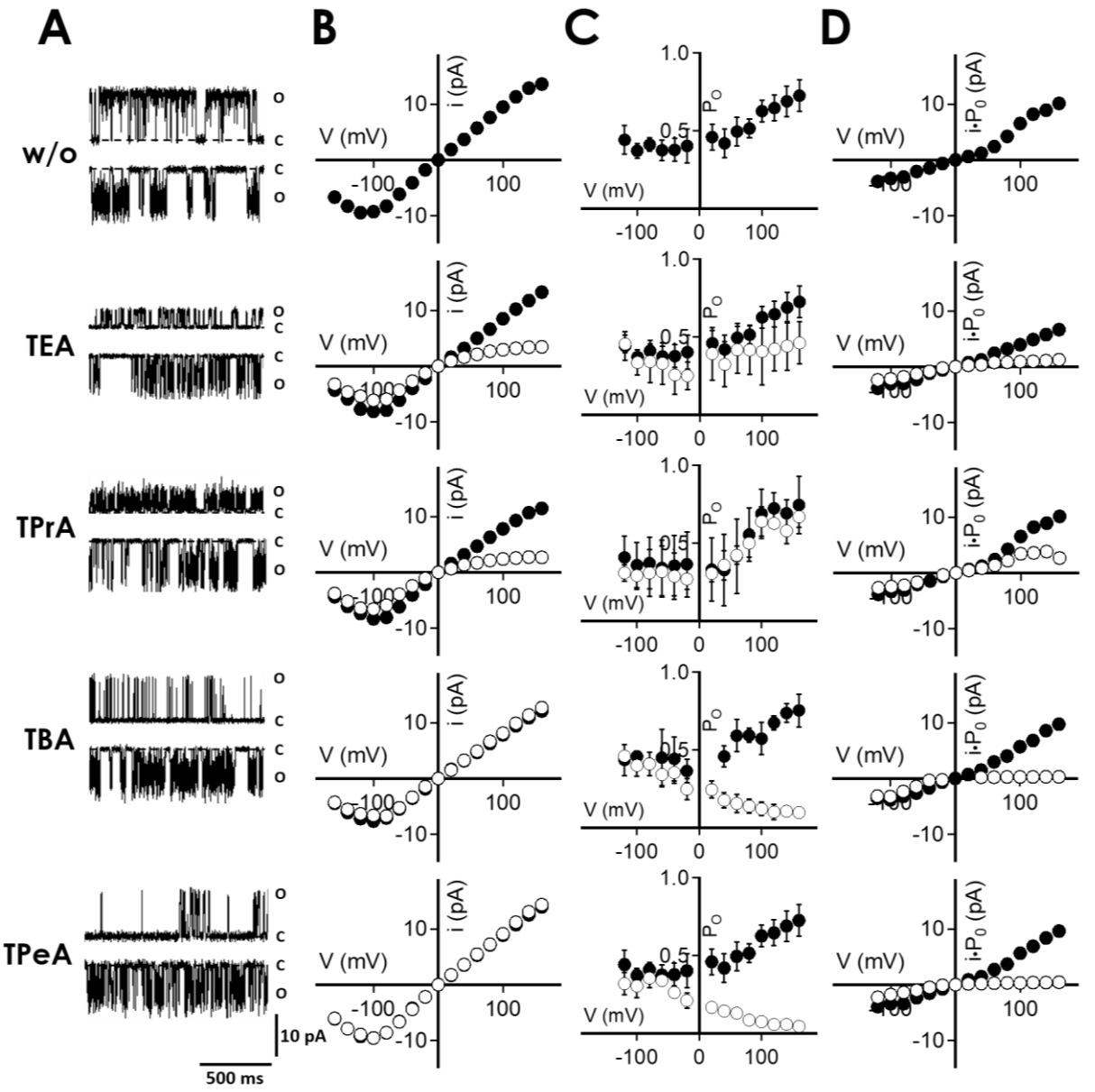

Figure 2.4: Block properties of Kcvs by QAs from the cytosolic side. (A) Single channel fluctuations in planar lipid bilayer of Kcvs without and with different QAs. The closed **C** and open **O** levels are indicated along the current traces. The membrane voltage for the upper traces is 120 mV and -120 mV for the lower traces. All QAs were added to the *cis* chamber, which faces the intracellular site of the protein. The blocker concentrations are: 5 mM TEA, 0.5 mM TPrA, 10 µM TBA, and 1 µM TPeA. (B) Unitary channel i/V-relations without (black) and with (white) blocker. (C) Corresponding mean open probabilities and (D) Time-averaged I/V relations. The latter were obtained by multiplying data in B and C. Mean data ± s.d. are from 3 independent recordings. The different QAs block the K^+ channel Kcvs in a voltage dependent manner. The larger the diameter of the blocker, the slower the block.

Affinity of the block

Blocking of Kcv_{NTS} and Kcv_S by TEA and TPrA is a fast process. As mentioned above, the individual blocking events are of such short lifetime that they cannot be resolved by the recording set-up. As a result, the block appears as an apparent reduction of the single channel current. In order to compare the sensitivity of both channels, dose-response curves were generated by fitting first-order Hill equations (Eq. 2.3) to the data points of this apparent reduction for every voltage step (Fig. 2.5). The Hill factor was set to 1 and each experiment was fitted separately. It was not possible to measure the saturation of the block in all cases, due to the strong reduction in apparent current, resulting in a too small signal-to-noise ratio. Nevertheless, by comparison with those cases, where the saturation could be measured, a maximal block of 100% was assumed for all fits.

The dose-response curves shift with more negative voltages to higher blocker concentrations, indicating a reduction in affinity at negative voltages. The K_D of TEA at 100 mV is 5.5 ± 0.8 mM for Kcv_{NTS} and 3.31 ± 0.9 mM for Kcv_S. Thus, Kcv_S is almost twice as sensitive towards TEA compared to Kcv_{NTS}. In contrast, the *Shaker* channel shows a lower K_D of 0.7 mM (Yellen et al., 1991), i.e. a higher affinity and KcsA a much lower affinity (K_D = 78.4 mM, Kutluay et al., 2005). The same picture occurs with the 1 Å larger TPrA. While the K_D for Kcv_{NTS} is 200 ± 60 µM, Kcv_S is also approximately twice as sensitive with a K_D of 80 ± 30 µM.

In Fig. 2.5G the voltage dependence can be clearly seen. In contrast to other channels, which reach asymptotic values at positive voltages (Jara-Osegura et al., 2007), the K_D decreases in the viral channels further with higher voltages. It is most likely that the saturation will eventually appear at much higher voltages. At negative voltages, the K_D exhibits more of an exponential dependency on the voltage.

As the diameter of the QAs increase, the speed of the block slows down. Starting from TBA with a size of 10 Å, the block can be fully resolved in the time series. Therefore, the K_D values from TBA were no longer determined from the reduced current amplitude as before, but from the reduction of the open probabilities (Eq. 2.3).

Here it should be noted, that in contrast to the current amplitudes, Kcv_{NTS} and Kcv_S differ in their open probabilities due to the inner gate in Kcv_S (Rauh et al., 2017). The long closed events induced by the inner gate reduce the mean open probability from 90% for Kcv_{NTS} to about 50% for Kcv_S. For this reason, the variation of the individual measurements with Kcv_S is significantly higher. Nevertheless, the difference in sensitivity of the two channels to the QAs remains (Fig. 2.6). At a voltage of 100 mV Kcv_{NTS} blocked by TBA has a K_D of 2.5 ± 0.1 µM and Kcv_S a K_D of 1.1 ± 1 µM.

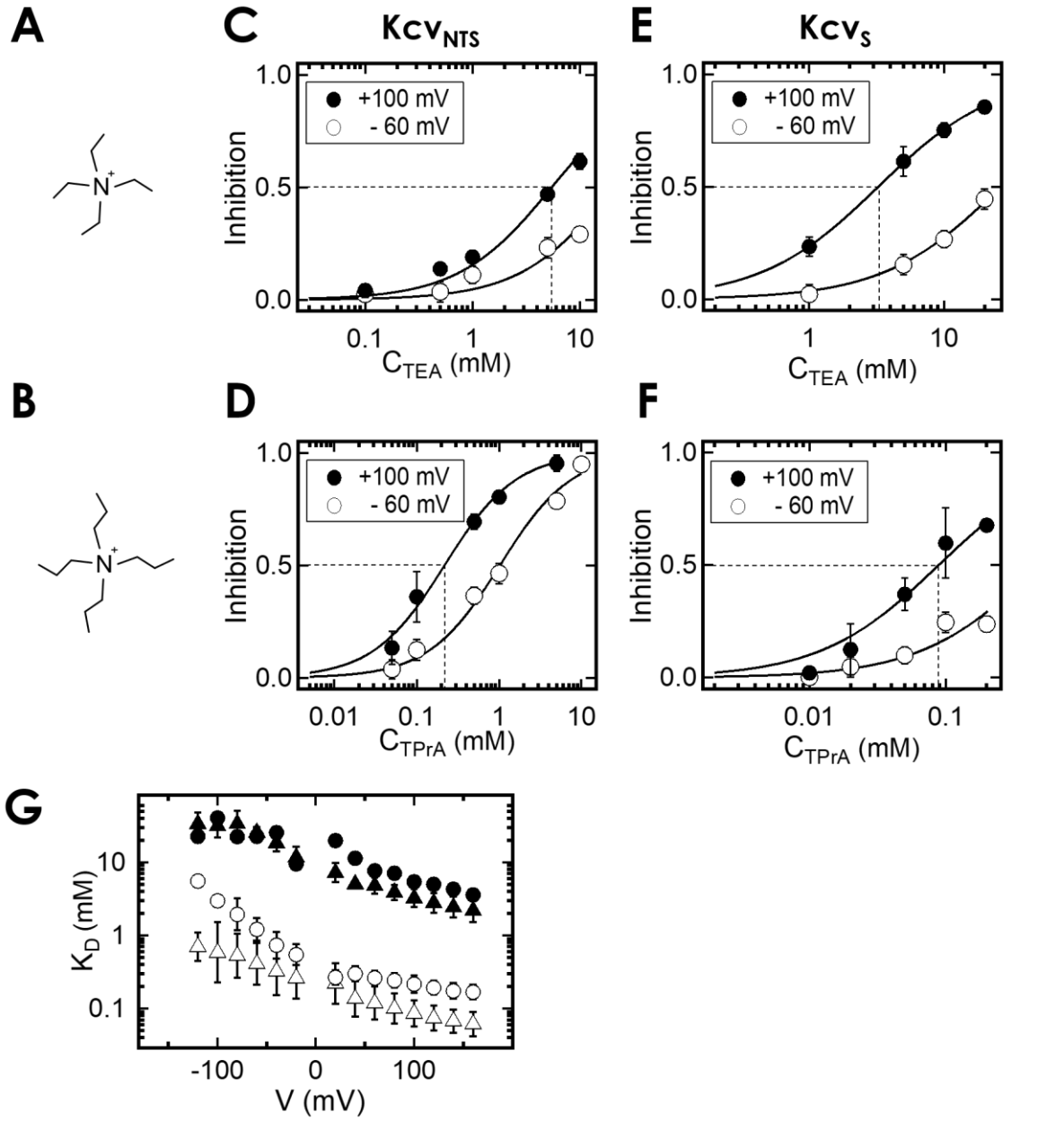

Figure 2.5: Inhibition of Kcv_{NTS} and Kcv_S by fast blocking QAs. Sketch of (A) TEA and (B) TPrA molecules. (C-F) Dose-response-curves at 100 mV and -60 mV of Kcv_{NTS} and Kcv_S with TEA and TPrA, respectively. The solid lines are average curves and represent the fits of data with the Hill equation (Eq. 2.3). Fit parameters are given in the text. The dotted line simplifies the readout of the K_D value at 100 mV. (G) The apparent dissociation constant, K_D, derived from data in C-F at different voltages. Shown is a complete dataset at voltages from -120 mV to 160 mV for recordings with TEA (black) and with TPrA (white). Data from Kcv_{NTS} and Kcv_S are shown by circles and by triangles respectively. Mean data ± s.d. are from 3 independent recordings. The data show the voltage dependence of the block and the increased sensitivity of Kcv_S against the blockers.

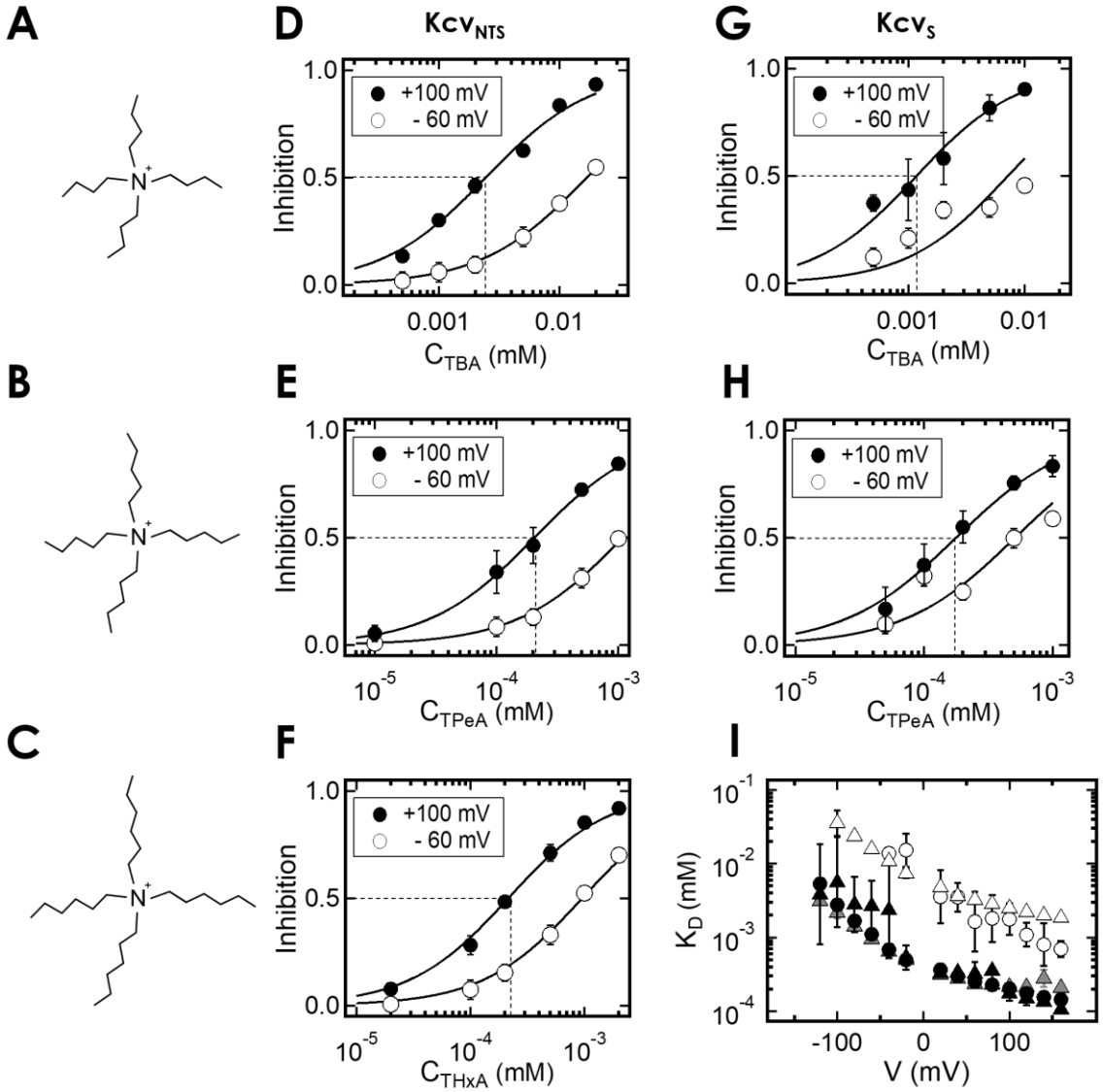

Figure 2.6: Inhibition of Kcv_{NTS} and Kcv_S by slow blocking QAs. Sketch of (A) TBA, (B) TPeA, and (C) THxA molecules. (D-H) Dose-response-curves at 100 mV and -60 mV of Kcv_{NTS} and Kcv_S with TBA, TPeA, and THxA, respectively. The solid lines are average curves and represent the fit of data with the Hill equation (Eq. 2.3). The dotted line simplifies the readout of the K_D value at 100 mV. (I) The apparent dissociation constant, K_D, derived from data in D-H at different voltages. Shown is a complete dataset at voltages from -120 mV to 160 mV. Recordings with TBA (white), TPeA (black), and THxA (grey). Data from Kcv_{NTS} and Kcv_S are shown by triangles and by circles, respectively. Mean data ± s.d. are from 3 independent recordings. The data show the voltage dependence of the block. The sensitivity of the two channels for TPeA is almost identical. There is also no difference between TPeA and THxA for Kcv_{NTS}. Kcv_S is more sensitive to TBA than Kcv_{NTS} as well as regarding the fast blockers (see Fig. 2.5).

Another picture emerges when TPeA is used as a blocker. In this case there is no longer a difference between the affinity of both channels (Fig. 2.6). The K_D values at 100 mV are 0.2 ± 0.06 µM for Kcv_{NTS} and 0.17 ± 0.04 µM for Kcv_S.

Experiments were also carried out with the next larger THxA with the Kcv_{NTS} channel. It is noticeable that there is no further reduction of the K_D, which is 0.21 ± 0.01 µM at 100 mV. The sensitivity of Kcv_{NTS} for TPeA and THxA is therefore almost identical. Based on these results, the experiments with THxA were not performed with Kcv_S anymore.

The data raise the question of whether the inner gate is responsible for the slightly increased affinity of Kcv_S for TEA and TPrA or whether there are other structural differences, causing this effect. To address this question, we decompose the K_D value into its individual components. Since the K_D is the ratio of the blocker dissociation rate (k_{BO}=k_{off}) divided by the association rate (k_{on}), a larger K_D value can be caused by either a larger k_{off} rate or a smaller k_{on} rate. In the following, the rate constants were calculated.

Determination of the rate constants

The kinetic behavior of ion channels as related to gating or blocking results from stochastic jumps between different conducting (open) and non-conducting (closed) states. For instance, the rate constant of blocker dissociation indicates how many molecules per second can dissociate from the channel. The inverse value, mean lifetime τ_B, is the average time the blocker spends at its binding site. The rate constant of blocker associations gives the average number of blocker associations per second. These processes are mathematically described by Markov models.

Fig. 2.7 shows different Markov models relevant for the analysis of the blocking effects. From the analyses in Rauh et al. (2017 & 2018), 5 closed states of the intrinsic channel gating with different dwell-time and one open state are known. For the data analysis here, this model is supplemented by a blocked state B (Fig. 2.7A). However, depending on the time scale of blocking, smaller models can be used.

If the blocking events are faster than resolution of the recording equipment, they can be resolved by full open-closed transitions, they have to be analyzed by extended beta distributions (Schroeder, 2015; Rauh et al., 2017 & 2018). However, this kind of analysis cannot distinguish between the different long closed state. Thus, they are merged in one slow state S for the analysis of the fast kinetic by beta distributions (Fig. 2.7B).

On the other hand, if the blocking events are slow enough that they accessible to dwell-time analysis (see below), the model in Fig. 2.7D can be used. The fast intrinsic gating (O-F and O-M) is now merged into the open state O, since it is invisible to the dwell-time analysis. This

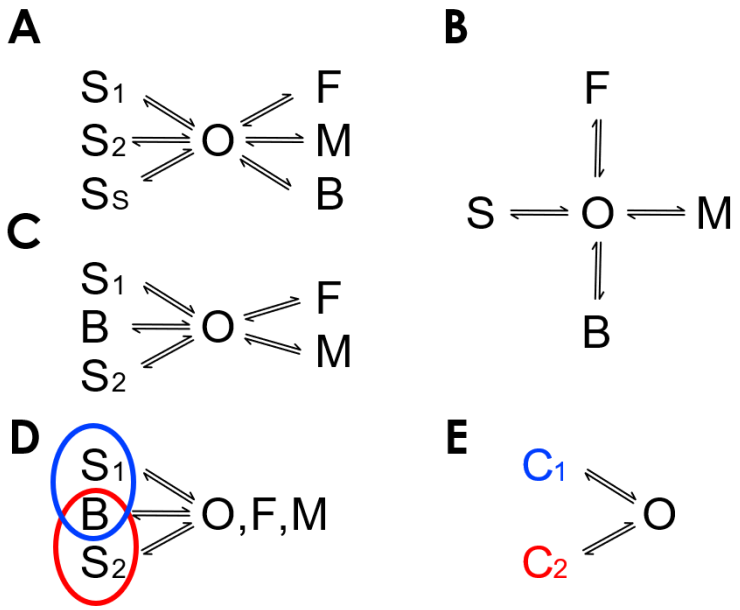

Figure 2.7: Markov models used for fitting the blocking kinetics. (A) The full Markov model with all states as known so far from previous studies from Rauh et al. (2017 & 2018) supplemented by the blocked state B. The closed states S_1, S_2, S_S belong to slow gating, which can be revealed by level detectors in the measured time series. F and M belong to fast gating (dwell-time in the closed state about 5 µs) and medium gating (dwell-time in the closed state about 50 µs). (B) The model used for the analysis of fast gating. The states S_1, S_2 and S_S cannot be resolved by this analysis. (C) The full model for the slow gating. S_S is omitted because it did not occur in our experiments. (D) In the experiments, the dwell–time in B happened to coincide with that of either S_1 or S_2. Thus, only two closed states occur in the measured dwell-time histogram. (E) The model used for fitting dwell-time histograms. The colors correspond to those used in Fig. 2.12, below.

merging is indicated by the circles in Fig. 2.7D. The long closed state S_S, which normally is found in Kcv_S (Rauh et al., 2017) is omitted, because it did not appear in the experiments here. The shorter closed states S_1 and S_2 are found in both Kcv_{NTS} and Kcv_S (Rauh et al., 2017).

When a slow blocker (e.g. TPeA) is added, an additional non-conducting state B should appear. However, it turned out in the analysis below, that the slow blockers happen to have a dwell-time which coincides with that one of either S_1 or of S_2 and is thus not separable in the dwell-time analysis, below. Therefore, B is merged into S_1 or into S_2 during the dwell-time analysis (circles in Fig. 2.7D). For this reason, the fits of dwell-time histograms use the simplified 3-state model with the closed states C_1 and C_2 and the apparent open state O. In the individual experiments is has to be determined whether B is included in C_1 or C_2.

As mentioned above, the analysis of the kinetics of the slow block as caused by TBA and TPeA have to be based on dwell-time analysis. Fig. 2.8 and Fig. 2.9 show dwell-time histograms obtained from Kcv_{NTS} and Kcv_S before and after the addition of different TBA concentrations measured at 100 mV (white) and -60mV (grey). For the analysis, the 3-state Markov model in

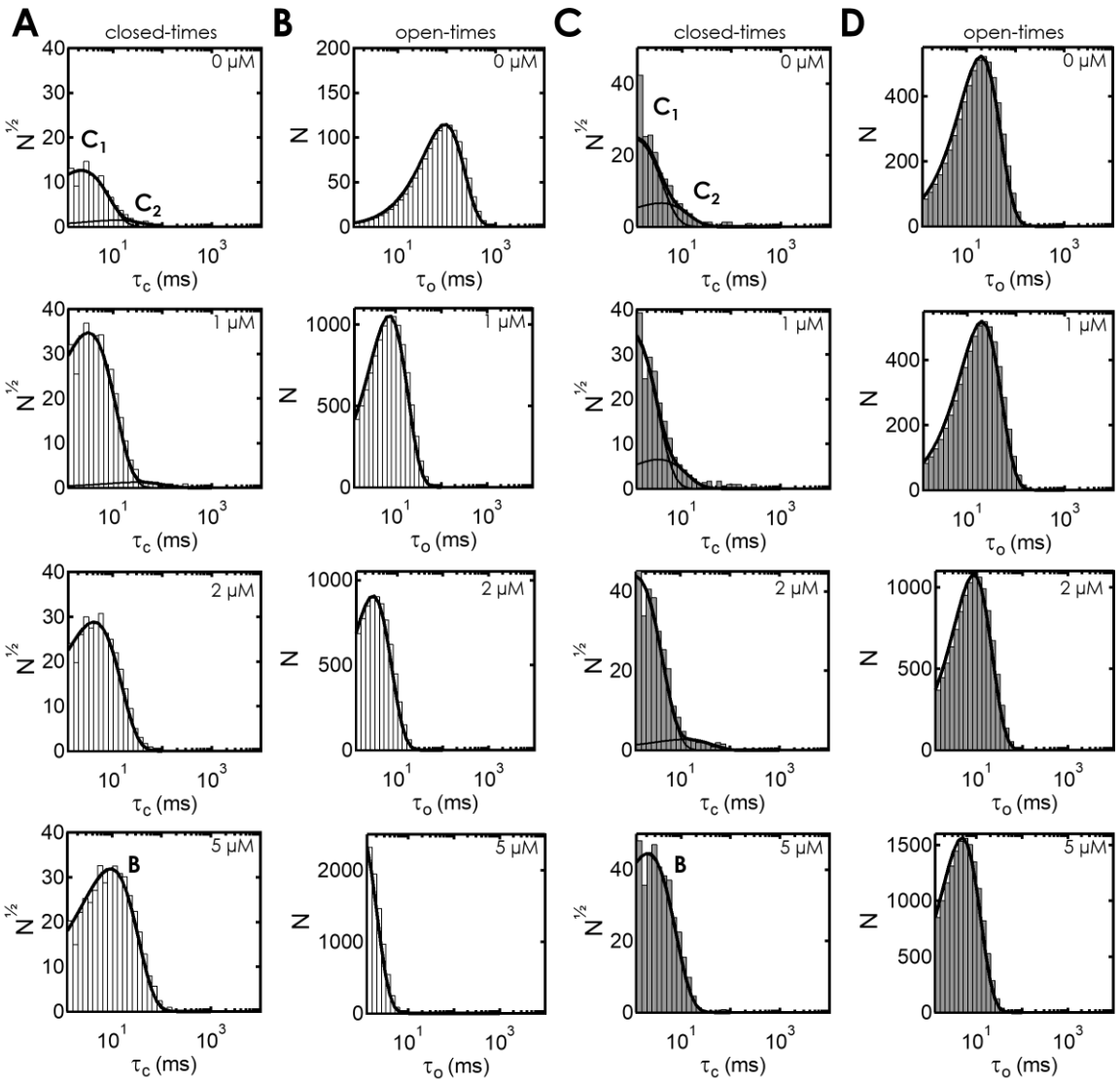

Figure 2.8: Dwell-time analysis of Kcv_{NTS} in absence and presence of TBA. Exemplary closed-time (A) and open-time histograms (B) at 100 mV (white) and exemplary closed-time (C) and open-time histograms (D) at -60 mV (grey). The first row shows data without blocker, the second with 1 µM, the third with 2 µM, and the fourth with 5 µM TBA. The data in A&C are fitted with the sum of two exponential functions while the data in B&D only require a single exponential function. The two closed states are indicated by C_1 and C_2, the blocked state is indicated by B.

Fig. 2.7E is used. Thus, the closed dwell-time histograms have to be fitted by two exponentials and the open dwell-time histogram by one exponential.

An inspection of the dwell-time histograms shows that the blocking kinetics in Kcv_{NTS} (marked B in Fig. 2.8) are merged into the O-S_1 kinetics, i.e, they are included in C_1, because this component increases with increasing TBA concentration. With increasing TBA concentration in Kcv_{NTS} (Fig. 2.8), the mean open-time is reduced because of the rising amount of blocking events. Therefore, also the total number of open events increases. At 5 µM TBA the

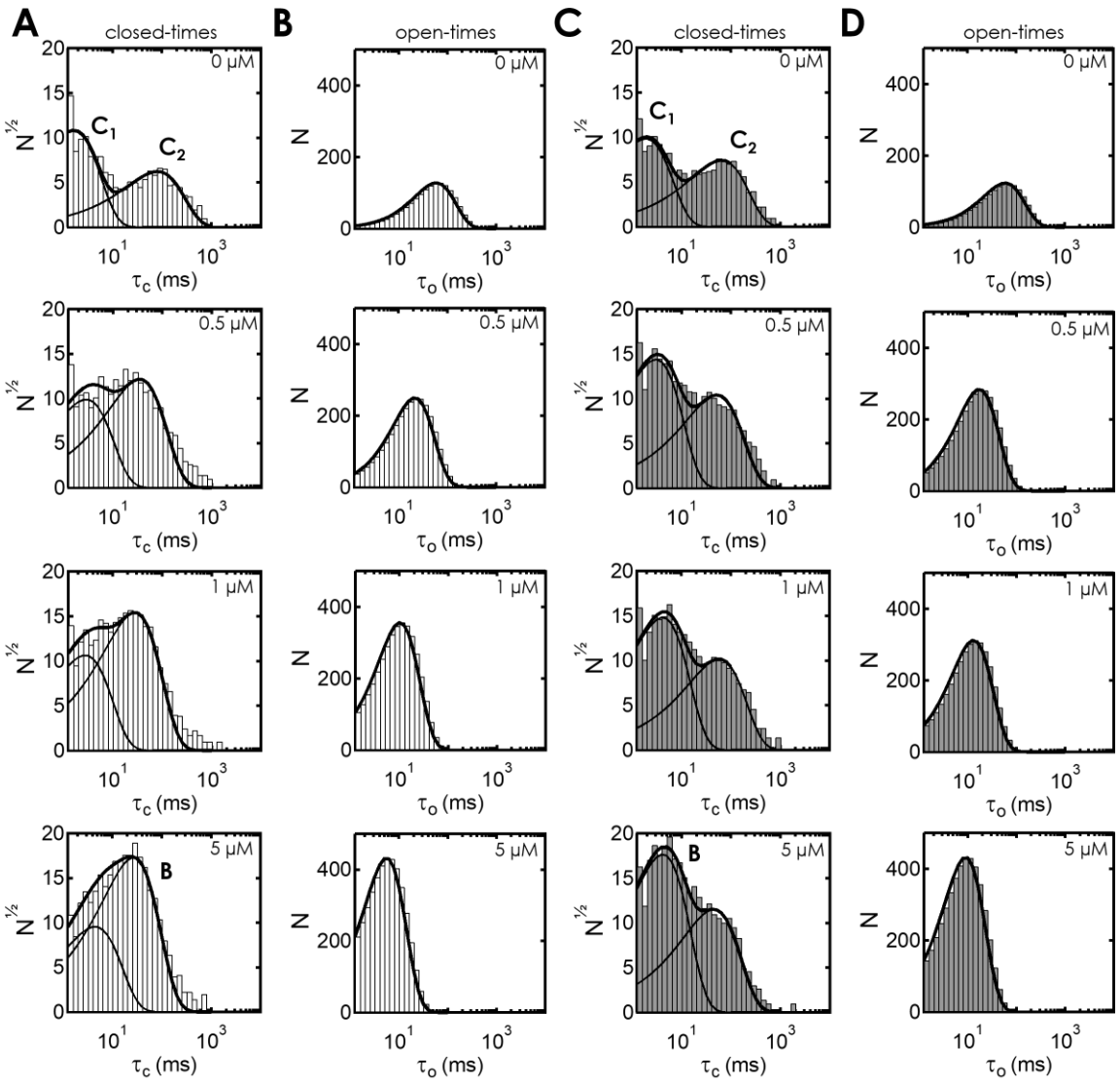

Figure 2.9: Dwell-time analysis of Kcv$_S$ in absence and presence of TBA. Exemplary closed-time (A) and open-time histograms (B) at 100 mV (white) and exemplary closed-time (C) and open-time histograms (D) at -60 mV (grey). The first row shows data without blocker, the second with 0.5 µM, the third with 1 µM, and the fourth with 5 µM TBA. The data in A&C are fitted with the sum of two exponential functions while the data in B&D only require a single exponential function. The two closed states are indicated by C_1 and C_2, the blocked state is indicated by B.

block gets so fast that some of the events cannot be detected by the filter and the left shoulder of the open-time histogram shifts out of the frame.

The dwell-time histograms of Kcv$_S$ at different TBA concentrations show a different picture (Fig. 2.9). The lifetime of the block is much longer than for Kcv$_{NTS}$, overlapping with C_2. This results in a marked increase in the apparent population of C2 at both 100 mV and -60 mV. Also, Kcv$_S$ shows an increasing shift of the open states to shorter times when the number of blocking

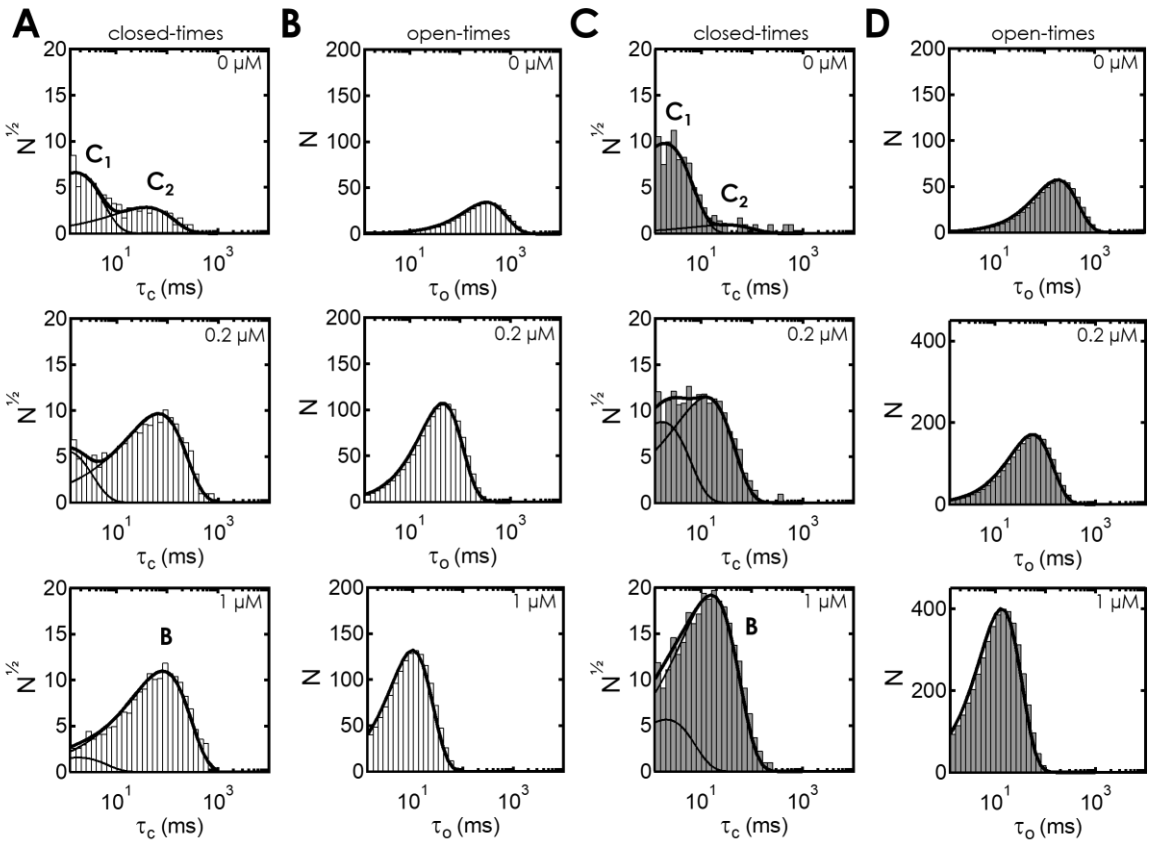

Figure 2.10: Dwell-time analysis of Kcv_{NTS} blocked by TPeA. Exemplary closed-time (A) and open-time histograms (B) at 100 mV (white) and exemplary closed-time (C) and open-time histograms (D) at -60 mV (grey). The first row shows data without blocker, the second with 0.2 µM, and the third with 1 µM TPeA. The data in A&C are fitted with two exponential functions while the data in B&D only require a single exponential function. The two closed states are indicated by C_1 and C_2, the blocked state is indicated by B.

events increases with higher TBA concentrations. Furthermore, the voltage-dependent behavior of the block is well visible, since the effect is weaker at -60 mV.

The same dwell-time analysis was also performed with the approximately 1 Å larger molecule TPeA (Fig. 2.10 & 2.11). Here, the blocking kinetic are merged in the S_2 gating for both, Kcv_{NTS} and Kcv_S. For Kcv_S, even at high concentrations, C_1 and B can still be clearly separated in contrast to Kcv_{NTS}. One reason for this is the higher occupancy of C_1 in Kcv_S under control conditions. At high concentrations of TPeA, C_2 completely dominates. In all cases, there is no difference between the experiments at 100 mV and -60 mV with respect to the merging of the TPeA block with C_2 gating.

In order to gain more precise insights about the exact change of the different populations, the occupation probabilities of the individual states of the model in Fig. 2.7E in relation to the concentration of the blockers were plotted (Fig. 2.12). They were calculated by a custom-made Matlab script (provided by O. Rauh; see Methods).

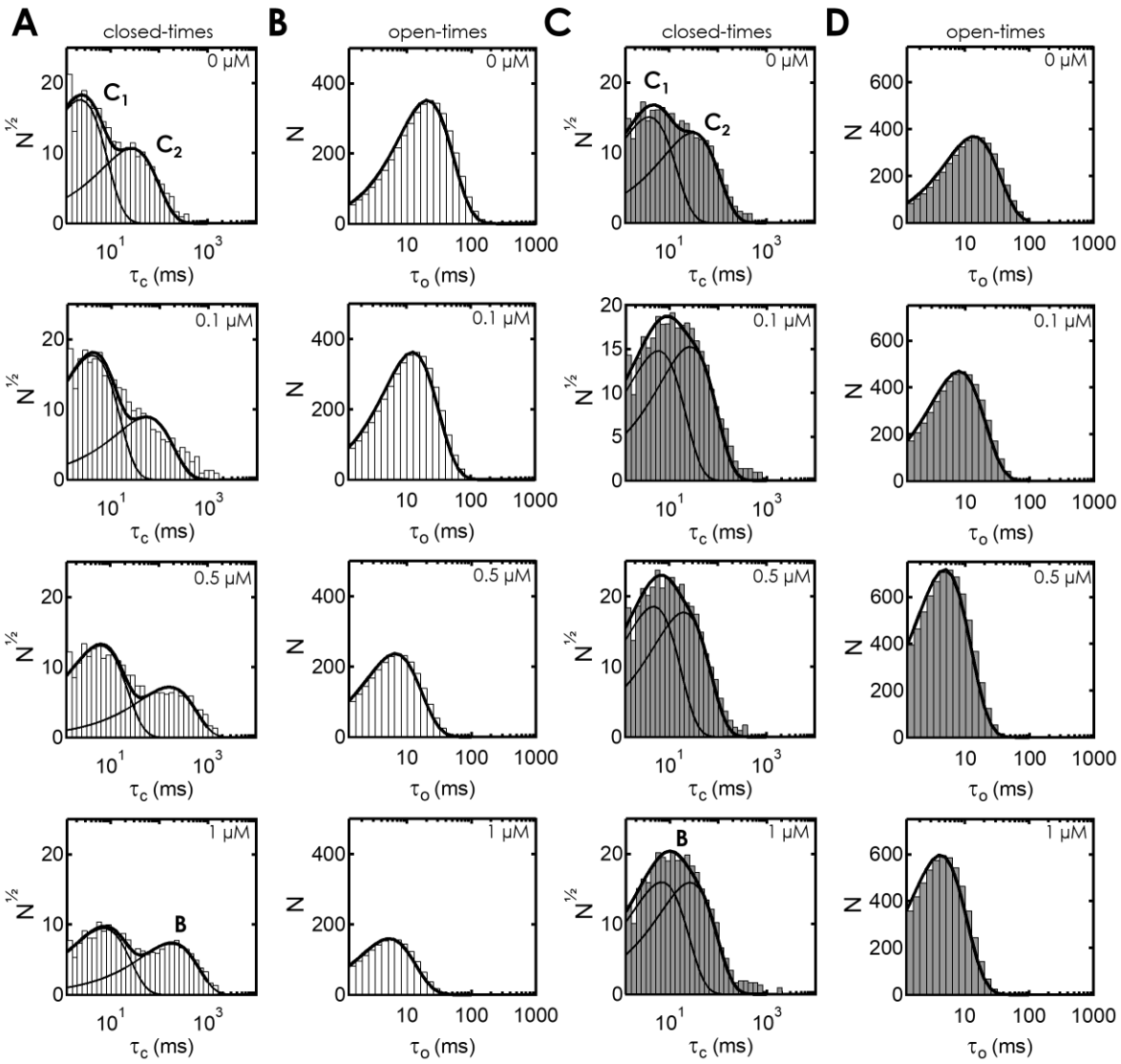

Figure 2.11: Dwell-time analysis of Kcv_S blocked by TPeA. Exemplary closed-time (A) and open-time histograms (B) at 100 mV (white) and exemplary closed-time (C) and open-time histograms (D) at -60 mV (grey). The first row shows data without blocker, the second with 0.1 µM, the third with 0.5 µM, and the fourth with 1 µM TPeA. The data in A&C are fitted with two exponential functions while the data in B&D only require a single exponential function. The two closed states are indicated by C_1 and C_2, the blocked state is indicated by B.

As mentioned above, TBA leads to a faster block in Kcv_{NTS}. Therefore, it is the probability of C_1 occupation (Fig. 2.7D blue), which increases significantly with rising blocker concentration. In contrast, the block in Kcv_S is slower, which brings the dwell-time in B close to that in S_2 and thus causes an increase in the occupation probability of C_2 (Fig. 2.7 red). At negative voltages both channels show a similar picture as at positive voltages. However, the quantity of the block is much lower due to the voltage dependency.

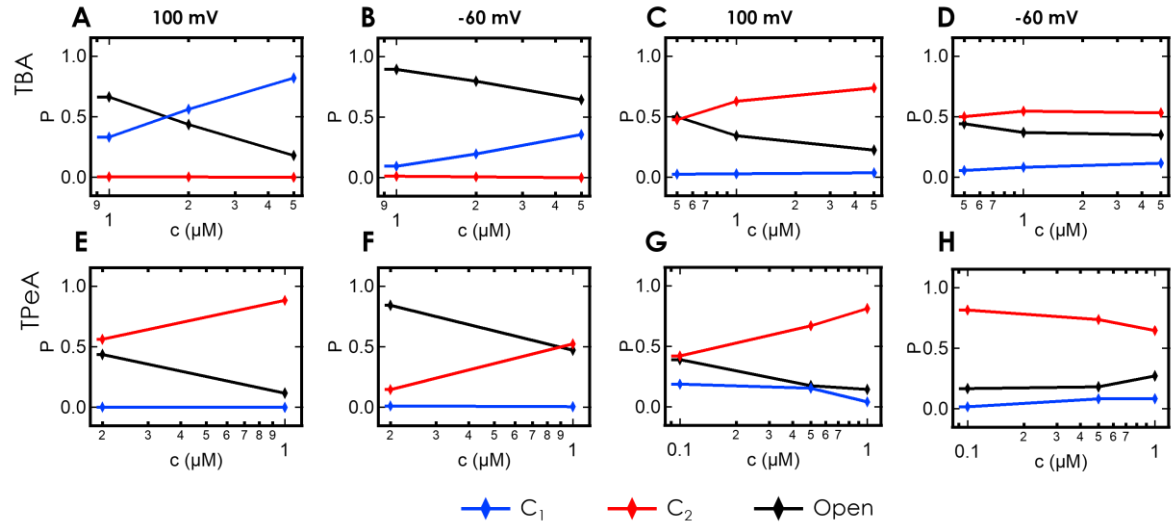

Figure 2.12: Occupation probabilities of different open and closed states in the Markov model of Fig. 2.7E. Shift in the occupation probabilities of the two K^+ channels Kcv_{NTS} and Kcv_S after addition of the blockers TBA and TPeA at 100 mV and -60 mV. Shown are data from: Kcv_{NTS} with TBA (A&B), Kcv_S with TBA (C&D), Kcv_{NTS} with TPeA (E&F), and Kcv_S with TPeA (G&H). The channels occupy three different states, one open state P_O (black) and two closed states P_{C1} (blue), and P_{C2} (red).

For TPeA, the characteristic of the block is similar for both channels. The reduction of the reaction speed (Fig. 2.10 & 2.11) due to the increased diameter of the molecule leads to an increase in the occupation probability of C_2.

The mechanistic background of the block leading to the occupation probabilities in Fig. 2.12 is provided by the rate constants of the Markov model. In the case of slow gating, these rate constants are obtained from the fit of the dwell-time histograms in Fig. 2.8 – 2.11 on the basis of the Markov models in Fig. 2.7E. The interest of this study is not the intrinsic gating, which is known from studies before (Rauh et al., 2017 & 2018), but in the rate constants of blocking. Thus, the individual contribution of blocking to the rate constants for the merged closed states C_1 and C_2 has to be determined.

At TPeA concentrations of 2 µM (Kcv_{NTS}) and 1 µM TPeA (Kcv_S), the integral over the C_2 histogram is much larger than without blocker. Therefore, it is assumed here, that k_{OC2} is a reasonably approximation for k_{OB} for TPrA. From this rate constant, the association rate can be calculated by $k_{on} = k_{OB} / [TPrA]$. In Fig. 2.13F, it can be seen that k_{on} for TPeA is identical for both Kcv_S and Kcv_{NTS}. Likewise, k_{C2O} can be used as an approximation of the dissociation rate k_{BO}. Here, we see a slightly faster dissociation of TPeA in Kcv_{NTS} than in Kcv_S (Fig. 2.13E), Thus the slightly lower sensitivity to TPeA found in Kcv_{NTS} compared to Kcv_S results from a difference of the dissociation rate constant, not of the binding rate constant.

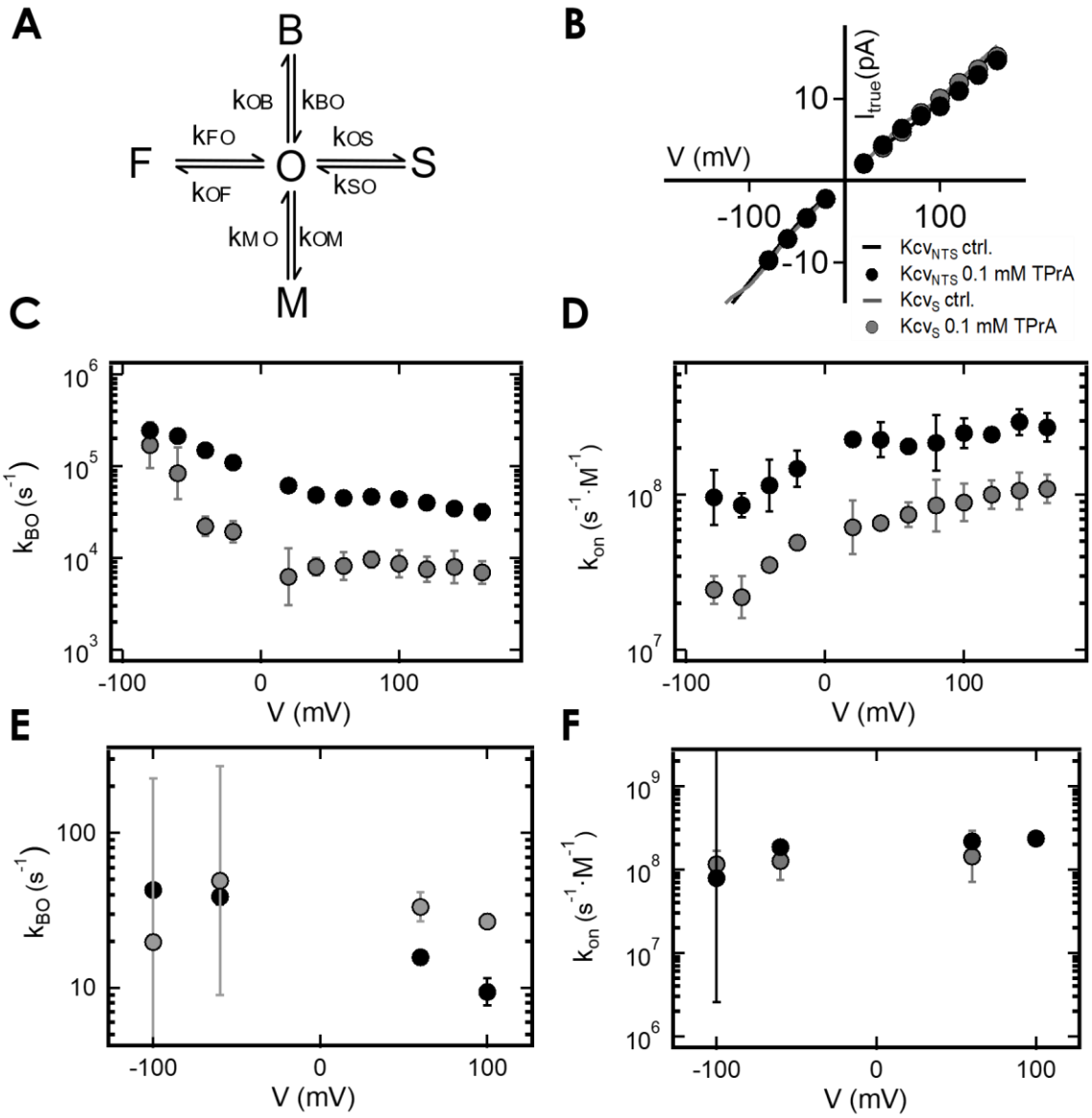

Figure 2.13: Kinetics of block of Kcv_S (grey), and Kcv_{NTS} (black). (A) Markov model of intrinsic gating (O, F, M, S) and blocking (O, B) for the beta fit analysis. (B) i/V relations of the influence of TPrA on the true single-channel current. (C) Dissociation rate (k_{OB}) and (D) association rate (k_{BO}) measured between -80 and 160 mV. The concentration for both channels is 0.1 mM TPrA. Data determined from extended beta distributions. (E) Dissociation rate and (F) association rate of the TPeA block. Data determined from dwell-time analysis ($k_{on}=k_{OB}$/Blocker). The concentrations are 2 µM for Kcv_{NTS} and 1 µM for Kcv_S. Mean data ± s.d. are from 3 independent recordings.

In case of fast blockers, e.g. TPrA, the rate constants cannot be determined by dwell-time analysis and have to be derived from beta distribution. The model in Fig. 2.7B is used to fit the measured amplitude histograms by a theoretical amplitude histogram. It includes three intrinsic gating processes (fast O-F gating, medium O-M gating, slow O-S gating) and the blocking

process O-B. The fit algorithm adjusts the rate constants of the intrinsic gating and the blocking until the measured and theoretical amplitude histograms coincide (see Methods).

Figure 2.13 shows the results from extended beta distribution analysis for Kcv_S (grey) and Kcv_{NTS} (black) with 0.1 mM TPrA. The true single channel current, I_{true}, (Fig. 2.13B) is not affected by the blocker in Kcv_S and Kcv_{NTS}. The true single channel current is the current, which would be measured in a (normally unaccessible) very short time interval not disrupted by any gating or blocking. It can only be revealed by extended beta distributions (Schroeder, 2015). The exact determination of the intrinsic gating is hampered by the dominating blocking kinetics. Basically it is not strongly influenced (data not shown), but that still has to be further elaborated and will be published in a separate forthcoming paper.

In contrast, the determination of the blocking kinetics is highly reliable at positive voltages. At negative voltages, it suffers from the strong decrease of the blocking effect as already visible in the K_D shown in Fig. 2.5D&E. Fig. 2.13C&D shows the rate constant of blocker dissociation k_{BO} and the blocker association rate k_{on} for Kcv_{NTS} and Kcv_S. In contrast to the results for the slow blocker TPeA, both blocker association and dissociation of TPrA are slower in Kcv_S by an almost constant factor than in Kcv_{NTS}, thus leading to an apparent parallel shift on the logarithmic scale. In detail, this shift is not complete in parallel. At 0.1 mM TPrA, blocker association rate k_{on} of Kcv_{NTS} at negative voltages is 3 times higher than that of Kcv_S and 2.5 times higher at positive voltages. The rate constants of unblocking k_{BO} of Kcv_{NTS} at negative voltages are seven times higher than that of Kcv_S and four to five times higher at positive voltages. Thus, both blocking and unblocking is slower in Kcv_S than in Kcv_{NTS}.

Even though the rate constants of blocking in Kcv_{NTS} are faster than those in Kcv_S, Kcv_{NTS} is less sensitive to the blocker than Kcv_S. This results from the finding in Fig. 2.13C&D that the increase in k_{BO} over that in Kcv_S is higher than the increase in k_{OB}, the rate constant of blocker binding. The probability of the blocked state can be calculated from the ratio of the two rate constants:

$$p(O) = \frac{k_{OB}}{k_{OB} + k_{BO}} = \frac{k_{OB}}{(k_{on} \cdot [TPrA] + k_{BO})} \qquad \textbf{(2.1)}$$

This is the origin of the finding of a higher K_D for Kcv_{NTS} as compared to Kcv_S obtained from the experiments in Fig. 2.5G.

The voltage dependence of k_{BO} shows an increase with negative voltages. The origin of the voltage dependence of k_{BO} is as follows: k_{BO} is accelerated by the electrostatic repulsion between the positively charged blocker and the positively charged K^+ ion at the S4 site of the selectivity filter. This repulsion becomes significant at negative voltages, when the occupation probability of site 4 increases with increasing negative voltages (Gabriel et al., in preparation).

The inner gate plays a major role in QA blocking kinetics

Although Kcv_{NTS} and Kcv_S have an amino acid identity of approximately 80%, they show major differences in their electrophysiological properties. The presence of an inner gate in Kcv_S leads to a reduced open probability, since the closing events of this gate are significantly longer compared to the selectivity filter gates common with Kcv_{NTS} (Rauh et al., 2017). Without this additional inner gate, Kcv_{NTS} possesses an average open probability of 90% while the presence of the inner gate lowers the open probability of Kcv_S to approximately 50%. The inner gate is formed by Phe^{78}. If the large aromatic side chain of this amino acid is removed by mutating the residue 78 into Ala, then the gate is abolished, and Kcv_S does no longer show the long closed events; the mean open probability of the mutant becomes similar to that of Kcv_{NTS} (Fig. 2.14). The gate is controlled by the amino acid immediately upstream of Phe^{78}. Kcv_{NTS} has a Gly at position 77 while Kcv_S contains a Ser. When these two amino acids are cross-swapped, Kcv_{NTS} G77S shows longer closing times, whereas Kcv_S S77G does not show them anymore (Fig. 2.14). The results of these mutation studies postulated the hypothesis that the additional gate in Kcv_S is formed by an intrahelical hydrogen bond between the hydroxyl residue of Ser^{77} and the amid oxygen of Ile^{73} (Rauh et al., 2017). In further mutation studies, it could be shown that only amino acids with a hydroxyl residue are indeed able to close the inner gate (Rauh et al., 2017). Since Kcv_{NTS} possesses a Gly at this position the Phe gate cannot close, and the channel does not show long closing times in its phenotype. Furthermore, experimental and computational data have shown, that this Ser forms a kink in TM2 with the effect that the orientation of the helix downstream of Ser77 is altered, including Phe^{78} (Rauh et al., 2017). In summary the available data suggest that the different properties of the two channels are due entirely to the different amino acids at position 77.

Inspired by this information, we will investigate in the following whether the different sensitivities of Kcv_{NTS} and Kcv_S to QAs are due to the structural differences related to the inner gate. An alternative explanation could be that there are further structural differences in the area of the inner pore entrance or the cavity, which account for the different sensitivities. Two strategies will be used: 1.) to entirely remove the inner gate in Kcv_S (F78A) and 2.) to eliminate only the hinge in Kcv_S (S77G), so that this region matches Kcv_{NTS}. First, the properties of TPrA and TPeA on Kcv_S F78A, e.g. the mutant with the inner gate totally removed, were investigated. These candidates present the basic two types of blocker. Since TPrA is a fast blocker, which exhibits clear differences between the channels, whereas the slow blocker TPeA causes only minor differences, these two QAs serve as examples for the two phenotypes of blocking of the mutant.

For both blockers, the basic behavior of the block in the mutant is similar to those in Kcv_{NTS} and Kcv_S. It is voltage dependent with a stronger block at positive voltages. Also, like in the wt-channels, TPrA causes a fast block, resulting in a reduction of the apparent single-channel

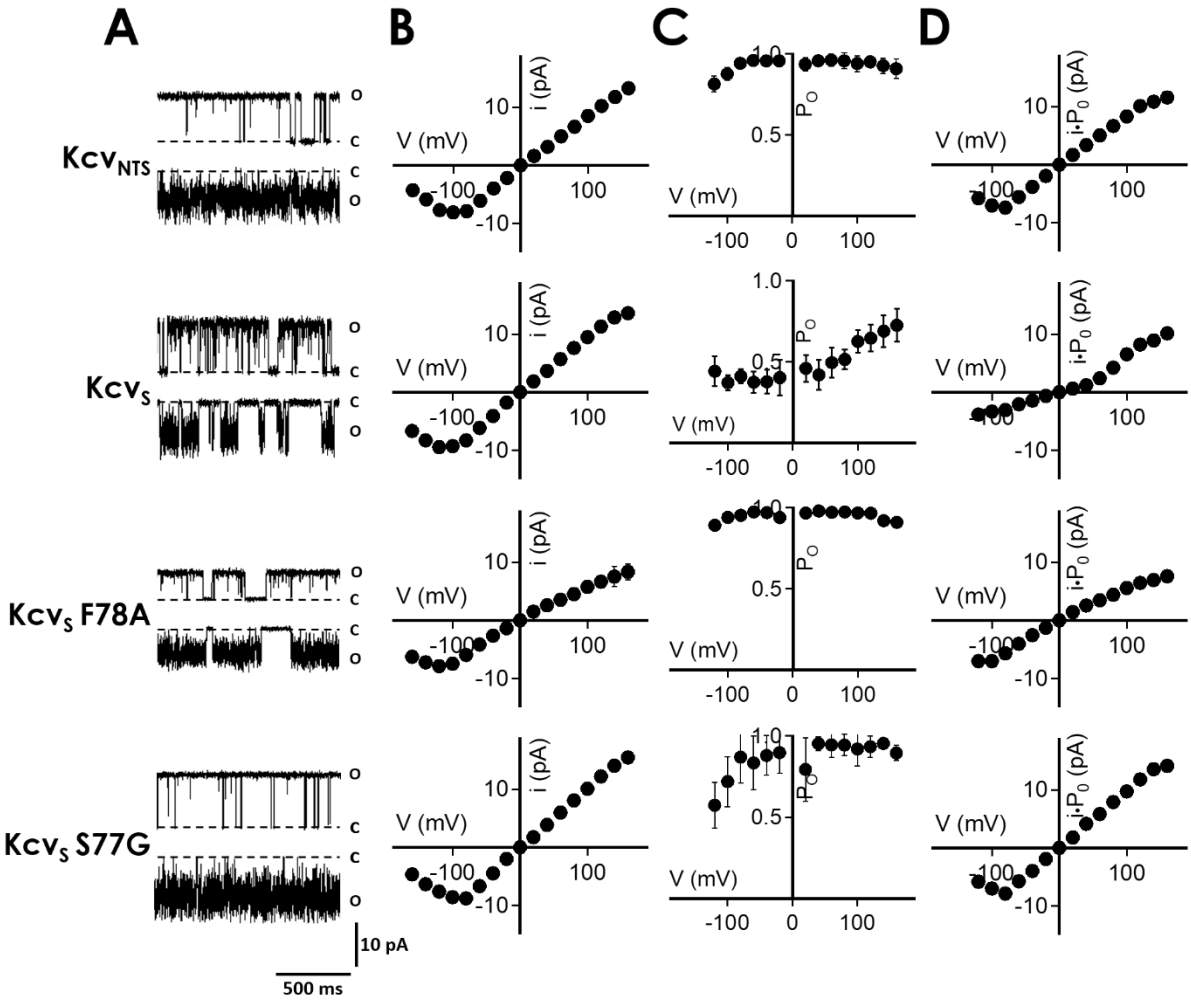

Figure 2.14: Functional properties of Kcv$_S$ F78A and Kcv$_S$ S77G compared to the wt-channels. (A) Single channel fluctuations in planar lipid bilayer. The closed **C** and open **O** levels are indicated along the current traces. The membrane voltage for the upper traces is 120 mV and -120 mV for the lower traces. (B) i/V-relations and corresponding (C) mean open probabilities and (D) time-averaged I/V relations. The latter were obtained by multiplying data in B and C. Mean data ± s.d. are from 3 independent recordings. Both mutations lead to an increase in the open probabilities approaching that of Kcv$_{NTS}$.

current, and TPeA causes a slow block resulting in a reduction of the open probability. Fig. 2.15E&F show dose-response curves of the two blockers at 100 mV and -60 mV. Compared to both wt-channels, it becomes apparent that the mutant exhibits a lower sensitivity to the blockers. While the K_D of TPrA at 100 mV is 0.22 ± 0.06 mM for Kcv$_{NTS}$ and 0.09 ± 0.03 mM for Kcv$_S$, the K_D of the mutant channel Kcv$_S$ F78A is approximately 4-fold higher with 0.56 ± 0.08 mM. A similar picture appears after the addition of TPeA. Here, the difference is even greater with a 14-fold increase in the K_D from 0.15 ± 0.04 µM for Kcv$_S$ to 3 ± 0.5 µM for Kcv$_S$ F78A.

Also, for the mutant Kcv$_S$ S77G the block properties of TEA, TPrA, and TPeA were examined. The data in Fig. 2.16 show, that the two fast blockers TEA and TPrA cause a reduction of the apparent single channel conductivity as described in the previous sections. Furthermore, TEA

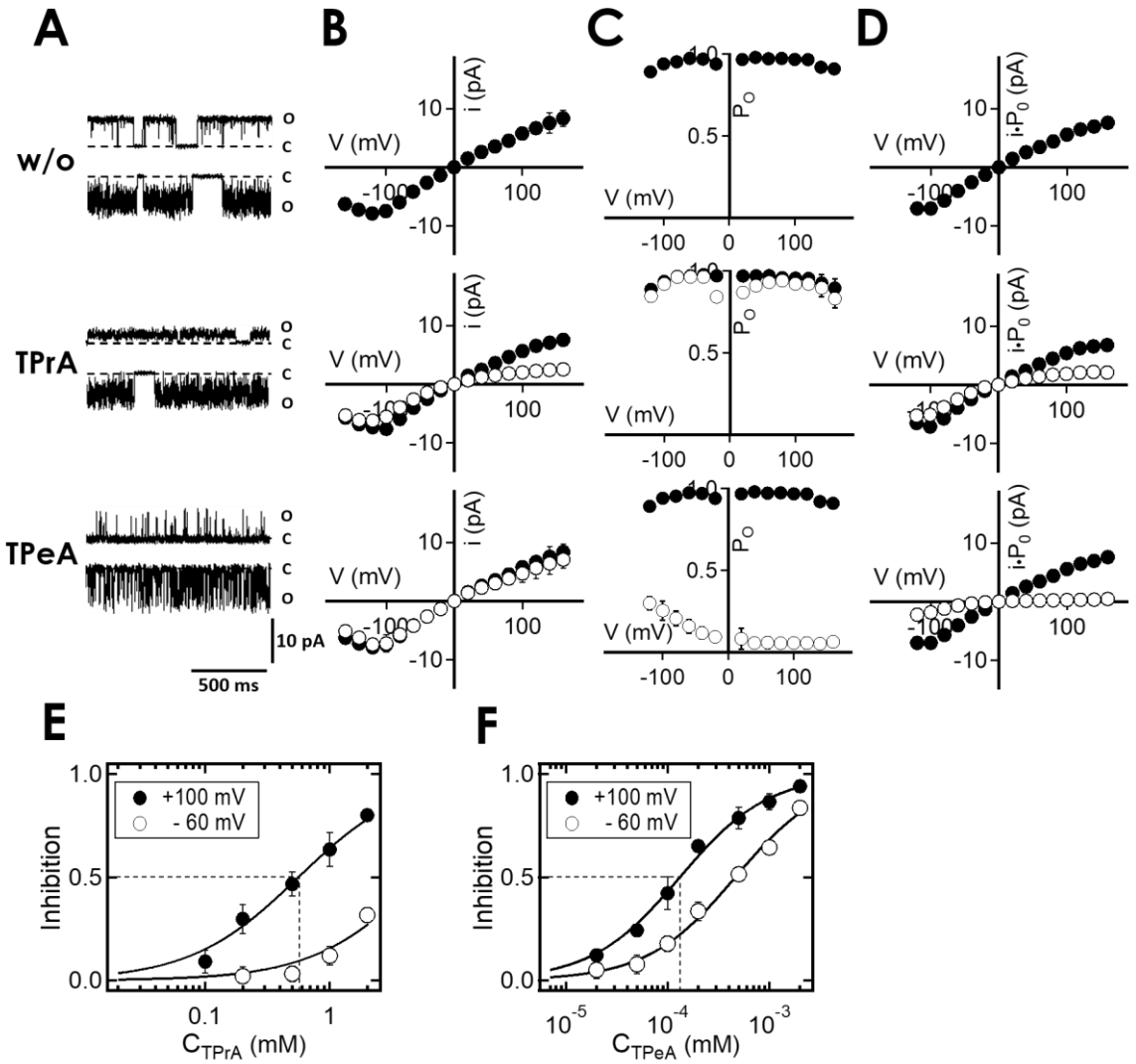

Figure 2.15: Sensitivity of Kcv$_S$ F78A to intracellular QAs. (A) Single channel fluctuations of Kcv$_S$ F78A in planar lipid bilayer w/o and with different QAs. The closed **C** and open **O** levels are indicated along the current traces. The membrane voltage for the upper traces is 120 mV and -120 mV for the lower traces. All QAs were applied from the intracellular site of the protein. The blocker concentrations are: 1 mM TPrA and 50 µM TPeA. (B) i/V-relations and corresponding (C) mean open probabilities and (D) time-averaged I/V relations. The latter were obtained by multiplying data in B and C. Data w/o QAs (black) and with QAs (white). Dose-response-curves of Kcv$_S$ F78A with (E) TPrA and (F) TPeA. The solid lines are average curves and represent the fit to the Hill equation. Mean data ± s.d. are from 3 independent recordings. The dotted line simplifies the readout of the K_D value at 100 mV.

also slightly reduces the open probabilities by another slower block effect, in the same way as for the wildtypes. TPeA, on the other hand, reduces the open probability in a way that the individual events are slow enough to be resolved. In order to quantify the effects of the mutations, the K_D values were calculated from dose-response curves (Fig. 2.17). Only the values at the positive voltage range were compared, since the previous sections have shown that negative voltages lead to strong variations due to the very

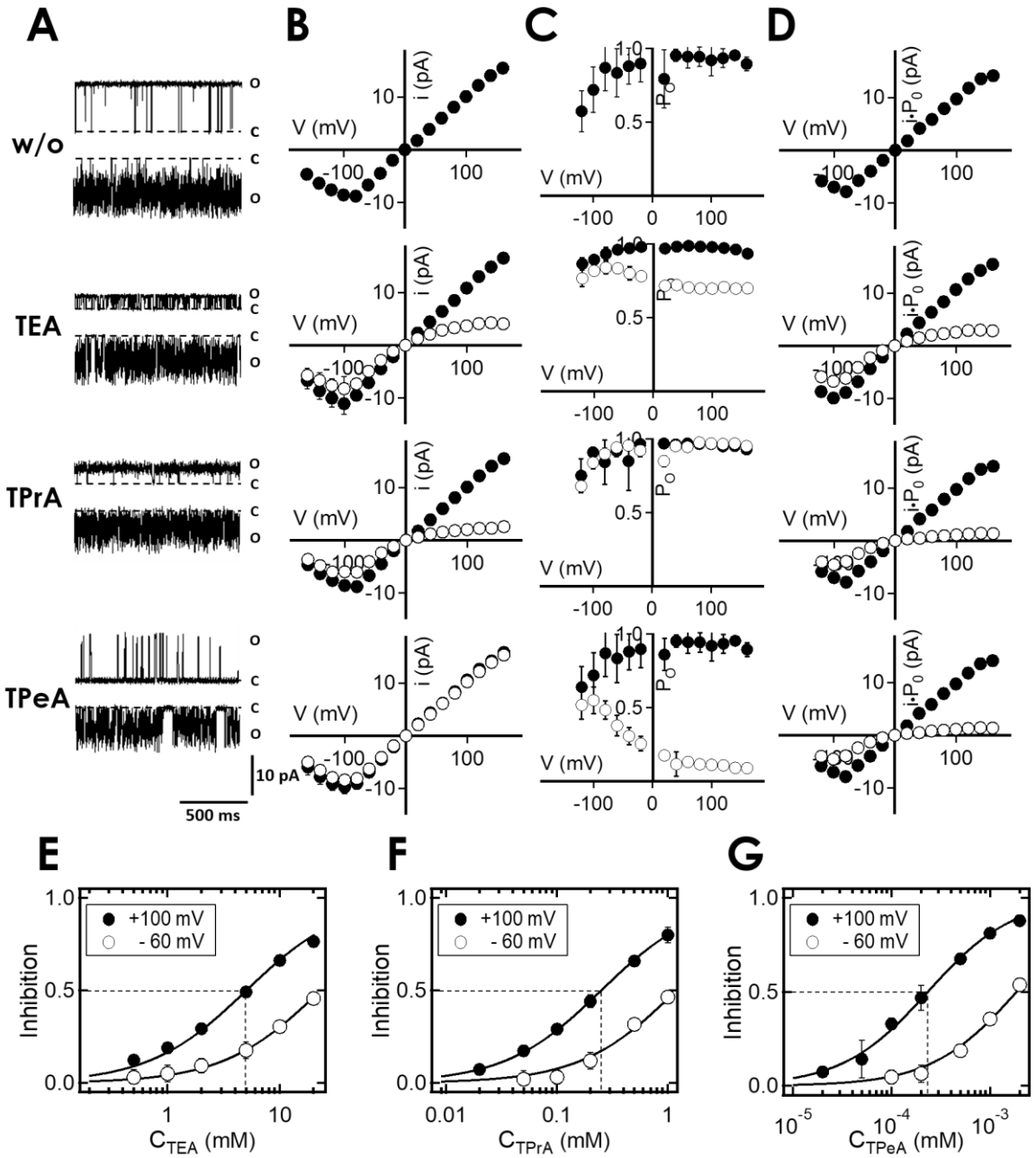

Figure 2.16: Sensitivity of Kcv_S S77G to intracellular QAs. (A) Single channel fluctuations of Kcv_S S77G in planar lipid bilayer w/o and with different QAs. The closed **C** and open **O** levels are indicated along the current traces. The membrane voltage for the upper traces is 120 mV and -120 mV for the lower traces. All QAs were applied from the intracellular site of the protein. The blocker concentrations are: 10 mM TEA, 1 mM TPrA, and 2 µM TPeA. (B) i/V-relations and corresponding (C) mean open probabilities and (D) time-averaged I/V relations. The latter were obtained by multiplying data in B and C. Data w/o QAs (black) and with QAs (white). Dose-response-curves with (E) TEA, (F) TPrA, and (G) TPeA. The solid lines are average curves and represent the fit to the Hill equation. Mean data ± s.d. are from 3 independent recordings. The dotted line simplifies the readout of the K_D value at 100 mV.

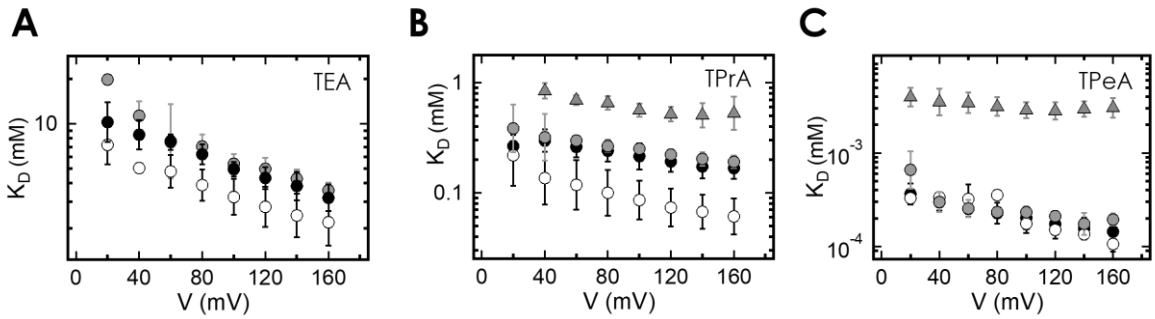

Figure 2.17: Sensitivities of Kcv_S F78A and Kcv_S S77G compared to the wt-channels. The apparent dissociation constant, K_D, derived from fits of dose-response curves with the Hill function from data as in Fig. 2.15 & 2.16. Shown is a complete dataset at voltages from 20 mV to 160 mV. Recordings with (A) TEA, (B) TPrA, and (C) TPeA with the following K^+ channels: Kcv_S (white), Kcv_{NTS} (black), Kcv_S F78A (grey triangles), and Kcv_S S77G (grey circles). Mean data ± s.d. are from 3 independent recordings. While Kcv_S S77G acquires the identical sensitivity as Kcv_{NTS}, Kcv_S F78A is less sensitive.

low block efficiency at these voltages. In the following, these values will be compared from recordings at 100 mV.

A priori, it would have been expected that the removal of the inner gate leads to an increased size of the pore entrance, which in turn should result in an increased accessibility and thus in a higher sensitivity to QAs. An approach to the solution of this conundrum will be based on the inspection of the rate constants k_{BO} and k_{on} (or k_{OB}) (Fig. 2.20) below, which determine the K_D with opposite effects.

When comparing the K_D values in the positive voltage range, the difference in sensitivity becomes even more apparent (Fig. 2.17B&C). The K_D values for the two blockers reach in the mutant channel an asymptotic value at positive voltages. As described in the previous sections, with TPrA Kcv_{NTS} exhibits at 100 mV a K_D of 0.22 ± 0.06 mM, while the K_D of Kcv_S is 0.09 ± 0.03 mM. After the substitution of Ser to Gly at position 77, the K_D of Kcv_S S77G is with 0.25 ± 0.02 mM not significantly different from that of Kcv_{NTS} (Fig. 2.17B). The S77G mutation seems to transform the properties of the intracellular block by QAs in the Kcv_S channel into that of Kcv_{NTS}. The results of these experiments imply that the intrahelical hydrogen bond formed by Ser^{77} has a direct influence on the sensitivity of the channel to QAs. The calculation of the rate constants k_{BO} and k_{on} (or k_{OB}), which determine the K_D with opposite effects will clarify the reason for the decrease of the sensitivity.

Dwell-time analysis has been used to calculate the rate constants for TPeA dissociation and the association as described above for the wildtype channels. Fig. 2.18 shows exemplary dwell-time histograms of Kcv_S F78A and Fig. 2.19 of Kcv_S S77G before and after the addition of different TPeA concentrations. If one compares the different histograms with those of the wt-channels, the effect of the block is similar. As the blocker concentration rises, the closed-time histograms show an increase of the population of C_2, indicating that the blocked state B has a

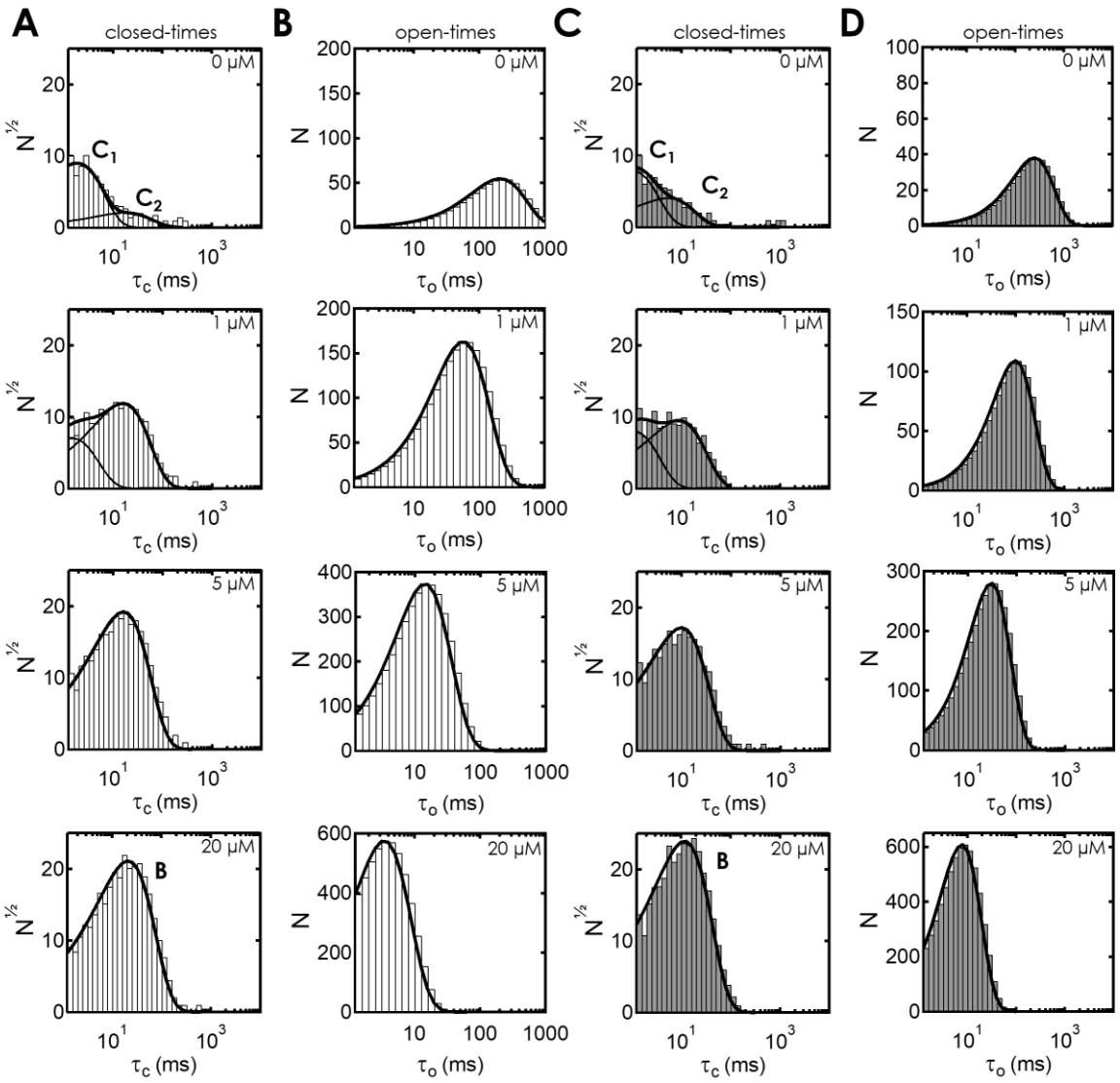

Figure 2.18: Dwell-time analysis of Kcv$_S$ F78A blocked by TPeA. Exemplary closed-time (A) and open-time histograms (B) at 100 mV (white). Exemplary closed-time (C) and open-time histograms (D) at -60 mV (grey). The first row shows data without blocker, the second with 1 µM, the third with 5 µM and the fourth with 20 µM TPeA. The data in A&C are fitted with the sum of two exponential functions while the data in B&D only require a single exponential function. The two closed states are indicated by C1 and C2, the blocked state is indicated by B.

similar dwell-time as the intrinsic closed state S_2 (Fig. 2.8). With regard to the open-time histograms, the lifetime of the events decreases, whereas the number of events is significantly higher. The analysis of the k_{on} values underscores that they are irrelevant for the differences between the channels. The k_{OB} rate is identical for the two wt-channels (Fig. 2.20D) at least at positive voltages. Accordingly, the intrahelical hydrogen bridge in Kcv$_S$ has no influence on the diameter of the pore entrance.

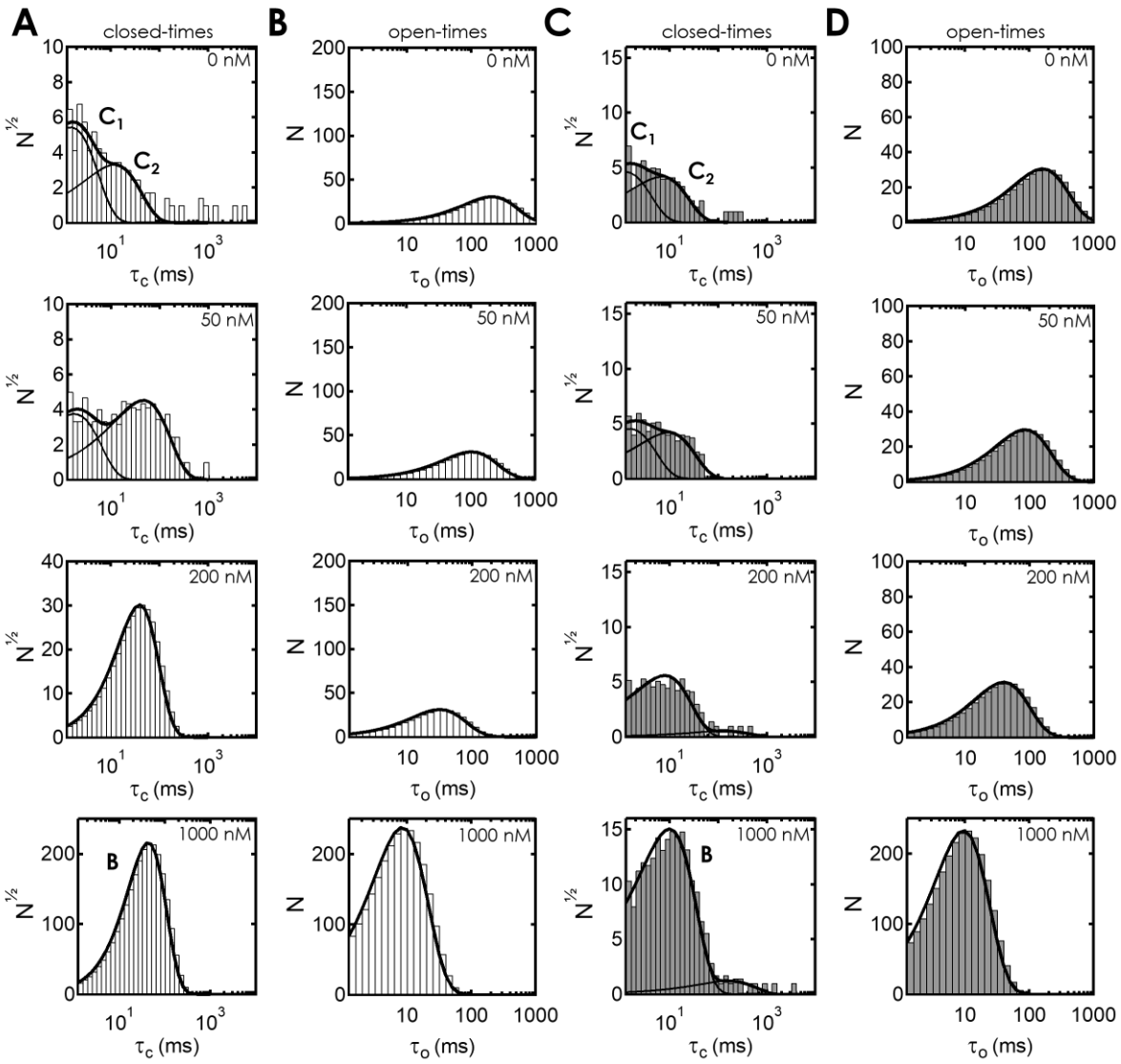

Figure 2.19: Dwell-time analysis of Kcv$_S$ S77G in absence and presence of TPeA. Exemplary closed-time (A) and open-time histograms (B) at 100 mV (white). Exemplary closed-time (C) and open-time histograms (D) at -60 mV (grey). The first row shows data without blocker, the second with 50 nM, the third with 200 nM, and the fourth with 1000 nM TPeA. The data in A&C are fitted with with the sum of two exponential functions while the data in B&D only require a single exponential function. The two closed states are indicated by C1 and C2, the blocked state is indicated by B.

The effect of the mutation S77G in Kcv$_S$ (Fig. 2.20) seems to be obvious. The rate constants k_{on} and k_{BO} obtain the same value as those of Kcv$_{NTS}$. This is expected as this mutation eliminates the hydrogen bond between Ser^{77} and the backbone of Ile^{73} (Rauh et al., 2017), creating the same structure as in Kcv$_{NTS}$.

The fast blocker TPrA causes a parallel shift of $k_{on} = k_{BO}$/[TPrA] and $k_{off} = k_{BO}$ on a logarithmic scale. This corresponds to a factor of about 4 for $k_{BO} = k_{off}$ and of about 2 for $k_{OB} = k_{on}$ [TPrA). This

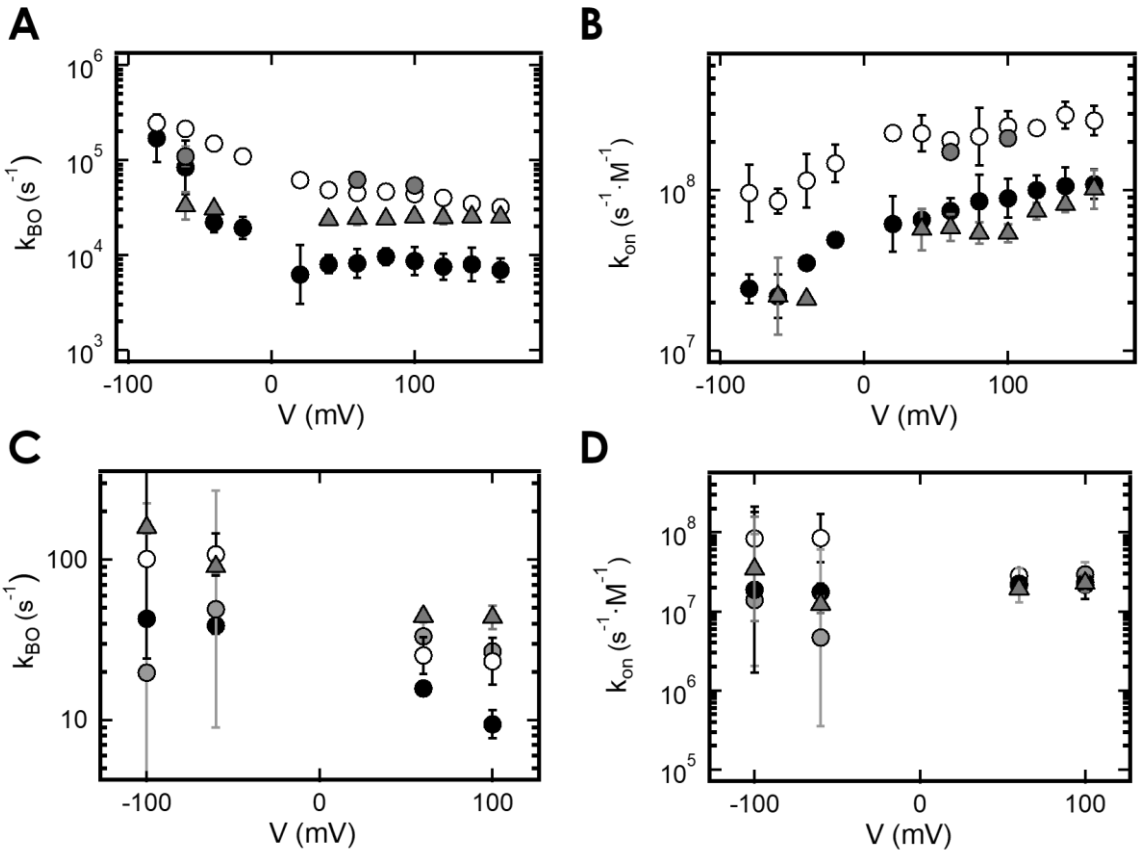

Figure 2.20: Kinetics of block of Kcv_S F78A and Kcv_S S77G compared to the wt-channels. (A) Dissociation rate (k_{BO}) and (B) Association rate (k_{on}) of block with 0.1 mM TPrA determined from fits of beta distribution analysis. (C) Dissociation rate and (D) Association rate of block with different TPeA concentrations. Data determined from fits of dwell-time histograms. Kcv_S (black), Kcv_{NTS} (white), Kcv_S F78A (grey triangles), and Kcv_S S77G (grey circles). The following TPeA concentrations are shown: 2 µM for Kcv_{NTS}, 1 µM for Kcv_S, 20 µM for Kcv_S F78A, and 2 µM for Kcv_S S77G. Mean data ± s.d. are from 3 independent recordings.

numerical finding explains why the faster blocking in Kcv_{NTS} results in a smaller blocking effect (and in a higher K_D, Fig. 2.17B) since the probability P_B of being in the closed state is:

$$p(O) = \frac{k_{OB}}{k_{BO} + k_{OB}} \qquad \textbf{(2.2)}$$

In the mutant Kcv_S S77G, the rate constants of blocking and unblocking coincide with those of Kcv_{NTS}. This is remarkable, because S77G also converts the O-M gating (Fig. 2.7A&B) of Kcv_S into that of Kcv_{NTS} (Schroeder, 2015). S77G eliminates the hydrogen bond in Kcv_S between Ser^{77} and the backbone of Ile^{73}. This hydrogen bond controls the recently detected inner gate related to the movements of the phenyl rings of Phe^{78} (Rauh et al., 2017).

With this mechanism in mind, the effect in the mutant Kcv_S F78A is surprising. It would be expected that removing the inner gate would convert the blocking behavior of Kcv_S to that of

Kcv_{NTS}, as done by S77G. However, the data in in Fig. 2.20 give a different picture. There is no effect on blocker binding $k_{OB} = k_{on}$ [TPrA] at all voltages. In the case of blocker dissociation $k_{off} = k_{BO}$, there is no effect at negative voltage, but k_{OB} approaches the values of Kcv_{NTS} with increasing positive voltages.

Actually, it does not come as a surprise that F78A has no effect on blocker binding. Measurements of the blocking kinetics can be done only in the long sojourns, when the inner gate is open. Then, the phenyl rings are out of the way. This also holds for blocker dissociation at negative voltages. Consequently, it is not a steric hindrance of blocker diffusion. The reason has to be in a conformational change near the blocker binding site and also for the binding site itself. So far it is known, that S77G influences a kink at position 77, which also may be influenced by F78A. However, details about any structural changes near the binding site of the blocker remain to be investigated.

In the light of such a hypothesis, the results obtained with TPeA may be unexpected, namely that blocker association (k_{OB} or k_{on}) is not different in both channels and in the mutants, in contrast to the effects of TPrA (Fig. 2.20). A possible explanation is as follows. The mutations S77G and F78A change the energy landscape near the blocker binding site. TPrA is small and thus its binding to the wall of the cavity near the binding site depends on how well TPrA fits to narrow changes in this energy landscape. This weak binding would influence the distance to the maximum of the Eyring barrier determining the rate constant of binding. Such a long-range effect of the mutations of the inner gate are likely because S77G also influences the O-M gating, which has been assigned to the selectivity filter (Rauh et al., 2017 & 2018). TPeA however is bigger than TPrA. Thus, it may not feel the fine-scale changes in the energy landscape related to the two different channels and its mutations. However, all the above hypotheses are not more than just incitements for future physiological, computational and structural investigations.

Significance for the structure of the inner gate and the dimensions of the pore

What do the results of these experiments tell us about the probable structure of the inner pore of viral K^+ channels? The working hypothesis was that probing the channel with varying sizes of blocker molecules should provide a molecular ruler to measure the size of the pore in an analogous manner to what was achieved for Na^+ channels (Hille, 1971).

The on rates are interpreted as function of the blocker size and are used for determining the diameter of the channel pore (Guo & Lu, 2001). It is assumed that small QAs are able to enter the channel and therefore have a high k_{OB}. In contrast, large molecules should be hindered in their diffusion by steric obstacles. This leads to a reduction of k_{OB}. Between these two extremes an intermediate window is present in which the k_{OB} value drops with the

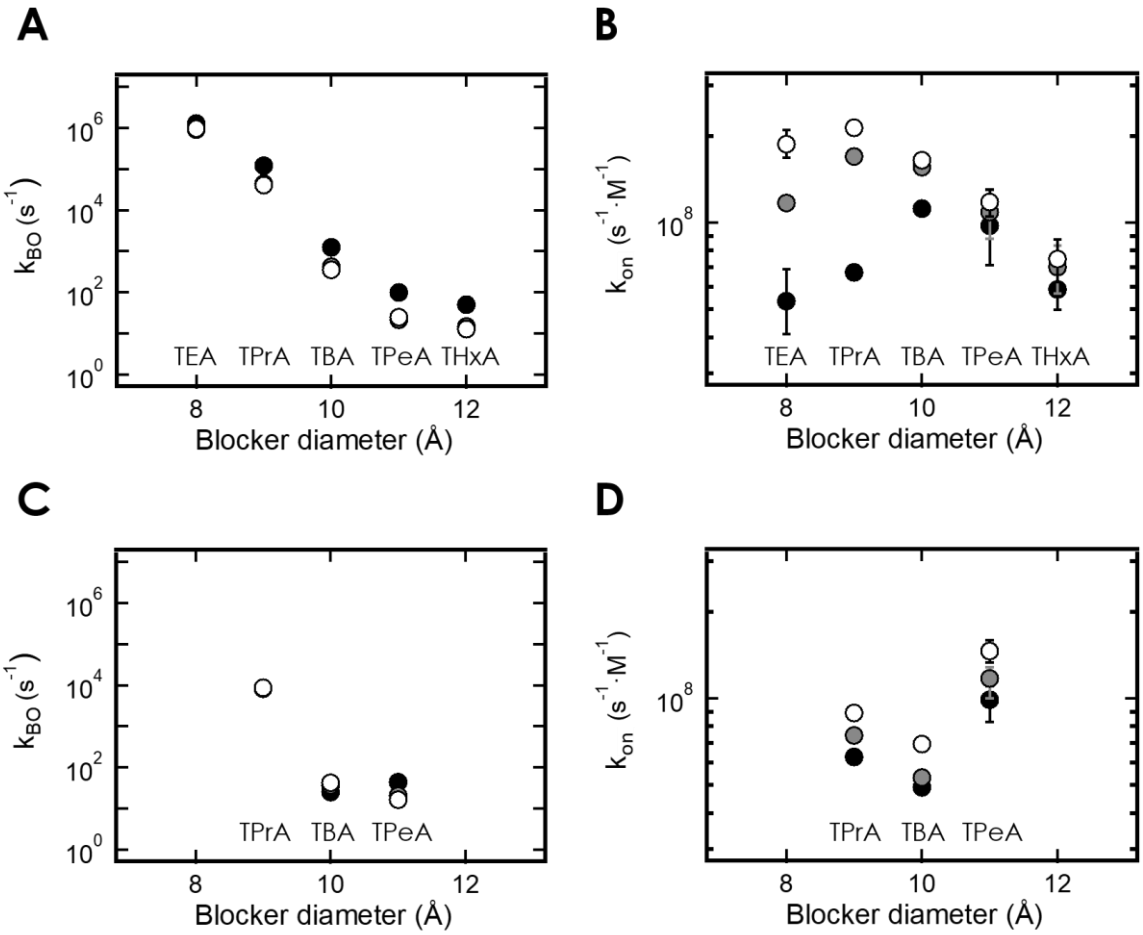

Figure 2.21: Dependence of the dissociation and association rates of QA blockers on their size in Kcv_{NTS} and Kcv_S. The blocker dissociation for Kcv_{NTS} (A) and Kcv_S (C) and association rates for Kcv_{NTS} (B)and Kcv_S (D) are plotted as a function of their ionic radii. The shown voltages are -60 mv (black), 60 mv (grey), and 100 mV (white). Mean data ± s.d. are from 3 independent recordings, except for TBA.

size of the blocker. It is assumed that the size between the sizes of two QAs, which exhibit the largest difference in the k_{OB} value, should correspond to the pore size (Jara-Osegura et al., 2008).

Compared to the dissociation, the association rate constants in this analysis show no relative difference with increasing blocker size (Fig. 2.21). At 100 mV the association rate constants measured in Kcv_{NTS} for TPrA is only three times faster than for THxA. In contrast, there is a 3000-fold difference in dissociation rate constant between these two QAs. The reason could be the flexibility of the block molecules (Faraldo-Gómez et al., 2007), or the flexibility of the intracellular pore entry. The results of this analysis underscore that k_{OB} is independent of the blocker size, a phenomenon which is unusual (Faraldo-Gómez et al., 2007; Piechotta et al., 2011).

With rising QA diameter, the k_{BO} values decrease exponentially over several orders of magnitudes. Accordingly, larger and thus more hydrophobic molecules bind stronger to the binding site. In addition, the off rates reflect the voltage dependence of the block. When the results from the on and off rates are taken together it becomes apparent that the K_D values for the blocker molecules are slightly more influenced by the variance in the off rates, than by the relative similar on rates. The lower values for TEA could be an artifact of the extended beta distribution analysis. This method reaches its analytical limit at these high rate constants. Likewise, the k_{BO} values for TEA in relation to the trend between TPrA and TPeA also fits this hypothesis. Of course, the anomaly of the TEA block could also play a role here, since this fast blocker also leads to a slow and therefore resolvable block.

Between TPeA and THxA a saturation of the rate constants can be seen. According to Piechotta et al. (2011), the saturation for THxA could occur from a collision of the blocker with the channel wall. Thus, the cavity below the selectivity filter could be 11 Å in diameter. With regard to the diameter of the pore entrance, as already described, a significant decrease of k_{OB} is required. The two channels IRK1 and ROMK1 show a 30-fold reduction in k_{OB} between TPrA and TPeA. Consequently, Guo & Lu (2011) proposed a diameter for the inner pore entrance of 9 Å for both Kir channels. Due to the small differences in the constants shown here, the determination of the size of the pore entrance for the viral K^+ channels is not as trivial.

The diffusion limit of QAs is between 10^8 and 10^9 $s^{-1} \cdot M^{-1}$ (Guo & Lu, 2001). However, the blocker rates in their studies were clearly below these values. This is also the case for the non-selective cation channel TRPV1 (Jara-Oseguera et al., 2008). In both studies the pore diameter of the two channels were determined as 9-10 Å respectively. The rates for Kcv_{NTS} are only slightly below the diffusion level. This means that even THxA can diffuse almost unhindered into the pore of this channel. TBA can enter the BK channel with a k of $5x10^8$ $M^{-1} \cdot s^{-1}$ (Li & Aldrich, 2004). This channel is known for its high conductivity and the authors assume that the high association rate is correlated with a large pore, which in turn is responsible for the high conductivity. Viral K^+ channels could be optimized for high conductivity and small size at the same time. The small size could be the reason for the high rate constants, because the molecule would not have to diffuse through a large pore to reach the binding site. But with these results the exact diameter of the pore entrance cannot be determined with QAs.

Regarding the comparison of QA induced block properties between Kcv_{NTS} and Kcv_S, the differences can be explained as follows. It could be shown in this context that the differences in affinity between the two similar channels with respect to k_{OB} and k_{BO} can be traced back exclusively to the inner gate, which is causally linked to Ser^{77} in Kcv_S. Notably the rate constants of Kcv_S S77G are identical to Kcv_{NTS}. The influence of the kink of Ser^{77} might continue up to the selectivity filter. This leads to a different binding speed of the small molecule TPrA, which is

reflected in varying k_{OB} values. In contrast, TPeA tends to be too large to sense the small differences and the k_{OB} values of the wt-channels are equal.

The also reduced k_{BO} in Kcv_S with TPrA could be caused by a trapping of the blocker. For other channels the trapping within the cavity by a closing gate has already been investigated. In *Shaker* a point mutation in S6 leads to a trapping of TEA (Holmgren et al., 1997). The authors suggested that in these channels the gate may function as a trap door or hinged lid that occludes access from the intracellular solution to the blocker site and to the narrow ion-selective pore. Furthermore, QA ions can also be trapped in the cavity of KcsA due to the bundle crossing of TM2 (Zhou et al., 2001). However, these gates do not resemble the inner gate of Kcv_S. While the inactivation of these channels leads to a trapping effect, this does not occur in Kcv_S. In the latter case the QAs can be trapped without simultaneous inhibition of the ion current. More similar to the situation in Kcv_S is the mechanism of voltage-gated Na^+ channels. The aromatic ring at residue Phe^{227} is in these channels specifically important for holding TBA in its binding site (Shimomura et al., 2016). The removal leads to an increase in the k_{BO} rates while the k_{OB} is unchanged. An equivalent effect could also be observed in the Kcv_S F78A mutant and should also be seen in Kcv_{NTS} F78A. But, since both wt-channels have the bulky aromatic side chain of Phe^{78}, both channels should be able to trap the QAs in the cavity. This would also explain the significantly higher affinity of the two Kcv channels compared to KcsA (Kutluay et al., 2005). It seems, that Kcv_S is able to trap the smaller QAs better than Kcv_{NTS} due to the intrahelical hydrogen bond of Ser^{77}. The larger the diameter of the QAs, the smaller the difference between the two channels, since the effect of the inner gate on the trapping becomes similar.

2.4 Conclusion

In this study the effects of different quaternary ammonium cations on viral K^+ channels were investigated using the lipid bilayer technique. This study was motivated by different electrophysiological properties of the channels Kcv_{NTS} and Kcv_S, which arise from the presence of an inner gate in Kcv_S (Rauh et al., 2017). In the first set of experiments it could be shown that in planar lipid bilayer the cytosolic part of the channel is exclusively oriented to the *cis* chamber. This together with data from patch clamp recordings of these channels in cells allow a clear-cut assignment of the orientation of the channel with respect to accessibility of cytosolic and extracellular blockers. In this well-defined experimental system, the voltage dependence and the velocity of a block by QAs was investigated. The data show that the efficiency of the intracellular block by QAs is significantly higher at positive voltages than at negative voltages. In addition, the speed of the block decreases with rising diameter of the blocking molecules. While TEA and TPrA lead to an apparent reduction of the single channel amplitude, the individual block events from TBA, TPeA, and THxA can be distinguished from each other; in the latter case a reduction of the open probabilities occurs as a result of the blockers. A direct comparison in the sensitivity of the two K^+ channels towards the QA blockers shows that Kcv_S is more sensitive to the different QAs. The reason for this is a difference in blocker dissociation and association. This difference decreases with increasing molecule diameter. In order to find out whether the inner gate, which is present in Kcv_S and absent in Kcv_{NTS} channel is responsible for this difference, this gate was removed in the mutant Kcv_S F78A. This manipulation leads to a reduction in sensitivity of the mutant to TPrA and TPeA of up to 14-fold. The reason for the reduced affinity can be traced back to a change in dissociation of the blocker. There is no effect on blocker binding. The further mutation S77G in Kcv_S also eliminates the inner gate in that it prevents an intrahelical hydrogen bonding in the inner transmembrane domain of the channel. In this way Phe^{78} is no longer obstructing the ionic pathway with the effect that the mutant acquires the electrophysiological properties of Kcv_{NTS}. A direct comparison of the rate constants of this mutant with those of the two wt-channels shows that the mutant behaves like the Kcv_{NTS} channel. To conclude, the goal of determining the spatial structure of the intracellular pore entrance could not be achieved, because of the almost identical blocker binding. Nevertheless, the results provide new insights into future physiological computational and structural investigations.

2.5 Methods

In vitro protein expression and purification

The two viruses coding for Kcv_{NTS} and Kcv_S were originally isolated in two alkaline lakes in Nebraska (Greiner, 2011). For cell-free expression, the coding sequences of the two channels were cloned into the pEXP5-CT/TOPO vector. The TA Expression Kit (Invitrogen, Carlsbad, CA, USA) was used. In order to express the channel proteins in their natural form, a stop codon was inserted downstream of the coding sequence. *In vitro* expression of the channel proteins was performed as described previously (Winterstein et al., 2018) with the MembraneMax HN Protein Expression Kit (Invitrogen, Carlsbad, CA, USA). The expression took place in the presence of nanolipoproteins (NLPs), which have several His-tags. This allows subsequent purification by metal chelate affinity chromatography. In detail, the reaction mixture is loaded onto a 0.2 mL HisPur Ni-NTA spin column (ThermoFisher Scientific, Waltham, MA, USA). All steps were performed according to the manufacturer's instructions. Only during elution, the spin column was washed three times with 250 mM pure imidazole.

Planar lipid bilayer experiments

All lipid bilayer experiments were performed at room temperature (20-25 °C) on a vertical bilayer set-up (IonoVation, Osnabrück, Germany). The preparation of the recording chamber was done as described by Braun et al. (2013). The two chambers were connected with Ag/AgCl electrodes to the head-stage. A patch-clamp amplifier (L/M-EPC-7, List-Medical, Darmstadt, Germany) was used to amplify the signal. The current responses were filtered with a 4-pole Bessel filter at 1 kHz and digitized with a sampling frequency of 5 kHz with an A/D converter (LIH 1600, HEKA Elektronik, Lambrecht, Germany). The bilayers of 1.2-diphytanoyl-sn-glycero-3-phosphocholine (DPhPC, Avanti Polar Lipids, Alabaster, AL, USA) were formed using the pseudo painting/air bubble technique (Braun et al., 2014b). The electrolyte solution consisted of 100 mM KCl. A small amount of the purified protein solution diluted in 250 mM imidazole was added to the *trans* compartment directly below the bilayer, by using a curved Hamilton syringe. After the successful incorporation of a single channel into the DPhPC membrane, constant voltages were applied for one to five minutes. In steps of 20 mV the voltage was changed between +160 mV and -160 mV.

Data analysis

The single channel measurements were recorded with Patchmaster (HEKA Elektronik, Lambrecht, Germany) and evaluated with the custom-made program KielpatchDA. Multi-channel measurements were analyzed with Fitmaster (HEKA). The amplitudes of the single channel measurements were evaluated visually. An automated Hinkley jump detector (Schultze & Draber 1993) was used to determine the open probabilities. The dwell-time histograms were fitted with one to three exponential functions with a custom-made Matlab script (provided by O. Rauh). Blocker dose-response relations were obtained from current measurements using voltage steps from +160 mV to -160 mV in 20 mV increments for 120 s. Data were obtained by measuring activity of the same channel first in the absence and then in the presence of varying concentrations of blocker. The fraction of current blocked (F_B) was calculated as:

$$F_B = 1 - \frac{i}{i_0} \tag{2.3}$$

where i is the current in the presence of blocker and i_0 is the current in the absence of blocker for TEA and TPrA. For TBA, TPeA and THxA, the open probability P_O was used instead of the current . For each QA, the apparent dissociation constant, K_D, was obtained at a given voltage by fitting F_B as a function of blocker concentration with the Hill equation:

$$F_B = \frac{[QA]^s}{K^s{}_D + [QA]^s} \tag{2.4}$$

where s is the steepness factor and [QA] is the quaternary ammonium concentration. S was set to 1 for all fits, and all data could be appropriately described in this way.

Dwell-time analysis

The number of missed closed events of the dwell-time histograms due to the limited temporal resolution of the recording set-up were estimated by the fit parameters. They were then used to correct the mean lifetime of the open state. It was assumed that the missed events are evenly distributed and that they have no influence on the total open-time of the channel. The occupation probabilities were calculated by assuming a simple Markov model in which all closed states are directly connected to the open state. The generated open-time and

closed-time histogram were fittes with Eq. 2.5 in order to obtain the relative contribution a_j and the mean lifetime τ_j of the various populations of dwell-times.

$$N_i = N \cdot \left(\sum_{j=1}^{n} a_j \cdot e^{-\frac{t_i}{\tau_j}} \left(e^{\frac{\Delta t_i}{t_j}} - 1 \right) \right) \quad \textbf{(2.5)}$$

The fit delivers the dwell-times and occupation probabilities of the state in the Markov model in Fig. 2.7, as well as the rate constants connecting the Markov states.

Extended beta distribution analysis

This analysis was carried out by Ulf-Peter Hansen and Indra Schroeder. The analysis becomes necessary when the rate constants of gating or blocking are higher than the bandwidth of the low-pass filter. In that case neither individual gating transitions nor the open channel current can be directly observed. Instead the gating or blocking transitions result in "excess noise" (Heinemann & Sigworth, 1991; Schroeder, 2015). This excess noise leads to broadenend and non-Gaussian peaks in amplitude histogram. With the help of extended beta distribution analysis, the hidden gating parameters can be extracted from these amplitude histograms (Rießner, 1998; Schroeder, 2015; Rauh, et al., 2017 & 2018). A custom-made analysis program "bownhill" generates theoretical amplitude histograms on the basis of an adequate Markov model (e.g. in Fig. 2.6A) and includes the identical base line noise and a digital representation of the jump-response of the 4-pole Bessel filter. A fitting routine adjusts the rate constants of the Markov model until the theoretical and the measured amplitude histogram coincide. Details of the application of this analysis to gating in Kcv_{NTS} have been described previously (Schroder, 2015; Rauh, et al., 2017 & 2018). The program can be downloaded: http://www.bio.tu-darmstadt.de/ag/professuren/indraschroeder/software.en.js.

2.6 References

Armstrong C. M., and B. Hille (1972) The Inner Quaternary Ammonium Ion Receptor in Potassium Channels of the Node of Ranvier. *J. Gen. Physiol.*, *59*, 388–400.

Biasini M., S. Bienert, A. Waterhouse, K. Arnold, G. Studer, T. Schmidt, F. Kiefer, T. G. Cassarino, M. Bertoni, L. Bordoli, and T. Schwede (2014) SWISS-MODEL : modelling protein tertiary and quaternary structure using evolutionary information. *Nucleic Acids Res.*, *42*(April), 252–258.

Braun, C., I. Schroeder, L. M. Henkes, C. Arrigoni, S. M. Kast, A. Moroni, and G. Thiel (2013) Minimal viral K+ channels as robust model systems for understanding structure/function correlations. *Eur Biophys J 42 (Suppl 1):S1–S236, doi: 10.1007/s00249-013-0917-x*

Braun, C., C. Lachnit, P. Becker, L. M. Henkes, C. Arrigoni, S. M. Kast, A. Moroni, G. Thiel, and I. Schroeder (2014a) Viral potassium channels as a robust model system for studies of membrane-protein interaction. *Biochim Biophys Acta 1838(4):1096-103*

Braun C. J., T. Baer, A. Moroni, and G. Thiel (2014) Pseudo painting/air bubble technique for planar lipid bilayers. *J. Neurosci. Methods*, *233*, 13–17.

Carpenter E. P., K. Beis, A. D. Cameron, and S. Iwata (2008) Overcoming the challenges of membrane protein crystallography. *Curr. Opin. Struct. Biol.*, *18*(5), 581–586.

Choi, K.L., C. Mossman, J. Aubé, and G. Yellen (1993) The internal quaternary ammonium receptor site of Shaker potassium channels. *Neuron 10 (3), 533–541. 10.1016/0896-6273(93)90340-W*.

Faraldo-Gómez J. D., E. Kutluay, V. Jogini, Y. Zhao, L. Heginbotham, and B. Roux (2007) Mechanism of Intracellular Block of the KcsA K+Channel by Tetrabutylammonium: Insights from X-ray Crystallography, Electrophysiology and Replica-exchange Molecular Dynamics Simulations. *J. Mol. Biol.*, *365*(3), 649–662.

French R. J., and J. J. Shoukimas (1981) Blockage of quid axon potassium conductance by internal tetra-N-alkylammonium ions of various sizes. *Biophys. J.*, *34*(May), 271–291.

Gabriel T. (2018) Measurement of the Kcv NTS inner gate diameter with quaternary ammonium. *Master Thesis Tech. Univ. Darmstadt.*

Gazzarrini S., M. Kang, A. Abenavoli, G. Romani, C. Olivari, D. Gaslini, G. Ferrara, J. L. van Etten, M. Kreim, M. S. Kast, G. Thiel, and A. Moroni (2009) Chlorella virus ATCV-1 encodes a functional potassium channel of 82 amino acids. *Biochem. J*, *420*(2), 295–303.

Guo D., and Z. Lu (2001) Kinetics of inward-rectifier K+ channel block by quaternary alkylammonium ions. dimension and properties of the inner pore. *J. Gen. Physiol.*, *117*(5), 395–406.

Heginbotham L., and E. Kutluay (2004) Revisiting Voltage-Dependent Relief of Block in Ion Channels : A Mechanism Independent of Punchthrough. *Biophys. J.*, *86*(6), 3663–3670.

Heinemann S. H., and F. J. Sigworth (1991) Open channel noise VI . Analysis of amplitude histograms to determine rapid kinetic parameters. *Biophys. J.*, *60*(September), 577–587.

Hille (2001) Ion channels of excitable membranes. *Sinauer Associates, Inc*.

Hille B., and W. Schwarz (1978) Potassium Channels as Multi-Ion Single-File Pores. *J. Gen. Physiol.*, *72*(October), 409–442.

Holmgren M., P. L. Smith, and G. Yellen (1997) Trapping of Organic Blockers by Closing of Voltage-dependent K ƨ Channels Evidence for a Trap Door Mechanism of Activation Gating. *J. Gen. Physiol.*, *109*(May), 527–535.

Jara-Oseguera A., I. Llorente, T. Rosenbaum, and L. D. Islas (2008) Properties of the Inner Pore Region of TRPV1 Channels Revealed by Block with Quaternary Ammoniums. *J. Gen. Physiol.*, *132*(5), 547–562.

Jiang Y., A. Lee, J. Chen, M. Cadene, B. T. Chait, and R. MacKinnon (2002) The open pore conformation of potassium channels. *Nature*, *417*(6888), 523–526.

Jogini V., and B. Roux (2005) Electrostatics of the Intracellular Vestibule of K+ Channels. *J. Mol. Biol.*, *254*, 272–288.

Kuo A., J. M. Gulbis, J. F. Antcliff, E. D. Lowe, J. Zimmer, F. M. Ashcroft, T. Ezaki, and D. A. Doyle (2003) Crystal Structure of the Potassium Channel KirBac1.1 in the Closed State. *Science (80-.).*, *300*(June), 1922–1927.

Kutluay E., B. Roux, and L. Heginbotham (2005) Rapid intracellular TEA block of the KcsA potassium channel. *Biophys. J.*, *88*(2), 1018–1029.

Li W., and R. W. Aldrich (2004) Unique Inner Pore Properties of BK Channels Revealed by Quaternary Ammonium Block. *J. Gen. Physiol.*, *124*(1), 43–57.

Milne J. L. S., M. J. Borgnia, A. Bartesaghi, E. E. H. Tran, L. A. Earl, D. M. Schauder, J. Lengyel, J. Pierson, A. Patwardhan, and S. Subramaniam (2013) Cryo-electron microscopy – a primer for the non-microscopist. *FEBS J.*, *280*, 28–45.

Nagel G., M. Brauner, J. F. Liewald, N. Adeishvili, E. Bamberg, and A. Gottschalk (2005) Report Light Activation of Channelrhodopsin-2 in Excitable Cells of Caenorhabditis elegans Triggers Rapid Behavioral Responses. *Curr. Biol.*, *15*, 2279–2284.

Piechotta, P.L., M. Rapedius, P.J. Stansfeld, M.K. Bollepalli, G. Ehrlich, I. Andres-Enguix, H. Fritzenschaft, N. Decher, M.S.P. Sansom, S.J. Tucker, and T. Baukrowitz (2011) The pore structure and gating mechanism of K2P channels. *The EMBO journal 30 (17), 3607–3619. 10.1038/emboj.2011.268*.

Rassendren F., G. Buell, A. Newbolt, R. A. North, and A. Suprenant (1997) Identification of amino acid residues contributing to the pore of a P2X receptor Franc. *EMBO J.*, *16*(12), 3446–3454.

Rauh O, U. P. Hansen, D. D. Scheub, G. Thiel, and I. Schroeder (2018) Site-specific ion occupation in the selectivity filter causes voltage- dependent gating in a viral K + channel., *8*(January), 1–15.

Rauh O, M. Urban, L. M. Henkes, T. Winterstein, T. Greiner, J. L. Van Etten, A. Moroni, S. M. Kast, G. Thiel, and I. Schroeder (2017) Identification of Intrahelical Bifurcated H-Bonds as a New Type of Gate in K+Channels. *J. Am. Chem. Soc.*, *139*(22), 7494–7503.

Riessner T. (1998) Level detection and extended beta distributions for the analysis of fast rate constants of Markov processes in sampled data. *PhD thesis, University of Kiel.*

Rondelli, V., E. Del Favero, P. Brocca, G. Fragneto, M. Trapp, L. Mauri, M.G. Ciampa, G. Romani, C.J. Braun, L. Winterstein, I. Schroeder, G. Thiel A. Moroni, and L. Cantu (2018). Directional K(+) channel insertion in a single phospholipidbilayer: Neutron reflectometry and electrophysiology in the joint exploration of a model membrane functional platform. *Biochim Biophys Acta Gen Subj, 1862(8), 1742-1750. doi:10.1016/j.bbagen.2018.05.007*

Schauder D. M., J. Lengyel, J. Pierson, and A. Patwardhan (2014) Cryo-electron microscopy : A primer for the non-microscopist. *FEBS Lett.*, *280*(1), 28–45.

Schroeder I. (2015) How to resolve microsecond current fluctuations in single ion channels: The power of beta distributions. *Channels*, *9*(5), 262–280.

Schultze R., and S. Draber (1993) A Nonlinear Filter Algorithm for the Detection of Jumps in Patch-Clamp Data. *J. Membr. Biol.*, *52*, 41–52.

Shimomura T., K. Irie, and Y. Fujiyoshi (2016) Molecular determinants of prokaryotic voltage-gated sodium channels for recognition of local anesthetics. *FEBS J.*, *283*, 2881–2895.

Spassova, M. and Z. Lu (1998) Coupled ion movement underlies rectification in an inward-rectifier K+ channel. *J Gen Physiol 112 (2), 211–221.*

Tan Q., B. Ritzo, K. Tian, and L.-Q. Gu (2012) Tuning the tetraethylammonium sensitivity of potassium channel Kcv by subunit combination. *J. Gen. Physiol.*, *139*(4), 295–304.

Tayefeh S., T. Kloss, M. Kreim, M. Gebhard, D. Baumeister, B. Hertel, C. Richter, H. Schwalbe, A. Moroni, G. Thiel, and S. M. Kast (2009) Model development for the viral Kcv potassium channel. *Biophys. J.*, 96, 485–498.

Thiel G., D. Baumeister, I. Schroeder, S. M. Kast, J. L. Van Etten, and A. Moroni (2011) Minimal art: Or why small viral K+ channels are good tools for understanding basic structure and function relations. *Biochim. Biophys. Acta - Biomembr.*

Thompson J., and T. Begenisich (2000) Interaction between Quaternary Ammonium Ions in the Pore of Potassium Channels Evidence Against an Electrostatic Repulsion Mechanism. *J. Gen. Physiol.*, *115*(June), 769–782.

Yellen G., M. E. Jurman, T. Abramson, and R. MacKinnon (1991) Mutations affecting internal TEA blockade identify the probable pore-forming region of a K+ channel. *Science*, *251*(4996), 939–942.

Zhou M., J. H. Morais-Cabral, S. Mann, and R. Mackinnon (2001) Potassium channel receptor site for the inactivation gate and quaternary amine inhibitors. *Nature*, *411*(June), 1–5.

3 Using Kcv channels for the developing of light-gated ion channel by modular design

3.1 Abstract

Viral K^+ channels are a small robust well studied model system of the pore module of complex ion channels. Kcv_{NTS} belongs to the ATCV-1 family and possesses a rather high unitary channel conductance and an open probability above 90%. By the coupling of the molecule MAL-AZO-QA, this channel is supposed to be controlled light-dependently. The TEA head group of this molecule is able to block the ion current. However, the sensitivity of Kcv_{NTS} to TEA is rather low. A mutation in the proximity of the selectivity filter increases this sensitivity. Furthermore, the single channel conductivity was significantly increased by the S42T mutation. The introduction of a Cys in the pore loop allows the coupling of the molecule to the channel. Although it was not possible to switch the channel light dependent, these experiments impressively show how viral K^+ channels can be used for modular design.

3.2 Introduction

Mechanisms for the sensing of electromagnetic radiation have emerged during evolution in various domains of life. In the absence of complex eye structures, metazoans have developed light-activated proteins (Fan & Lin, 2015). The class of opsin genes encode for proteins with seven transmembrane domains and a light-sensitive mechanism (Terakita, 2005). Opsin genes are divided into two subfamilies, the microbial opsins (type 1) and the animal opsins (type 2) (Becker et al., 2016). While type 1 opsin genes occur exclusively in prokaryotes, algae and fungi, type 2 genes are only present in higher eukaryotes and are mainly responsible for vision. Both types require the vitamin A like organic cofactor retinal, which serves as an antenna for photons (Seddon et al., 2010). When bound to a conserved lysine within the seventh transmembrane domain, the functional opsin is called rhodopsin. The light sensitivity of these proteins depends on a photoisomerization of retinal; absorption of photons in turn leads to structural changes in the protein, which initiate downstream signaling cascades. In type 2 opsins, the connection of protein and retinal is hydrolyzed after photoisomerization (Teller et al., 2003), in type 1 the retinal molecule does not dissociate but returns to its original state while still covalently bound to its partner. Type 1 opsins also include the subfamily of Channelrhodopsin (Nagel et al., 2002). These proteins originate from the unicellular alga *Chlamydomonas reinhardtii* and are light-activated non-selective cation channels. They combine the two tasks of light perception and ion conduction in a single protein. The pharmacological and genetic manipulation of specific cell types and expression profiles has

become more and more important. However, the temporary accuracy for manipulating individual neurons has been lacking. There was for a long time no technique available, which allowed to perform experiments with cellular precision and high temporal resolution within intact neural tissue. This is why Crick (1979) requested a new method that would allow him to manipulate cellular components of the brain individually.

The visionary idea of Crick has now been put into action thanks to the discovery of the light gated ion channel Channelrhodopsin (Nagel et al., 2002). This protein has been exploited in the last decade as a tool in biology for manipulating cellular activity by light. In this approach, called optogenetics, this light-sensitive channel and other light sensitive transport proteins are expressed in cells including neurons with the effect that the electrical activity of these cells can be controlled in a non-invasive manner by light. In seminal experiments Boyden et al. (2005), were introducing Channelrhodopsin into hippocampal neurons, where it provided millisecond precise control of neuronal activity.

Model organisms in which optogenetics channels have already been successfully used include C. elegans (Nagel et al., 2005), Drosophila (Zhang et al., 2007), zebrafish (White et al., 2008), rats (Lee et al., 2010) and primates (Han et al., 2009).

Regarding ion channels, in the last decade it was possible to suppress neuronal activity with ion pumps (Chow et al., 2010). Throughout optimization, Chuong et al. (2014) designed a red-shifted, high conductive chloride pump. But, illumination for prolonged periods, leads to a decline in efficiency over time. During a 60 s illumination, the peak activity can reduce to 50% - 90%. Further protein-engineering has also led to the development of the first potassium pumping rhodopsin (Gushchin et al., 2015).

In addition to retinal there are also non-biological chemical compounds that change their conformation by photoisomerization. The best studied is azobenzene (García-Amóros & Velasco, 2012). It is the simplest aromatic azo compound and consists of two phenyl rings linked by an N=N double bond. All compounds with this type of double bond are called diimides or diazene. They are able to absorb light and are used as dyes in various industries (Farooqi et al., 2016). Throughout the above mentioned photoisomerization the azobenzene can switch between a *trans* and a *cis* isomer. This switching is caused by appropriate wavelengths of light. While ultraviolet light leads to a conformational change from *trans* to *cis*, the azobenzene molecule changes from *cis* to *trans* under green light. Optogenetics has already made use of the reversible photoswitch of these molecules and created light-switchable ion channels with azo compounds (Banghart et al., 2004). Based on the photoactive conformational switching of azobenzol, channel proteins where designed and synthesized in which a channel blocker is linked via an azobenzol containing tether on the outside of modified channels. In one of these synthetic channels the molecule, MAL-AZO-QA, contains on one end a maleimide (MAL) for

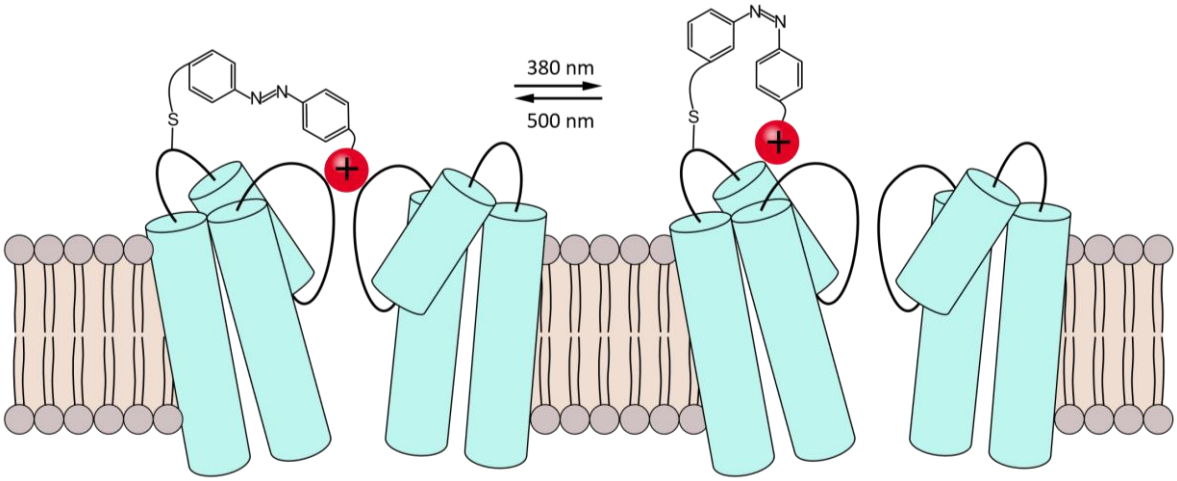

Figure 3.1: Photoisomerization of MAL-AZO-QA gates ionic current. Sketch of modified Kcv_{NTS} with bound MAL-AZO-QA. In the trans configuration the ion flow can be blocked, while after photoisomerization the *cis* configuration is too short to block effectively.

cysteine tethering and on the other and a quaternary ammonium (QA) group to block the channel; the azo group is positioned between these elements (Banghart et al., 2004).

For more than four decades, tetraethylammonium (TEA) has been used to probe for investigating K^+ channel pharmacology, permeation, gating structure and the dynamics of protein movement at both the internal and external end of the conduction pathway (Armstrong & Miller, 1988; MacKinnon & Yellen, 1990). Mutagenesis studies demonstrated that the amino acid residue in position 449 in the pore of the *Shaker* H4 potassium channel had a dramatic impact on the blocking potency of external TEA (MacKinnon & Yellen, 1990). It was also observed, that all four channel subunits contribute more or less equally to TEA blocking potency (Heginbotham & MacKinnon, 1992). A bulk of structural and functional data underscore that the amino acids at the position equivalent to *Shaker 449 determines* the primary site for TEA binding.

In the case of the MAL-AZO-QA molecule, the TEA-like head group is able to block the channel pore at position 449. Amino acid Glu^{422} is estimated to be 15-18 Å away from this TEA binding site. When a Cys is substituted at position Glu^{422}, MAL-AZO-QA is able to bind to *Shaker* and block the ion current in a light-dependent manner (Banghart et al., 2004).

While the *Shaker* H4 channel belongs to the voltage-dependent K^+ channels with six TM per subunit (Long et al., 2005), the viral potassium channel Kcv_{NTS} is with only two TM per subunit by far smaller (Kang et al., 2004). Due to their simple architecture, which is identical to the architecture of the pore module of more complex K^+ channels, they are easy to handle (Winterstein et al., 2018). In addition, Kcv_{NTS} possesses a rather high unitary channel conductance and an open probability above 90%. In addition, when transfected in cells, the

protein synthesis and its sorting to the plasma membrane is presumably faster that of other much larger channels. All these structural and functional features make the small Kcv type channels ideal tools for engineering new channels tools for optogenetics.

Kcv type channels were already used in the past for an engineering of a light-gated potassium channel (Cosentino et al., 2015). To create a single-component light-gated K^+ channel, the viral potassium channel Kcv_{PBCV-1} was therefore fused to the LOV2-Jα photosensory region of a plant blue-light receptor. The synthetic channel exhibits biophysical features of Kcv channels and photoactivates in blue light.

3.3 Results and Discussion

In experiments reported by Banghart et al. (2004), the voltage-dependent K^+ channel *Shaker* was modified in such a way that it could be switched light-dependently. For this purpose, the molecule MAL-AZO-QA was used. This small molecule can be coupled on one end to a cysteine in the extracellular loop of the channel protein. The quaternary ammonium residue on the other end of the MAL-AZO-QA molecule is able to block the channel depending on the conformation of the light switchable azobenzol. Since the head group of this molecule is almost identical to Tetraethylammonium (TEA), channels used for this kind of experiment have to be sensitive against TEA on the extracellular side. In principle, many potassium channels are highly sensitive to TEA, because they have a binding site at the extracellular pore entrance. All four subunits are equally involved in the potency of the block (Heginbotham & MacKinnon, 1992). Molecular dynamics studies have shown that the residues interact directly with the TEA molecule (Guidoni & Carloni, 2002). TEA binding leads to a reduction of the potassium current and this effect is selective for TEA. For example, whereas the external binding site is fairly selective for TEA, the internal binding site binds many TEA derivatives as well or even better than TEA itself (Armstrong & Hille, 1972).

TEA inhibits potassium channels because it acts like a fully hydrated potassium ion that cannot dehydrate (Armstrong, 1971). According to structural experiments performed by Lenaeus et al. (2005), TEA actually binds closer to the filter of the pore at the external site, than the last fully hydrated potassium ion. The half-maximal inhibition (IC_{50}) of the *Shaker* channel by external TEA is 0.35 ± 0.65 mM (Heginbotham, & MacKinnon, 1992). For the viral K^+ channel Kcv_{PBCV-1} the picture looks similar, the IC_{50} is at 0.41 ± 0.03 mM (Tan et al., 2012). There are no exact values known for the channels of the ATCV-1 family Kcv_{NTS} and Kcv_S. Greiner (2011) reports a reduction of the potassium inflow by approximately 10% - 20% with 10 mM TEA on the extracellular side. These measurements were made by patch clamp measurements in which only the sensitivity of the channel to extracellular TEA was monitored. Also, these measurements

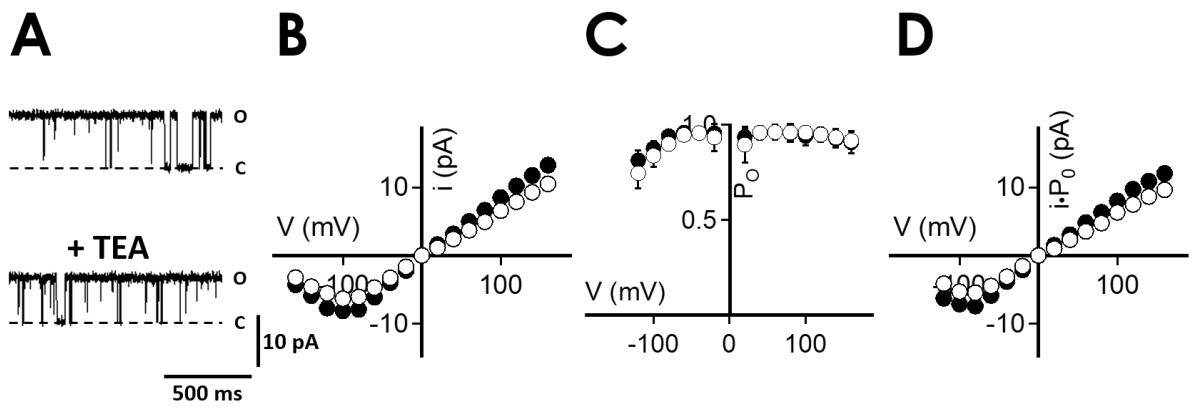

Figure 3.2: Kcv_{NTS} exhibits a low sensitive against external TEA. (A) Single channel fluctuations of Kcv_{NTS} in planar lipid bilayer at 120 mV w/o and with 10 mM TEA (+TEA) in external electrolyte solution. The closed **C** and open **O** levels are indicated along the current traces. (B) Mean i/V-relations and (C) Mean open probabilities. (D) Time-averaged I/V relations obtained by multiplying data in B with C. Recordings w/o (black) and with (white) external TEA. Mean data ± s.d. are from 3 independent recordings.

provided no information on the effect of TEA on the single channel level. To obtain more information for the effect of TEA on channels from the ATCV-1 family, Kcv_{NTS} was examined in the following using the lipid bilayer method.

Fig. 3.2 shows characteristic examples of single channel measurements of in vitro synthesized Kcv_{NTS} with the planar lipid bilayer technique in DPhPC membranes. The current amplitude increases almost linearly between -60 mV and +100 mV and has in this voltage window clearly defined open levels. Below -60 mV Kcv_{NTS} shows an increase in noise and an apparent decrease in current amplitude. This can be related to the phenomenon of flicker gating. This gating process has already been described for Kcv channels (Gazzarrini et al., 2009, Rauh et al., 2017) and has its origin in a fast gating mode that can no longer be resolved by the recording technique. This fast gating results in an increase in open channel noise and an apparent decrease of the channel amplitude at extreme negative voltages. The *i*/V curves can be described between -60 mV and +60 mV in approximation with Ohm's law.

$$i = \frac{V}{R} = \gamma \cdot V_0 \qquad \textbf{(3.1)}$$

Where *R* stands for the electrical resistance and γ for the single channel conductance. In the absence of external TEA, Kcv_{NTS} has a conductivity *g* of 86.8 ± 1.4 pS.

It has been described in Chapter 2.3 that the extracellular side of the channel is oriented towards the *trans* compartment of the bilayer chamber while the intracellular side faces

towards the *cis* compartment. After adding 10 mM of external TEA, the conductivity decreases over the entire voltage window by approximately 20%. This result corresponds to the effect of TEA on the same channel in HEK293 cells reported by Greiner (2011). The data suggest that Kcv_{NTS} exhibits only a low sensitivity against external TEA even though the channel is selective for potassium and has a high conductivity. In this respect it appears that Kcv_{NTS} is not a suitable candidate for constructing a synthetic light-dependent channel with the switchable MAL-AZO-QA molecule.

Sensitivity against TEA is attributed to a single amino acid

In the case of Kcv_{PBCV-1} channel, mutation studies have already been performed to tune TEA sensitivity (Tan et al., 2012). In this study the position Leu^{70} in the filter was identified as key amino acid for the regulation of TEA sensitivity. It was demonstrated that mutations of this residue can increase the TEA sensitivity 1000-fold. Leu^{70} ensures the optimal conformation of the protein for a high TEA affinity. Regarding the alignment (Fig. 3.3) of Kcv_{PBCV-1} and Kcv_{NTS}, the equivalent position to Leu^{70} in Kcv_{PBCV-1} is Thr^{53} in Kcv_{NTS}. This deviation in the primary sequence could be the reason for the low sensitivity of Kcv_{NTS} against TEA. To test this hypothesis, the mutant Kcv_{NTS} T53L was generated by site-directed mutagenesis. This point mutation leads in Kcv_{NH}, another close relative of Kcv_{NTS} in the ATCV-1 family, to an almost complete inactivation of the channel (Rösser, 2017). The average open probability of this mutant is only about 1%. The data suggest that the selectivity filter may remain in a collapsed state because they are unable to develop critical hydrogen bonds. Further scrutiny of the alignment reveals that the amino acid at position 69 of Kcv_{PBCV-1} and 52 of the ATCV-1 family are also different. While Kcv_{PBCV-1} has an Ile at this position, the other two ATCV type channels possess a Leu at the respective position. Since the stretch of amino acid sequence surrounding of the crucial position, which is responsible for TEA sensitivity, is highly conserved, the double mutant Kcv_{NTS} L52I T53L was generated.

Surprisingly, both channel mutants turned out to be functional. In detail, they show clear single channel amplitudes and moderate open probabilities (Fig. 3.4). However, the single channel conductance is reduced by 76% in the single mutant and 67% in the double mutant compared to the wt-Kcv_{NTS}. For the engineering endeavor the mutants have the advantage of a drastic increased sensitivity to external TEA. At the same time, they have the disadvantage of a large reduction in conductivity with the effect that this parameter is so low that after the addition of TEA it cannot be determined quantitatively. For these reasons, these two mutant channels are not suitable for the experiments with the aforementioned MAL-AZO-QA construct.

```
KcvPBCV-1   MLVFSKFLTRTEPFMIHLFILAMFVMIYKFFPGGFENNFSVANPDKKASWI
KcvNTS      ----------MLLLIIHLSILVIFTAIYKMLPGGMFSN-------TDPTWV
KcvNH       ----------MLLLIIHICILVFFTTVYKMLPGGMFSY-------ADPSWV
                        ::**: **.:*. :**::***: .         . :*:

KcvPBCV-1   DCIYFGVTTHSTVGFGDILPKTTGAKLCTIAHIVTVFFIVLTL-----     94
KcvNTS      DCLYFSASTHTTVGYGDLTPKSPVAKLTATAHMLIVFAIVISGFTFPW     82
KcvNH       DCIYFSASTHTTVGYGDLTPKSAVAKLTATAHMLIVFAIVVSSFTFPW     82
            **:**..:**:***:**: **:  *** : **:: ** **::
```

Figure 3.3: Sequence alignment of three viral K⁺ channels. Identical amino acids are labeled with stars. Conservative and semi-conservative amino acid are labeled with colons or dots respectively. The consensus sequence of K⁺ channels is highlighted in dark grey. The crucial position for the TEA sensitivity is highlighted in light grey.

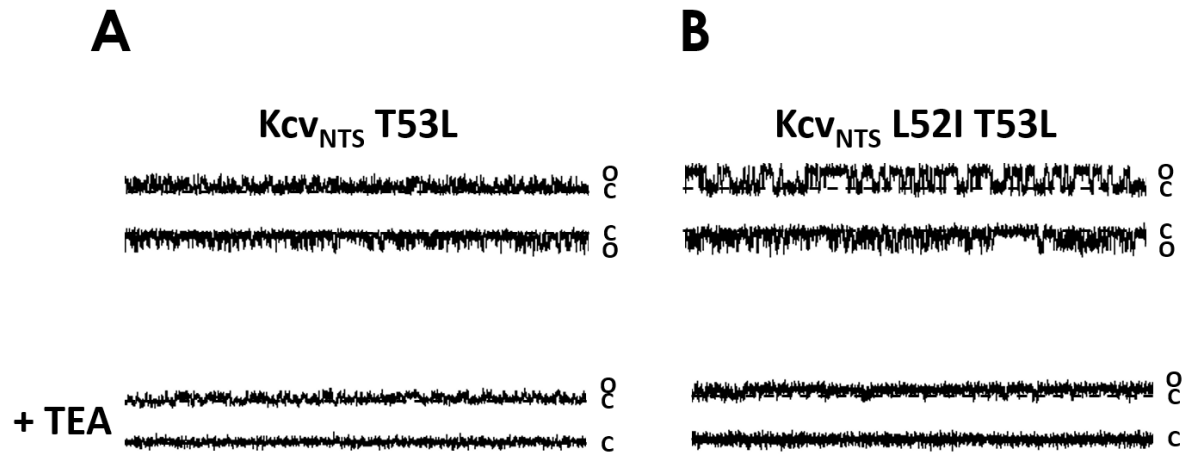

Figure 3.4: Mutations lead to an increased TEA sensitivity and in a decrease in unitary current. (A) Single channel fluctuations of Kcv_{NTS} T53L in planar lipid bilayer w/o and with 10 mM external TEA (+TEA). (B) Single channel fluctuations of Kcv_{NTS} L52I T53L w/o and with 10 mM external TEA. The closed **C** and open **O** levels are indicated along the current traces. The membrane voltage for the upper traces is 120 mV and -120 mV for the lower traces.

Increasing the unitary conductance by a single mutation

In KcsA, mutations of residue Glu^{71} have a dramatic effect on the hydrogen bridge network in close proximity to the selectivity filter (Cordero-Morales et al., 2011). The corresponding position Ser^{42} in Kcv_{NTS} plays the same role (Rauh et al., 2018). The structural model of Kcv_{NTS} suggests that this mutation has an effect on the anchoring of the selectivity filter. Here, the mutation S42T leads to a rearrangement of the hydrogen bridge network and can thus influence the channel structure or the potassium affinity. In the following experiments I tested whether the

introduction of the mutation S42T in the two channels Kcv_{NTS} T53L and Kcv_{NTS} L52I T53L has the same effect and increases the single channel conductivity.

As in the previous section, the planar lipid bilayer technique with synthetic DPhPC membranes was used to analyze the two channel proteins. With this single channel recording technique, the hypothesis on the influence of residue 42 on unitary conductance could be confirmed. The single channel conductivity was increased significantly by a point mutation at position Ser^{42} (Fig. 3.5). In the mutant Kcv_{NTS} S42T T53L the unitary conductance was increased 6-fold. After addition of 10 mM external TEA the conductivity decreased from 104 pS to 9 pS due to blocking of the extracellular pore entrance. The L52I T53L double mutant showed a similar picture as the S42T mutation. The triple mutant Kcv_{NTS} S42T L52I T53L has a conductivity of 117 pS, which is reduced by 84% in responds to external TEA. The Hill equation was used to calculate the affinity of the channel to TEA from dose-response curves.

As seen in Fig. 3.5C, both channels show a clear outward rectification although they do not possess a voltage sensor. The open probabilities are much lower at negative voltages than at positive ones. Other viral potassium channels also show rectifying properties without possessing a voltage sensor (Rauh et al., 2018). The origin of this effect was found in the immediate surrounding of the outer pore entrance.

An analysis of the single channel data shows that the interburst phases shorten and the open probabilities increase after adding external TEA. This phenomenon was also observed in Kcv_{PBCV-1} (Tan et al., 2012). It was assumed that this behavior could be equivalent to C-type inactivation. This gating phenomenon is associated with the extracellular pore mouth of K^+ channels; it was originally observed as a reduction of the conductivity of many voltage-dependent K^+ channels (Armstrong et al., 2014). According to Choi (1991) and Lopez-Barneo (1993), the hallmarks of C-type inactivation are an inhibition by high external K^+ or external TEA. These properties can be interpreted as 'foot in the door' mechanism, where the occupation of the binding site by K^+ or TEA at the external filter causes the conformational changes which prevents C-type inactivation (Kurata & Fedida, 2006; Meisel et al., 2018).

Close scrutiny of the dose-response curves shows that the TEA block exhibits a slight voltage dependency (Fig. 3.5D). When charged blockers enter the narrow confinement of the pore and bind at a site within the electric field, a voltage-dependent block occurs .
Since the block of Kcv_{NTS} is only weak, TEA presumably enters the electric field only very slightly. Another picture is shown when TEA is added on the intracellular side (Chapter 2.3). TEA must enter much deeper into the electric field, since the intracellular block is much more voltage-dependent. Based on data from other K^+ channels it seems that the reason for this phenomenon is related to the hydrophobicity of the blocker and not a specific structure of the channel protein (French & Shoukimas, 1981).

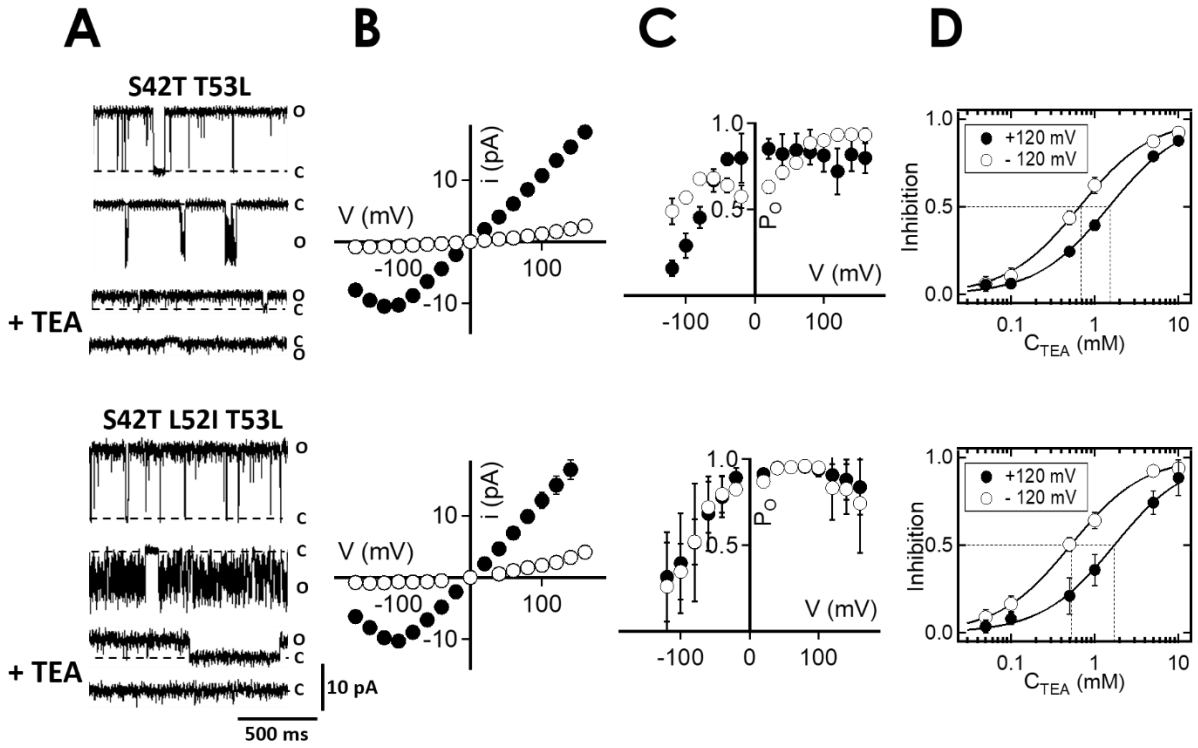

Figure 3.5: Single mutation increases the conductance of Kcv_{NTS}. (A) Single channel fluctuations of Kcv_{NTS} S42T T53L (top row) and Kcv_{NTS} S42T L52I T53L (bottom row) in planar lipid bilayer w/o and with 5 mM external TEA. The closed **C** and open **O** levels are indicated along the current traces. The membrane voltage for the upper traces is 120 mV and -120 mV for the lower traces. (B) Mean i/V-relations and (C) mean open probabilities. Recordings w/o (black) and with (white) external TEA. (D) Dose-response-curves. The solid lines are average curves and represent the fit to the Hill equation. The dotted line simplifies the readout of the K_D values. Mean data ± s.d. are from 3 independent recordings

To sum up, both mutant channels with an increased TEA sensitivity have acquired a high unitary conductance without compromising their sensitivity to external TEA. This combination of high single channel conductance and sensitivity to external TEA makes them suitable building blocks for engineering a light gated channel on the basis of the MAL-AZO-QA construct.

.

Introducing a binding site for MAL-AZO-QA

The initial idea to link a maleimide to *Shaker* via a flexible linker with a quaternary ammonium (QA) group had the following background: The aim was to find out how the S1-S4 domains are spatially related to the filter region (Blaustein et al., 2000). The amino acid Cys was therefore inserted at position Glu^{422} and the channel was exposed to various test molecules. These consisted of a sulfhydryl target, which can bind to the inserted Cys, and is covalently bound to a TEA molecule via a maleimide linker. If the test compound has a sufficient length and

orientation, the QA can reach the pore and block the ionic current. If the compound is too short or too long, the QA cannot reach the pore. While the block by TEA is reversible, the coupling to the channel protein creates a high local QA concentration, which cannot be washed out. By varying the length of the linker, the distance between the Cys and the TEA binding sites could now be measured. As an outcome from these experiments it was reported that the distance is approximately 15 Å (Blaustein et al., 2000). This approach was later modified by Banghart et al. (2004) in such a way, that they introduced a flexible linker, which includes a light sensitive azo compound. The known distance between E422C and the extracellular pore entrance was used to design the molecule MAL-AZO-QA. At a wavelength of 500 nm this tether is long enough for the QA to block the pore. If the wavelength is shortened to 380 nm, the length of the MAL-AZO-QA tether decreases from 17 Å to 10 Å by photoisomerization of the azobenzol component. In this conformation the QA headgroup is no longer able to reach the TEA binding site.

Transferred to the viral potassium channel Kcv_{NTS}, the amino acid homologous to Glu^{422} is located approximately at position 25 - 27. The exact position cannot be directly identified, because the distance to the TEA binding site is not known. The reason for this is that there is no crystal structure for Kcv_{NTS} available. The homology model, which was used here, is less accurate and may provide false distances between tether attachment and TEA binding site. For this reason, the Cys substitution was performed at three different positions in the extracellular loop. Furthermore, also the influence of Cys on the gating behavior of the channel was not known. It is known from previous studies that in Kcv_S a Cys at the intracellular pore entrance leads to the formation of disulfide bridges and this strongly impairs the unitary conductance (Rauh et al., 2017). To identify the best position for Cys in the Kcv_{NTS} mutants six different variants were generated by site-directed mutagenesis. These mutants should exhibit the following criteria: a high conductivity, high open probabilities and a good sensitivity to external TEA block. In detail, the following mutants were investigated: Kcv_{NTS} M25C/F26C/S27C S42T T53L and Kcv_{NTS} M25C/F26C/S27C S42T L52I T53L.

First, the triplet of cysteine mutants of Kcv_{NTS} S42T T53L was investigated. In the planar lipid bilayer, the mutants M25C and F26C show low open probabilities at negative voltages due to long closed-times between burst events (Fig. 3.6). Thus, these channels become strong outward rectifiers. This is interesting considering the fact that they do not feature a voltage sensor. The voltage dependency of the mutants results in a high variance in the measured values of open probabilities. More accurate results with smaller standard deviations could have been obtained by extending the recording time at test voltages to several minutes. However, since it was not the aim to investigate the origin of the long interburst phases, no further experiments were carried out. Also, no dose-response curves were generated and the IC_{50} was

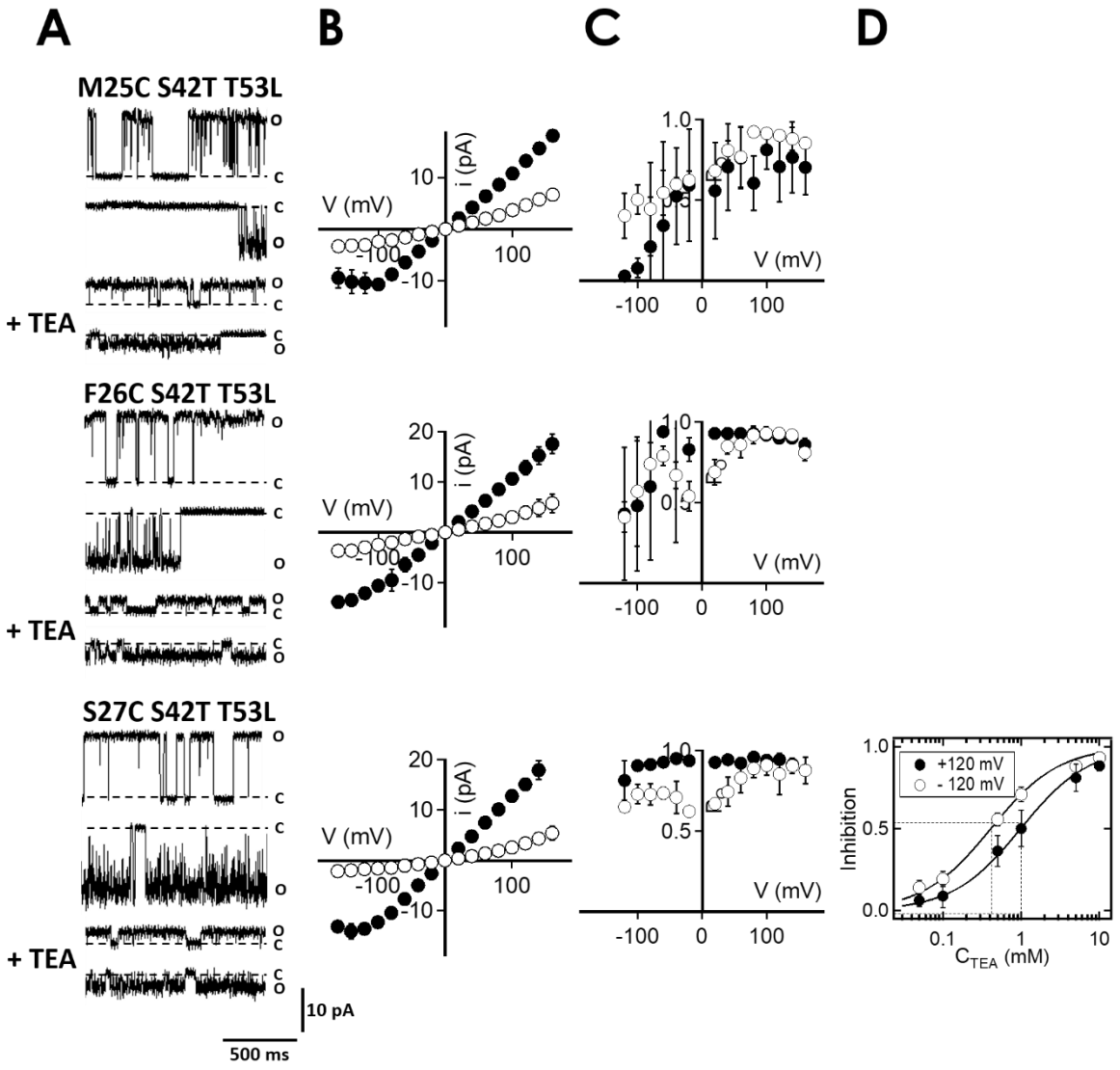

Figure 3.6: Functional properties of different cysteine mutants. (A) Single channel fluctuations of Kcv_{NTS} M25C S42T T53L (top row), Kcv_{NTS} F26C S42T T53L (central row), and Kcv_{NTS} S27C S42T T53L (bottom row) in planar lipid bilayer w/o and with 5 mM external TEA (+ TEA). The closed **C** and open **O** levels are indicated along the current traces. The membrane voltage for the upper traces is 120 mV and -120 mV for the lower traces. (B) Mean i/V-relations and (C) mean open probabilities. Recordings w/o (black) and with (white) external TEA. (D) Dose-response-curves. The solid lines are average curves and represent the fit to the Hill equation. The dotted line simplifies the readout of the K_D values. Mean data ± s.d. are from 3 independent recordings.

not calculated. Instead, these two channel mutants were considered unsuitable for further experiments.

In contrast, the mutant Kcv_{NTS} S27C S42T T53L does not show prolonged interburst phases at the single channel level (Fig. 3.6). In addition, it exhibits a high single channel conductance

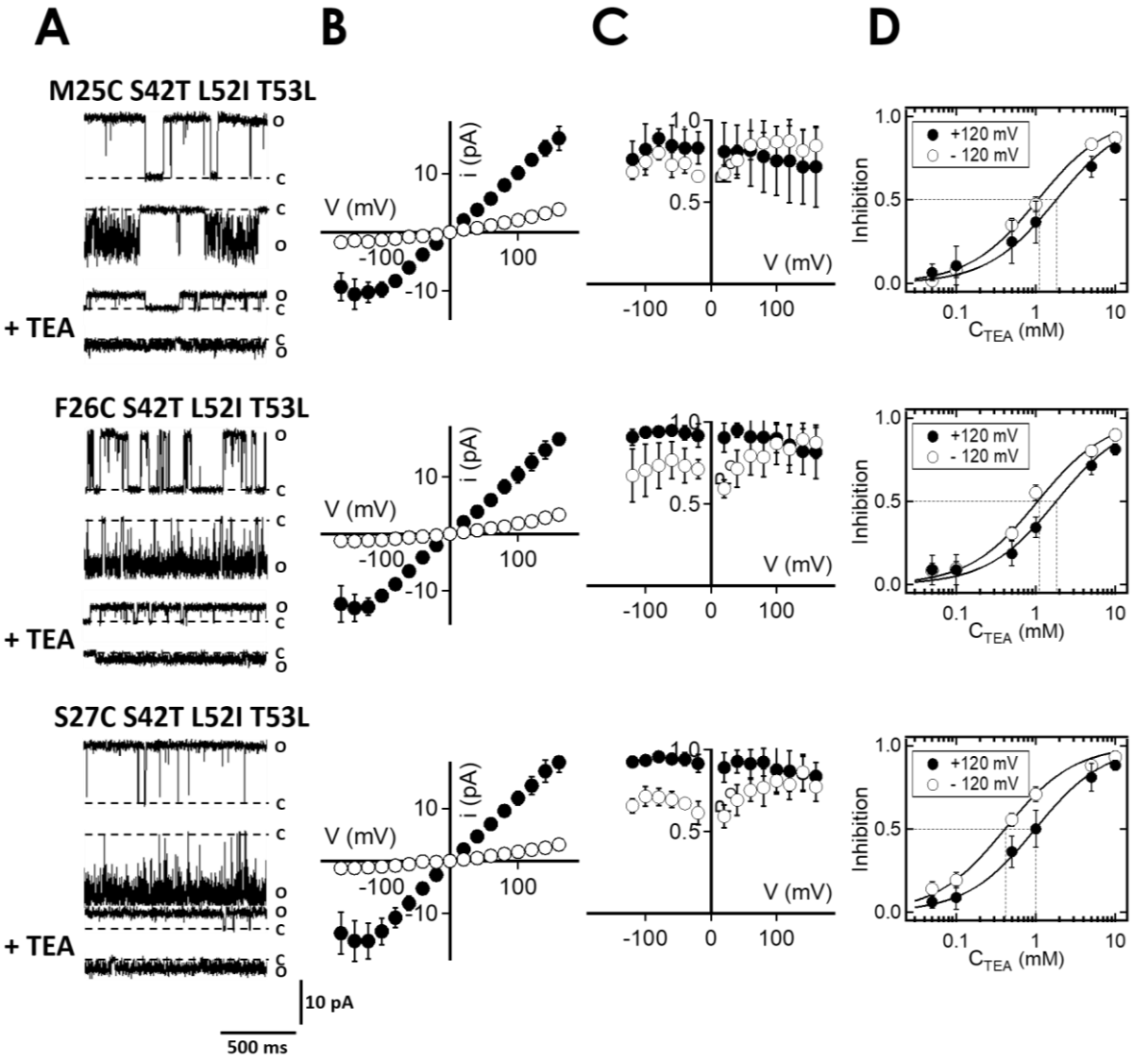

Figure 3.7: Functional properties of different cysteine mutants. (A) Single channel fluctuations of Kcv_{NTS} M25C S42T L52I T53L (top row), Kcv_{NTS} F26C S42T L52I T53L (central row), and Kcv_{NTS} S27C S42T L52I T53L (bottom row) in planar lipid bilayer w/o and with 5 mM external TEA (+ TEA). The closed **C** and open **O** levels are indicated along the current traces. The membrane voltage for the upper traces is 120 mV and -120 mV for the lower traces. (B) Mean i/V-relations and (C) mean open probabilities. Recordings w/o (black) and with (white) external TEA. (D) Dose-response-curves after increasing the external TEA concentration stepwise. The solid lines are average curves and represent the fit to the Hill equation. The dotted line simplifies the readout of the K_D values. Mean data ± s.d. are from 3 independent recordings.

and a favorable sensitivity towards external TEA with an IC_{50} of 2.6 ± 1.6 mM at 120 mV. These properties qualify this mutant for further experiments with MAL-AZO-QA.

The electrophysiological characterization of the second triplet is described in the following paragraph. The results are much more homogeneous than those obtained with the previous triplet. None of the three mutants shows an anomaly regarding their electrical properties or sensitivity to external TEA (Fig. 3.7). The unitary conductances are high as anticipated; the same

holds true for the open probabilities. The sensitivity to external TEA is within an ideal range with an approximate IC_{50} value of 1.1 mM at 120 mV. Accordingly, all variations of the viral potassium channel Kcv_{NTS} marked in Table 3.1 are suitable for further engineering endeavors in creating a light gated channel.

Table 3.1: Electrophysiological properties of different Kcv_{NTS} mutants. Summary of functional properties of six different TEA sensitive Kcv_{NTS} variants. The essential characteristics conductance, between 60 and -60 mV [pS], mean open probability [P_o], and the half maximal inhibitory concentration [mM] at 120 mV are compared. Some values were not evaluated (n.e.). The signs + and - indicate whether the channel constructs are suitable for further engineering of light sensitive channel. Mean data ± s.d. are from 3 independent recordings.

Channel mutant [Kcv_{NTS}]	I [pS]	P_o	IC_{50} [mM]	Suitable
M25C S42T T53L	128.5 ± 3.4	0.53 ± 0.2	n.e.	-
F26C S42T T53L	127.1 ± 21.2	0.75 ± 0.1	n.e.	-
S27C S42T T53L	151.8 ± 14.7	0.92 ± 0.02	2.6 ± 1.6	+
M25C S42T L52I T53L	116.7 ± 7.8	0.78 ± 0.16	1.2 ± 0.94	+
F26C S42T L52I T53L	121.3 ± 11.6	0.88 ± 0.07	1.2 ± 0.3	+
S27C S42T L52I T53L	151.1 ± 20.5	0.85 ± 0.06	1.06 ± 0.44	+

Preliminary investigations for the MAL-AZO-QA coupling

The MAL-AZO-QA molecule was custom made by company Enamine (Kiev, Ukraine). Before coupling to the K^+ channel, some additional control experiments were carried out to investigate the structure and functionality of the molecule. In a first step mass spectrometry was used to investigate the molecular structure of this chemical compound. In a second step the photoisomerization of the molecule was examined with the help of UV-Vis spectra. With these experiment it is possible to check whether the LEDs used as light sources are sufficient for switching the conformation of the azobenzol. In a third experiment I tested whether photoisomerization of the molecule is also taking place within the lipid bilayer chamber. Finally, I tested whether the coupling of a maleimide to a free sulfhydryl group is also possible within the chamber.

Mass spectrometry

Mass spectrometry is a technique used to separate electrically charged species from each other (Urban, 2016). For this purpose, the ions are distributed in a spectrum with regards to their mass-to-charge ratio. Either pure samples or complex mixtures can be analyzed (Sommer et al., 2006). This technique was be used to investigate whether the synthesized MAL-AZO-QA is present in the correct molecular mass. The investigation was carried out with electrospray ionization according to Fenn et al. (1989). The molecular mass was confirmed by ESI MS. The calculated mass/charge ratio of $[M+H^+]^+$ is 491.56 m/z. The measured value of the synthetic MAL-AZO-QA molecule is 491.2408 m/z. When comparing the simulated isotope distribution with the measured one, the masses correspond qualitatively. The spectra in (Fig. 3.8). show the mass that a proton has absorbed by electrospray ionization. The impurities of the sample are tiny as their intensity is rather low compared to the isotope distribution of MAL-AZO-QA (Fig. 6.1). Quantitatively speaking, since spectrometry is a well-established analytical method for the identification of substances, the molecule should be in the right configuration. Accordingly, the synthesized molecule can be used for the intended experiments.

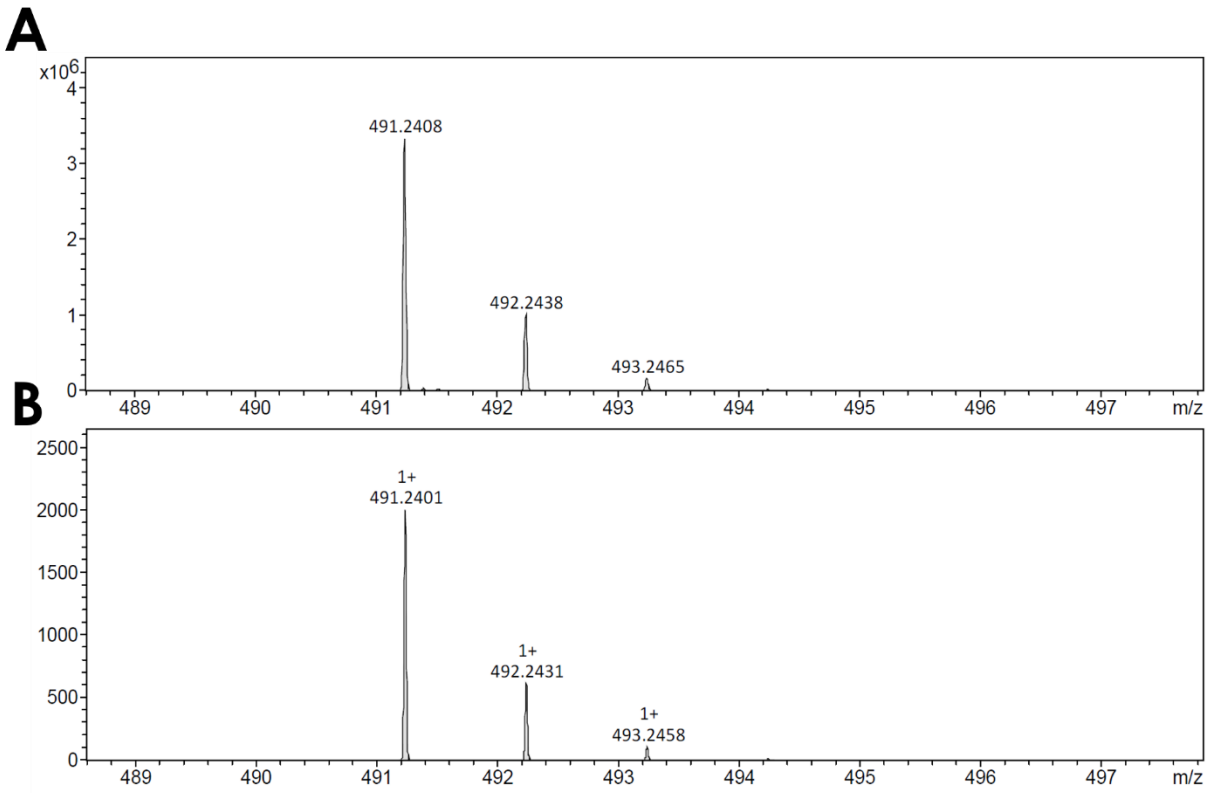

Figure 3.8: Mass spectrum of MAL-AZO-QA. (A) Measured isotope distribution of the sample containing the synthesized MAL-AZO-QA molecule. (B) Simulated isotope distribution. Shown are the intensities in correlation to the mass per charge. Both distributions are identical, therefore the mass is qualitatively right.

UV-Vis

After verifying that the synthetically produced molecule has the correct structure and conformation, it was investigated whether the LED light sources were sufficient to induce the conformational change of the azo compound. To examine the expected light induced transition of the azobene UV-Visible spectroscopy was used. With this method the different light-absorption between various states in the molecule can be investigated. The *trans* configuration of the MAL-AZO-QA should have a large absorbance peak at 360 nm and a small shoulder at about 440 nm (Banghart et al., 2004). After maximal photoisomerization to the *cis* configuration, the peak at 360 nm should be significantly reduced.

These expected transitions have been reproduced in the present control experiments (Fig. 3.9). After irradiation of one of the two samples for 30 seconds with the LED with 380 nm wavelength, the peak at 380 nm is clearly reduced. The intensity was 147 µmol/$M^{-2}s^{-1}$. Thus, a photoisomerization of the molecules has occurred. The effect could be reversed by irradiating the sample with the LED with 500 nm wavelength with an intensity of 470 µmol/$M^{-2}s^{-1}$ (Fig. 3.9C). The absorbance peak is now present again, whereas the other sample irradiated with the 380 nm LED no longer possesses the characteristic peak. These results show that the intensity of the two LEDs is sufficient to photoisomerize the MAL-AZO-QA molecule, i.e. to switch between *trans* and *cis* configuration.

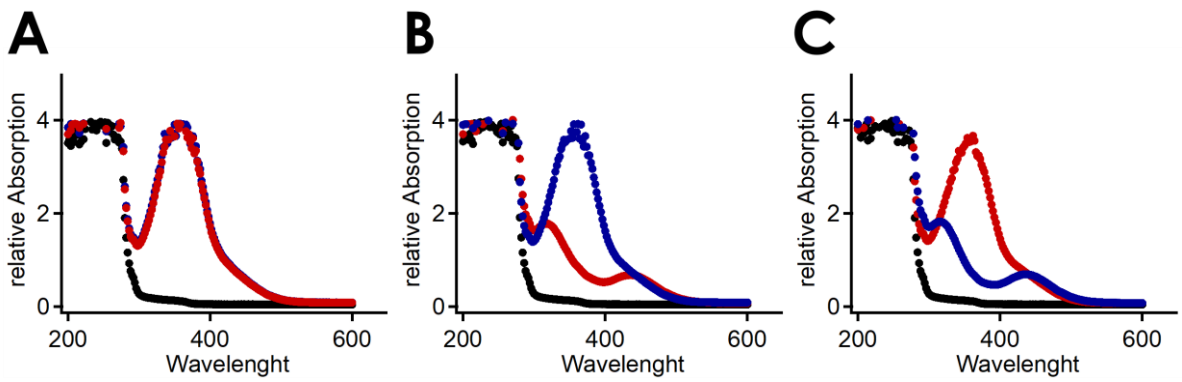

Figure 3.9: UV-Vis spectra of MAL-AZO-QA after light-irradiation with different wavelengths. Absorption of ddH_2O (black) and MAL-AZO-QA in a second (red) and third well (blue) between 200 nm and 600 nm. (A) Control measurement w/o irradiation. (B) Well 2 was irradiated with 380 nm UV-LED and well 3 with 500 nm LED. (C) Sample 2 was irradiated with 500 nm LED and sample 3 with 380 nm LED. The exposure time was 30 s and the intensity of the LEDs was 147 µol/$M^{-2}s^{-1}$ for the UV-LED and 470 µmol/$M^{-2}s^{-1}$for the green LED. As it can be seen, the sample which is irradiated with the 380 nm LED changes its relative absorption due to the conformational change from *trans* to *cis* configuration.

Photoisomerization inside the bilayer chamber

In the next set of experiments, I investigated whether the MAL-AZO-QA molecule can be photoisomerized inside the bilayer chamber by the LED light source. According to Banghart

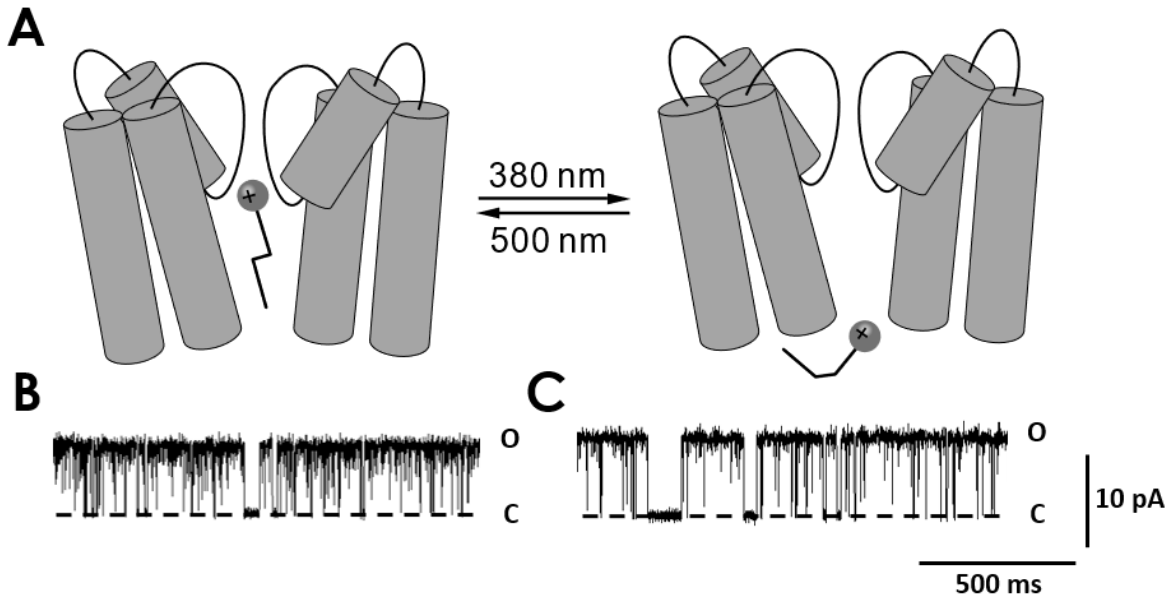

Figure 3.10: Light switchable intracellular block of MAL-AZO-QA. (A) Cartoon of Kcv_{NTS} with MAL-AZO-QA on the intracellular site. The linear *trans* isomer (right) is a better blocker than the bent *cis* isomer (left); the former can easier enter the cavity of the channel. (B) Single channel fluctuations after adding 50 µM MAL-AZO-QA into the *cis* chamber. The open channel noise is increased. (C) Irradiation with the 380 nm LED leads in the same channel to a decrease of the open channel noise due to the photoisomerization into the bent form. The closed **C** and open **O** levels are indicated along the current traces. The membrane voltage is 120 mV.

et al., (2009), this type of molecule can also block channel proteins from the intracellular side without being attached to the channel protein. In the free form the molecule can penetrate into the cavity of the channel and block the ion current for steric reasons (Fig. 3.10A). In this situation the linear *trans* isomer turns out to be a better blocker than the bent *cis* isomer, as the former can enter deeper into the cavity. Based on these considerations there should be a difference in the single channel current, depending on the irradiation of the bilayer chamber with blue or green light from the LED light source.

Fig. 3.10B shows channel fluctuations of Kcv_{NTS} after the addition of 50 µM MAL-AZO-QA into the *cis* chamber. The data are from a single measurement. The single channel noise in Fig. 3.3A is widened (1.14 pA) compared to experiments without internal MAL-AZO-QA (0.8 pA). The data show that the molecule in the linear conformation is able to enter the pore. This increase in open channel noise is consistent with the idea that internal linear MAL-AZO-QA generates a fast blocking process. In these recordings it is not possible to resolve the single events as it is the case with flicker gating (Schroeder & Hansen, 2007). In contrast, with a slower blocking process, the individual events could be resolved and one would observe a reduction in the open probabilities (Chapter 2.3). Since there is no binding site on the intracellular side of the channel and the MAL-AZO-QA probably cannot penetrate far into the cavity, the block is

very fast but significant. Irradiation with 380 nm light photoisomerized the molecule and transforms it into the bent *cis* configuration. Thus, it is no longer able to enter the cavity and the noise width decreases (0.98 pA). This experiment was not further multiplied and qualitatively analyzed. However, it can be assumed that photoisomerization of the MAL-AZO-QA works within the bilayer chamber.

Sulfhydryl coupling using N-ethylmaleimide

The coupling of the MAL-AZO-QA molecule is executed by a maleimide bond to the K^+ channel. The maleimide group attaches in this reaction covalently to a sulfhydryl target, which is provided by a cysteine within the protein. In the following experiments I examined, whether it is possible to carry out this coupling within the bilayer chamber. For this purpose, the mutant Kcv_{NTS} T53C was used, which has already been described in detail in chapter 2.3. Residue 53 is located at the extracellular pore entrance, directly at the TEA binding site. N-ethylmaleimide was used as coupling reagent. This significantly smaller imide should undergo after addition into the *trans* chamber, a maleimide bond with the sulfhydryl residue of Cys^{53}. Since this position is directly at the pore entrance, the molecular bond at this point should lead to a change of the ionic current through the channel.

The conductance of Kcv_{NTS} T53C is reduced after addition of N-ethylmaleimide to the *trans* chamber (Fig. 3.11). Thus, it is possible to perform the coupling of an imide to a sulfhydryl residue within the lipid bilayer chamber under the prevailing measuring conditions.

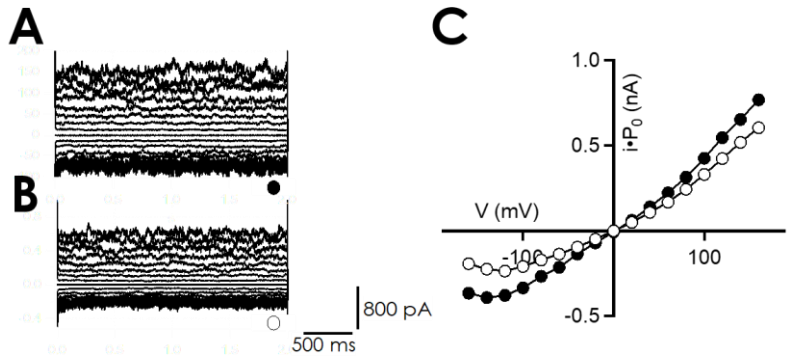

Figure 3.11: Multichannel measurement of Kcv_{NTS} T53C with N-ethylmaleimide. Multichannel measurement of Kcv_{NTS} T53C in planar lipid bilayer before (A) and after (B) the addition of 5 mM N-ethylmaleimide. (C) Time-averaged I/V-curve. N-ethylmaleimide is able to bind to the free sulfhydryl group at position 53 and reduces the conductance of the channels.

3.4 Conclusion

About 13 K^+ channels of the ATCV-1 family are included in the database of the National Center for Biotechnology Information[3] (2019). With a size of only 82 amino acids per subunit, these potassium channels are among the smallest of their kind. Despite their size, they exhibit all major features of K^+ channels (Gazzarrini et al., 2009). This includes assembling into a tetramer, K^+ selectivity and a sensitivity to canonical K^+ channel blockers. The variability of the different channels with respect to their primary amino acid sequence is reflected in a variability in functional features including unitary conductance and channel gating (Siotto et al., 2017). All these structural and functional features and the fact that these small channels are easy to handle (Winterstein et al., 2018) make viral potassium channels ideal components for modular design. Recent publications have shown that viral K^+ channels are in particular suitable building blocks for the engineering of synthetic ion channels (Cosentino et al., 2015).

The aim of this work was, to generate a light-gated potassium channel of the ATCV-1 family. Inspired by the design principles of Banghart et al. (2004), it was planned to link a K^+ channel blocker via a light sensitive tether to a viral K^+ channel. As a prerequisite for this endeavor it was first necessary to find a suitable K^+ channel with a high sensitivity against TEA, a conductance around 100 pS and a high mean open probability. Furthermore, a cysteine mutation has to be introduced in the extracellular loop of the channel protein in a way that this mutation is not negatively influencing the electrophysiological properties of the channel.

In a first step, the sensitivity of the viral K^+ channel Kcv_{NTS} against external TEA was increased. This was achieved by a single mutation at the extracellular pore entrance according to Tan et al. (2012). In a second step, the conductance, which was reduced as a result of the mutation in step one, was again elevated. The introduction of Ser at position 42 caused a significant 6-fold increase of the current amplitude. Lastly, a cysteine at the extracellular loop was introduced to ensure to coupling of the MAL-AZO-QA.

However, it was not possible to regulate the gating of Kcv_{NTS} light-dependently. The reason for this could not be found in this work. Nevertheless, these experiments impressively show how simple modular design function is using viral potassium channels.

[3] https://blast.ncbi.nlm.nih.gov/Blast.cgi

3.5 Methods

Mutagenesis

The viral potassium channels Kcv_{NTS} is a member of the ATCV subfamily. The coding sequences of this channel was cloned into the pEXP5-CT/TOPO vector in order to express them cell-free. The TA Expression Kit (Invitrogen, Carlsbad, CA, USA) was used for this purpose. A downstream stop-codon ensures that the proteins are expressed in their natural form. The amplified DNA fragments were separated with an agarose gel and then purified with the Zymoclean™ Gel DNA Recovery Kit (Zymo Research, Irvine, CA, USA). The plasmids were amplified by DH5α cells and extracted with the ZR Plasmid Miniprep™ Classic Kit (Zymo Research, Irvine, CA, USA). Following Papworth et al. (1996), mutations were inserted using PCR-based site-directed mutagenesis. The PCR products were separated in an agarose gel and purified via gel extraction. The template DNA was digested using FastDigest DpnI (ThermoFischer Scientific, Waltham, MA, USA). With 5 µL of the purified PCR product 50 µL of chemically competent DH5α were transformed. The heat shock took place at 42 °C for 60 seconds. After incubation at 37 °C overnight positive clones were selected. The LB medium of the agar plates consisted of 10 g/L tryptone, 5 g/L yeast extract, 5 g/L NaCl, 20 g/L agar, (pH adjusted with 1 M NaOH) and 50 µg/mL ampicillin. The plasmid DNA was purified using the ZR Plasmid Miniprep™ Classic Kit.

In vitro protein expression and purification

The expression of channel proteins was performed as described previously (Winterstein et al., 2018). Expression and translation were performed with the MembraneMax HN Protein Expression Kit (Invitrogen, Carlsbad, CA, USA) in the presence of nanolipoproteins (NLPs) following the manufacturer's instructions. They contain several His-tags to ensure subsequent purification by metal chelate affinity chromatography. The reaction mixture, with a volume of 50 µL, was loaded onto a HisPur Ni-NTA spin column (ThermoFisher Scientific, Waltham, MA, USA). Only the elution step was not as prescribed in the manufacturer's instructions. Here, the spin column was washed three times with 250 mM imidazole.

Planar lipid bilayer experiments

All lipid bilayer experiments were performed at room temperature (20-25 °C) by using a conventional vertical bilayer set-up (IonoVation, Osnabrück, Germany). As described by Braun et al. (2013) the recording chambers were connected with Ag/AgCl electrodes to the head-stage. To amplify the signal, the patch-clamp amplifier L/M EPC-7 (List-Medical, Darmstadt, Germany) was used. The current responses were filtered with a 4-pole Bessel filter

at 1 kHz and digitized with a sampling frequency of 5 kHz with an A/D converter (LIH 1600, HEKA Elektronik, Lambrecht, Germany). The used lipid was composed of 1,2-diphytanoyl-sn-glycero-3-phosphocholine (DPhPC, Avanti Polar Lipids, Alabaster, AL, USA). The bilayers were formed using the pseudo painting/air bubble technique (Braun et al., 2014). The electrolyte solution contained 100 mM KCl and was buffered with 10 mM HEPES. The pH of 7 was adjusted with 1 M KOH. The purified protein was diluted in 250 mM imidazole. A small amount was added to the *trans* compartment directly below the bilayer by using a curved Hamilton syringe. Constant voltages were applied for one to five minutes, after the successful incorporation of a single channel into the membrane. In 20 mV increments, the voltage was changed generally between +160 mV and -160 mV.

Data Analysis

The single channel measurements were recorded with Patchmaster (HEKA Elektronik, Lambrecht, Germany). For further data evaluation the custom-made program KielpatchDA was used. The single channel amplitudes were evaluated visually. To determine the open probabilities an automated Hinkley jump detector (Schultze & Draber, 1993) was applied. The dwell time histograms were fitted with one to three exponential functions. A certain number of closed events are missing due to the limited time resolution. The calculated fitting parameters were used to correct the mean lifetime of the open state. The missed events should be randomly distributed and have no impact on the entire open-time of the channel. The dose–response relations of the blocker were obtained using voltage steps from +160 mV to -160 mV in 20 mV increments for 120 s. The fraction of current blocked (F_B) was calculated as:

$$F_B = 1 - \frac{i}{i_0} \tag{3.2}$$

where i is the current in the presence and i_0 is the current in the absence of blocker. For each QA, the apparent dissociation constant, K_D, was obtained at a given voltage by fitting F_B as a function of blocker concentration with the Hill equation:

$$F_B = \frac{[QA]^s}{K^s{}_D + [QA]^s} \tag{3.2}$$

where s is the steepness factor and [QA] is the quaternary ammonium concentration. The voltage dependence of K_D was obtained by plotting the value obtained from the Hill equation fit as a function of voltage.

Mass spectrometry

The analysis of MAL-AZO-QA using mass spectrometry was performed by the MS department of the Technical University Darmstadt, deploying the method of electrospray ionization (Fenn et al., 1989). For this purpose, the TOF-Q impact II spectrometer (Bruker Daltonik GmbH, Bremen, Germany) was used.

UV-Vis

The plate reader Spark® (Tecan Trading AG, (Männedorf, Switzerland) was used to generate the absorption spectra. First, distilled water (blank) was added to one well of the plate and 1 mM MAL-AZO-QA dissolved in the electrolyte solution generally used for channel recordings was added to two other wells. The absorption was then measured between 200 nm and 600 nm, as the point of photoisomerization is in this range. Following that, the wells were irradiated with the 380 nm LED (0.4 mW/cm^2) for 30 s and the absorption was measured again. In the second run the wells were irradiated with 500 nm light from the second LED (3.8 mW/cm^2).

3.6 References

Armstrong C. M., and B. Hille (1972) The Inner Quaternary Ammonium Ion Receptor in Potassium Channels of the Node of Ranvier. *J. Gen. Physiol.*, *59*, 388–400.

Armstrong C. M., and T. Hoshi (2014) K^+ channel gating: C-type inactivation is enhanced by calcium or lanthanum outside. *J. Gen. Physiol.*, *144*(3), 221–230.

Banghart M., K. Borges, E. Isacoff, D. Trauner, and R. H. Kramer (2004) Light-activated ion channels for remote control of neuronal firing. *Nat Neurosci.*, *7*(12), 1381–1386.

Becker E. A., A. I. Yao, P. M. Seitzer, T. Kind, T. Wang, R. Eigenheer, K. S. Y. Shao, V. Yarov-yarovoy, and M. T. Facciotti (2016) A Large and Phylogenetically Diverse Class of Type 1 Opsins Lacking a Canonical Retinal Binding Site. *PLoS One*, *11*(6), 1–20.

Blaustein R. O., P. A. Cole, C. Williams, and C. Miller (2000) Tethered blockers as molecular "tape measures" for a voltage-gated K+channel. *Nat. Struct. Biol.*, *7*(4), 309–311.

Boyden E. S., F. Zhang, E. Bamberg, G. Nagel, and K. Deisseroth (2005) Millisecond-timescale , genetically targeted optical control of neural activity. *Nat. Neurosci.*, *8*(9), 1263–1268.

Braun C. J., T. Baer, A. Moroni, and G. Thiel (2014) Pseudo painting/air bubble technique for planar lipid bilayers. *J. Neurosci. Methods*, *233*, 13–17.

Choi K. L., R. W. Aldricht, and G. Yellen (1991) Tetraethylammonium blockade distinguishes two inactivation mechanisms in voltage-activated Ki channels. *Proc. Natl. Acad. Sci U.S.A.*, *88*(June), 5092–5095.

Chow B. Y., X. Han, A. S. Dobry, X. Qian, A. S. Chuong, M. Li, M. A. Henninger, G. M. Belfort, Y. Lin, P. E. Monahan, and E. S. Boyden (2010) High-performance genetically targetable optical neural silencing by light-driven proton pumps. *Nature*, *463*(7277), 98–102.

Chuong A. S., M. L. Miri, V. Busskamp, G. A. C. Matthews, L. C. Acker, A. T. Sørensen, A. Young, N. C. Klapoetke, M. A. Henninger, S. B. Kodandaramaiah, M. Ogawa, S. B. Ramanlal, R. C. Bandler, B. D. Allen, C. R. Forest, B. Y. Chow, X. Han, Y. Lin, K. M. Tye, B. Roska, J. A. Cardin, and E. S. Boyden (2014) Noninvasive optical inhibition with a red-shifted microbial rhodopsin. *Nat. Publ. Gr.*, *17*(8), 1123–1129.

Cordero-Morales J. F., E. O. Gracheva, and D. Julius (2011) Cytoplasmic ankyrin repeats of transient receptor potential A1 (TRPA1) dictate sensitivity to thermal and chemical stimuli. *Proc. Natl. Acad. Sci U.S.A.*, *108*(46).

Cosentino C., L. Alberio, S. Gazzarrini, M. Aquila, E. Romano, S. Cermenati, P. Zuccolini, J. Petersen, M. Beltrame, J. L. Van Etten, J. M. Christie, G. Thiel, and A. Moroni (2014) Engineering ofa light-gated potassium channel. *Science (80-.).*, *9844*(2011).

Crick F. H. (1979) Thinking about the brain. *Sci. Am.* US: Scientific American, Inc.

Fan L. Z., and M. Z. Lin (2016) Optical control of biological processes by light-switchable proteins. *Wiley Interdiscip Rev Dev Biol*, *4*(5), 545–554.

Farooqi M. J., M. A. Penick, J. Burch, G. R. Negrete, and L. Brancaleon (2016) Characterization of novel perylene diimides containing aromatic amino acid side chains. *Spectrochim Acta A Mol Biomol Spectrosc.*, *153*, 124–131.

Fenn J. B., M. Mann, C. K. A. I. Meng, S. F. Wong, and C. M. Whitehouse (1989) Electrospray Ionization for Mass Spectrometry of Large Biomolecules. *Science (80-.).*, *246*(6), 64,71.

Fork R. (1971) Laser Stimulation of Nerve Cells in Aplysia. *Science (80-.).*, *3*(1968), 907–908.

French R. J., and J. J. Shoukimas (1981) Blockage of squid axon potassium conductance by internal tetra-N-alkylammonium ions of various sizes. *Biophys. J.*, *34*(2), 271–291.

García-amorós J., and D. Velasco (2012) Recent advances towards azobenzene-based light-driven real-time information-transmitting materials. *Beilstein J. Org. Chem.*, *8*, 1003–1017.

Gazzarrini S., M. Kang, A. Abenavoli, G. Romani, C. Olivari, D. Gaslini, G. Ferrara, J. L. van Etten, M. Kreim, M. S. Kast, G. Thiel, and A. Moroni (2009) Chlorella virus ATCV-1 encodes a functional potassium channel of 82 amino acids. *Biochem. J*, *420*(2), 295–303.

Greiner T. (2011) Characterization of novel potassium transport proteins from Chlorella viruses. *Diss. Tech. Univ. Darmstadt*.

Guidoni L., and P. Carloni (2002) Tetraethylammonium binding to the outer mouth of the KcsA potassium channel: Implications for ion permeation. *J. Recept. Signal Transduct.*, *22*(1–4), 315–331.

Gushchin I., V. Shevchenko, V. Polovinkin, K. Kovalev, A. Alekseev, E. Round, V. Borshchevskiy, T. Balandin, A. Popov, T. Gensch, C. Fahlke, C. Bamann, D. Willbold, G. Büldt, E. Bamberg, and V. Gordeliy (2015) Crystal structure of a light-driven sodium pump. *Nat. Publ. Gr.*, *22*(5), 390–395.

Han X., X. Qian, J. G. Bernstein, H. Zhou, G. T. Franzesi, P. Stern, R. T. Bronson, A. M. Graybiel, R. Desimone, and S. Edward (2010) Millisecond-Timescale Optical Control of Neural Dynamics in theNonhuman Primate Brain. *Neuron*, *62*(2), 191–198.

Heginbotham L., and R. MacKinnon (1992) The aromatic binding site for tetraethylammonium ion on potassium channels. *Neuron*, *8*(3), 483–491.

Kang M., A. Moroni, S. Gazzarrini, D. DiFrancesco, G. Thiel, M. Severino, and J. L. Van Etten (2004) Small potassium ion channel proteins encoded by chlorella viruses. *Proc. Natl. Acad. Sci. U. S. A.*, *101*(15), 5318–5324.

Kurata H. T., and D. Fedida (2006) A structural interpretation of voltage-gated potassium channel inactivation. *Biophys. Mol. Biol.*, *92*, 185–208.

Lee J. H., R. Durand, V. Gradinaru, F. Zhang, I. Goshen, D. Kim, L. E. Fenno, C. Ramakrishnan, and K. Deisseroth (2011) Global and local fMRI signals driven by neurons definedoptogenetically by type and wiring. *Nature*, *465*(7299), 788–792.

Lopez-Barneo J., T. Hoshi, S. H. Heinemann, and R. W. Aldrich (1993) Effects of external cations and mutations in the pore region on C-type inactivation of Shaker potassium channels. *Receptors Channels*, *1*(1), 61–71.

MacKinnon R., and G. Yellen (1990) Mutations Affecting TEA Blockade and Ion Permeation in Voltage-Activated K + Channels m). *Sciene*, *250*(4978), 276–279.

Meisel E., W. Tobelaim, M. Dvir, Y. Haitin, A. Peretz, and B. Attali (2018) Inactivation gating of Kv7.1 channels does not involve concerted cooperative subunit interactions. *Channels (Austin).*, *12*(1), 89–99.

Miller C. (1988) Competition for Block of a Ca2+-Activated K+ Channel by Charybdotoxin and Tetraethylammonium-. *Neuron*, *1*, 1003–1006.

Nagel G., M. Brauner, J. F. Liewald, N. Adeishvili, E. Bamberg, and A. Gottschalk (2005) Report Light Activation of Channelrhodopsin-2 in Excitable Cells of Caenorhabditis elegans Triggers Rapid Behavioral Responses. *Curr. Biol.*, *15*, 2279–2284.

Nagel G., D. Ollig, M. Fuhrmann, S. Kateriya, A. M. Musti, E. Bamberg, and P. Hegemann (2002) Channelrhodopsin-1 : A Light-Gated Proton Channel in Green Algae. *Science (80-.).*, *296*(June), 2395–2399.

Rauh O., U. P. Hansen, D. D. Scheub, G. Thiel, and I. Schroeder (2018) Site-specific ion occupation in the selectivity filter causes voltage-dependent gating in a viral K+channel. *Sci. Rep.*, *8*(1), 1–15.

Rauh O, M. Urban, L. M. Henkes, T. Winterstein, T. Greiner, J. L. Van Etten, A. Moroni, S. M. Kast, G. Thiel, and I. Schroeder (2017) Identification of Intrahelical Bifurcated H-Bonds as a New Type of Gate in K+Channels. *J. Am. Chem. Soc.*, *139*(22), 7494–7503.

Rösser S. (2017) Influence of the outer pore mouth on the voltage dependence of the viral potassium channel Kcv NH. *Bachelor Thesis Tech. Univ. Darmstadt*.

Schmucker D., A. L. Sut, A. Beermannt, H. Jackle, and D. G. Jayt (1994) Chromophore-assisted laser inactivation of patched protein switches cell fate in the larval visual system of Drosophila. *Proc Natl Acad Sci U S A*, *91*(March), 2664–2668.

Schroeder I., and U. Hansen (2007) Saturation and Microsecond Gating of Current Indicate Depletion-induced Instability of the MaxiK Selectivity Filter., *130*(1), 83–97.

Schultze R., and S. Draber (1993) A Nonlinear Filter Algorithm for the Detection of Jumps in Patch-Clamp Data. *J. Membr. Biol.*, *52*, 41–52.

Seddon A. M., P. Curnow, and P. J. Booth (2004) Membrane proteins, lipids and detergents: Not just a soap opera. *Biochim. Biophys. Acta - Biomembr.*, *1666*(1–2), 105–117.

Sommer U., H. Herscovitz, F. K. Welty, and C. E. Costello (2006) LC-MS-based method for the qualitative and quantitative analysis of complex lipid mixtures. *J. LLipid Reasearch*, *47*, 804–814.

Tan Q., B. Ritzo, K. Tian, and L.-Q. Gu (2012) Tuning the tetraethylammonium sensitivity of potassium channel Kcv by subunit combination. *J. Gen. Physiol.*, *139*(4), 295–304.

Teller D. C., R. E. Stenkamp, and K. Palczewski (2003) Evolutionary analysis of rhodopsin and cone pigments: connecting the three-dimensional structure with spectral tuning and signal transfer. *FEBS Lett.*, *555*(1), 151–159.

Terakita A. (2005) Protein family review The opsins. *Genome Biol.*, *6*(213), 1–9.

Urban P. L. (2016) Quantitative mass spectrometry: an overview. *Phil.Trans.R. Soc. A*, *374*(20150382).

White R. M., A. Sessa, C. Burke, T. Bowman, C. Ceol, C. Bourque, M. Dovey, W. Goessling, E. Burns, and L. I. Zon (2008) Transparent adult zebrafish as a tool for in vivo transplantationanalysis. *Cell Stemm Cell*, *2*(2), 183–189.

Winterstein L. M., K. Kukovetz, O. Rauh, D. L. Turman, C. Braun, A. Moroni, and I. Schroeder (2018) Reconstitution and functional characterization of ion channels from nanodiscs in lipid bilayers. *J. Gen. Physiol.*, *150*(4), 637–646.

Zagotta W. N., T. Hoshi, and R. W. Aldrich (1990) Restoration of Inactivation in Mutants of Shaker Potassium Channels by a Peptide Derived from ShB. *Science (80-.).*, *250*(4980), 568–571.

Zhang J., K. L. Schulze, P. R. Hiesinger, K. Suyama, S. Wang, M. Fish, M. Acar, R. A. Hoskins, H. J. Bellen, and M. P. Scott (2007) Thirty-One Flavors of Drosophila Rab Proteins. *Genet. Soc. Am.*, *1322*(June), 1307–1322.

Zhou Y., L. Guan, J. A. Freites, and H. R. Kaback (2008) Opening and closing of the periplasmic gate in lactose permease. *Proc. Natl. Acad. Sci. U. S. A.*, *105*(10), 3774–3778.

4 Photolithographic production of small and defined apertures in laminates of dry film polymer sheets for channel recordings in planar lipid bilayers

This chapter was published with small modifications in El Khoury M., T. Winterstein, W. Weber, V. Stein, H. F. Schlaak, and G. Thiel (2018) Photolithographic fabrication of micro apertures in dry film polymer sheets for channel recordings in planar lipid bilayers. *The Journal of Membrane Biology; https://doi.org/10.1007/s00232-019-00062-9*

4.1 Abstract

Planar lipid bilayers constitute a versatile method for measuring the activity of protein channels and pores on a single molecule level. Ongoing efforts attempt to tailor this method for detecting biomedically relevant target analytes or for high-throughput screening of drugs. To improve the mechanical stability of bilayer recordings, we use a thin-film epoxy resist ADEX as septum in free-standing vertical bilayers. Defined apertures with diameters between 30 µm and 100 µm were micro-fabricated by photolithography. The performance of these septa was tested by functional reconstitution of the K^+ channel Kcv_{NTS} in lipid bilayers spanned over apertures in ADEX or Teflon films; the latter is conventionally used in bilayer recordings and serves as reference. We observe that the functional properties of the K^+ channel are identical in both materials while ADEX provides no advantage in terms of capacitance and signal-to-noise ratio. In contrast to Teflon however, ADEX enables long-term experimental recordings while the stability of the lipid bilayer is not compromised by pipetting solutions in and out of the recording chamber. Combined with the fact that the ADEX films can be cleaned with acetone, our results suggest that ADEX carries great potential for multiplexing bilayer chambers in robust and reusable sensing devices.

4.2 Introduction

Channel proteins catalyze the diffusion of ions across lipid membranes. This can occur in a highly regulated and selective manner through canonical ion channels (Hille, 2001), or less selectively via highly conductive beta barreled pores (Delcour, 2002). Considering the function of ion channels is crucial for a large variety of cellular events (Ashcroft, 2006), their underlying structure/function relationships are intensively studied in the context of their physiological and

pathophysiological activity (Kurachi & North, 2004; Catterall et al., 2017). For the same reason, ion channels are also considered promising drug targets (Terstappen et al., 2010; Yu et al., 2016). In recent years, pore-forming proteins, so-called protein nanopores, have also received great attention from protein engineers (Ayub & Bayley, 2016). These proteins can be genetically modified to sense various physical stimuli (e.g. voltage, mechanical stress) and chemical signals and molecules (e.g. ligands, pH, DNA, etc.) in a highly sensitive and selective fashion. Sensing of chemical or physical cues is then translated into altered channel gating, which in turn affects the currents through the nanopores (Bayley & Cremer, 2001). Because the unitary conductance of nanopores is generally high, conventional amplifiers can register any modulation of pore conductance and/or gating by the analyte of interest. The most prominent example of such a biotechnological application of conducting pores is the MinION device from Oxford Nanopore Technologies, which serves as a portable long-read DNA sequencing device (Fraiture et al., 2018). Since ion channels and protein nanopores are membrane proteins, they have to be embedded in a lipid bilayer to be functionally analyzed. There are many established electrophysiological techniques for measuring the activity of channels and nanopores in lipid bilayers in a cellular context or in vitro (Coronado & Latorre,1983; Hamill et al., 1981; Huxley, 2002; Iwamoto & Oiki, 2015; Lee et al., 2016; Hartel et al., 2018). Among these methods, the planar lipid bilayer (PLB) technique constitutes even 50 years after its invention (Müller et al., 1962; Montal & Müller, 1972) one of the most versatile methods for monitoring the activity of single ion channels and protein nanopores as well as their sensitivity to chemical and physical queues (Zakharian, 2013). Its key advantage over other electrophysiological approaches is that it allows recording of channel and pore activity on a true single molecule level under very reduced and defined conditions e.g. phospholipid composition and electrolyte concentrations. All this provides a range of experimental benefits. For example, it becomes possible to compare the functional features of a purified channel protein directly with the structural properties of the same isolated from crystallographic or cryo-EM structures. Another benefit of the bilayer technique relates to the fabrication of sensing devices. The literature reports multiple strategies for including miniaturized bilayer set-ups into portable sensing devices (Gu, 2009; Gu & Shim, 2010) or for multiplexing bilayers for high throughput analysis (Prokofyev et al., 2014; Kawano et al., 2011). An inherent disadvantage of the PLB technique concerns the incorporation of channel and pore proteins without contaminations into the bilayer and the mechanic instability of the lipid bilayer membrane. To overcome these shortcomings, many attempts were made over the past decades: In a recent study, we reported a new technique which allows efficient synthesis and incorporation of ion channel proteins into planar lipid bilayers (Winterstein et al., 2018). This approach combines in vitro translation of ion channels into nanodiscs followed by their direct reconstitution from the micro scaffolds into planar lipid bilayers. This procedure turned out to be a fast, efficient and

artifact-free method to reconstitute and measure ion channel activity in vitro (Winterstein et al., 2018). A number of studies have also provided technical solutions for improving the stability of the classical bilayer system (Gu, 2009; Tien et al., 1991; Mach et al., 2008; Kalsi et al., 2014). In conventional set-ups, the bilayer is formed over septa in Teflon or overhead transparency films (Winterstein et al., 2018; Bartsch et al., 2012; Williams, 1994). Also, cuvettes of monolithic polystyrene with locally thinned walls are used (Williams, 1994). The apertures in the respective septa, which host the lipid bilayer, are produced by rather crude methods including mechanical punching (Winterstein et al., 2018) or electrical sparks (Bartsch et al., 2012). The size of the resulting apertures, which are not under a good control of the experimenter, usually ranges between 50 and 200 µm in diameter (Kalsi, 2014; Sugawara & Hirano, 2005; Pantoja et al., 2001). These systems are well suited for experimental work, yet highly sensitive to mechanical disturbances. In our experience, most bilayers that have been formed over a Teflon septum with apertures >100 µm do not survive the exchange of a solution in one of the chambers by pipetting; this mechanic sensitivity generally confounds the routine characterization of channel functions and high throughput approaches. Another disadvantage associated with the large aperture concerns the high capacitance of the lipid bilayer membrane. The latter is a major source of noise in bilayer recordings and prevents the resolution of channel currents with small unitary currents or with high frequency gating (Hartel et al., 2018). Various micro-engineering techniques provide solutions to overcome the technical challenges associated with manufacturing small apertures of a well-defined size. This includes a range of mechanical and lithographic micro-fabrication approaches for producing small pores of defined size in a variety of materials (Kalsi, 2017; Pantoja et al., 2001; Castellana & Cremer, 2006; Groves et al., 1997; Cheng et al., 2001; Fertig et al., 2001; Peterman et al., 2002; Baaken et al., 2008; Buchholz et al., 2008). The basic message of these studies is that smaller apertures reduce the mechanical sensitivity in conventional bilayer recordings indeed while increasing the signal-to-noise ratio. Yet, smaller pores may in some cases also prevent the incorporation of channel proteins into miniaturized bilayers (Pantoja et al., 2001). In this work, we report a micromachining method for fabricating small and defined apertures in laminates of pre-cast epoxy thin dry film photosensitive polymer sheet ADEX (DJ MicroLaminates, Inc). ADEX foils with defined apertures can be used as septa in conventional bilayer set-ups, where they exhibit excellent properties for bilayer formation and stability. We observe that the electrical activity of a model K^+ channel is identical to recordings in Teflon foils, but resists mechanical perturbations that occur during buffer exchange. In addition, ADEX foils are chemically resistant to acetone. Therefore, the same septum can be cleaned and reused in subsequent recordings. This property and the ADEX foil photolithography-based fabrication method leads to a reusable well-defined aperture, which is accurately positioned on the foil surface. The chosen ADEX polymer is compatible with various microsystem fabrication and

manufacturing techniques, were a mass production of ADEX foils can be realized. Therefore, these ADEX foils can be integrated into reusable Lab-on-chip devices enabling the recording of multiple bilayers. We assume that this technique can improve electrical recordings in reconstituted lipid bilayer membranes.

4.3 Results and Discussion

Dry ADEX film sheets are suitable for fabricating complex apertures by photolithographic methods. To examine the application of these films as septum in planar lipid bilayer set-ups, we first measured the electrical properties of intact 50 µm thick ADEX foils. The latter were therefore sealed with silicone grease between two chambers of a planar lipid bilayer set-up (Bartsch et al., 2012). After filling the chambers with 100 mM KCl, a voltage ramp was applied across the ADEX foil to measure its electrical properties in the bilayer set-up (Fig. 4.1). With $Cc = I/(\Delta V/\Delta t)$ in which I is the initial current jump at the onset of the ramp and $\Delta V/\Delta t$ the slope of the voltage ramp we determine the capacitance Cc of the system. With intact ADEX foil in the bilayer set-up we obtained a value of 54 pF (54±1.1 pF, n=4) for (Cc) From the slope of the subsequent current response, a resistance (Rc) of 63 GΩ (mean 61±3; n=4) was estimated. The same experiments were performed with the usual 25 µm thick Teflon foil, which is routinely employed for bilayer recordings (Winterstein et al., 2018; Sugawara & Hirano, 2005). Based on measurements in 4 foils, we obtained a mean Cc value of 39±1 pF and a mean Rc of 588±179 GΩ. The results of these measurements show that, in the bilayer set-up, the ADEX foil has a lower resistance and approx. 1.5 times higher capacitance than a Teflon septum.

Next, we generated, as illustrated in Fig. 4.2, cylindrical pores with different diameters in ADEX foils. To visualize the geometry of these pores, film sheets with a single aperture were incubated in a solution with FITC and imaged on a confocal microscope. For comparison, the aperture in Teflon films generated by electric sparks (Bartsch et al., 2012) was imaged in the same manner. Representative examples of top and side views of both preparations are shown in Fig. 4.2. The large and small apertures in the ADEX foil are perfectly spherical and highly reproducible. The standard deviation of the mean pore diameter is < 5% of the pore size based on 4 foils prepared in the same manner. In contrast, Teflon-based apertures exhibit a larger variability around a mean diameter of 96.4 ±14 µm; the standard deviation is as large as 15% of the pore size based on 5 foils prepared in the same manner.

The cross section reveals that the apertures in ADEX foils have a slight cone shape in which the diameter on one side is approx. 10% smaller relative to the opposite rim. We can assign the

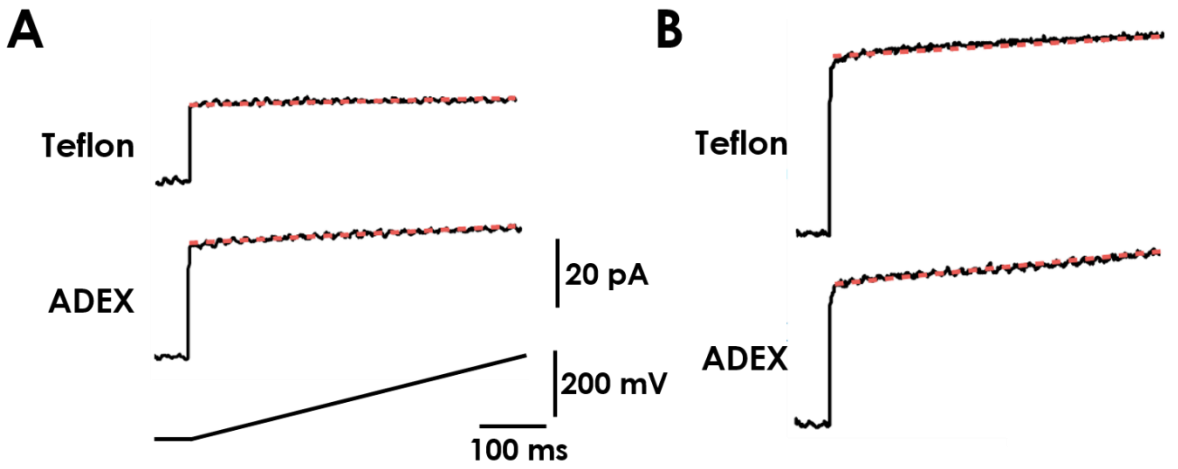

Figure 4.1: Capacitance and resistance of Teflon and ADEX foils. Intact Teflon or ADEX foils (A) or foils with approx. 100 µm large aperture (B) were sealed between two chambers of a planar lipid bilayer set-up. After filling both chambers with 100 mM KCl solution and after generating a stable DPhPC bilayer over the apertures in B, the current responses to a voltage ramp (lower trace) were measured. The initial current jump at the onset of the ramp is a measure for the capacitance. The resistance can be obtained from the slop (red line) of the current during the voltage ramp.

larger pore diameter to the side of the film that was exposed to the UV light in the lithographic preparation.

To examine the application of ADEX septa in planar lipid bilayer (PLB) recordings, we used foils with apertures of approx. 100 µm diameter; for comparison, apertures with similar dimensions were also generated by electric sparks in Teflon (Fig. 4.1). Both septa were positioned in conventional cuvettes for a vertical bilayer set-up (Bartsch et al., 2012). Planar lipid bilayers of DPhPC phospholipid were then generated with the painting or pseudo painting/air bubble technique (Müller et al., 1967; Braun et al., 2014b). After establishing a stable bilayer, the capacitance (Cp) and resistance (Rp) of single pores were measured in both systems from voltage ramps (Fig. 4.1). In case of ADEX septa, the Cp value was 57 pF (mean 57 ± 1 pF, n=4) (Fig. 4.1B) in a pore with a mean diameter of 102 ± 2 µm. To obtain the specific capacitance of the lipid bilayer (Cm) in the pore, the mean Cc value measured in Fig. 4.1A was subtracted from Cp and the remaining value normalized to the mean area of the pore. In this way, we can estimate a mean specific membrane capacitance Cm of 0.3 ± 0.01 µF/cm2 and 0.6 ± 0.02 µF/cm2 for bilayers in pores of approx. 100 µm diameter in ADEX and Teflon foils, respectively. The Cm value in Teflon is compatible with data reported for other bilayer systems including Teflon as septum (Winterstein et al., 2018; Sugawara & Hirano, 2005). The specific capacitance of the membrane in the ADEX foil is lower. One possible explanation for the lower capacitance could be due to the different geometry of the bilayer

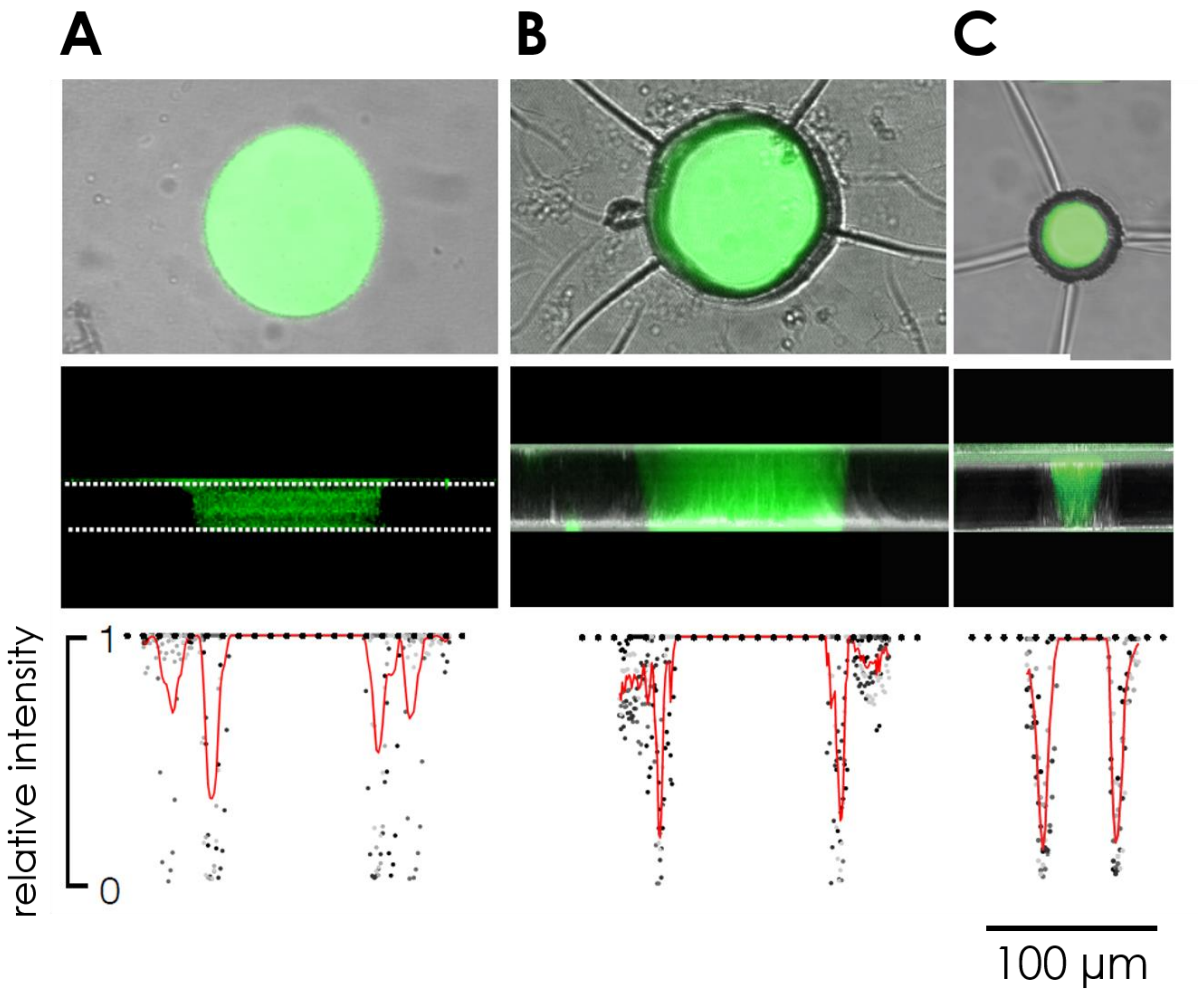

Figure 4.2: Imaging of apertures in Teflon and ADEX foils. The upper row shows a top view on single apertures in Teflon (A) and ADEX foils (B&C). Illustrated are overlays of bright field images (grey) with fluorescent images (green) from FITC in the pore. The central rows show the corresponding side view of the pores reconstructed from confocal scans of fluorescein fluorescence; the borders in the Teflon foil are indicated by dotted lines. The edges of the ADEX foil are visible from the self-reflection of the 633 nm laser, which does not occur in Teflon. The lower row reports data from individual intensity scans (grey points) and their mean values (red lines; $n \geq 4$) for the respective pores. The data were obtained by measuring the grey value along a line at the equator of single pores in a top view perspective. Grey values from different pores were normalized to the same ordinate. Scale bar is valid for all panels.

in the apertures in the ADEX films with a larger rim and a smaller effective bilayer. The results of these experiments indicate that the apertures in ADEX films carry both disadvantages (e.g. lower resistance) and advantages (e.g. lower specific capacitance) compared to similarly sized apertures in conventional Teflon films. ADEX septa are thus generally suited to host stable, free-standing planar lipid bilayers. Yet, because of inferior electrical properties, ADEX films will not necessarily improve the signal-to-noise ratio in ion channel recordings compared to Teflon foils.

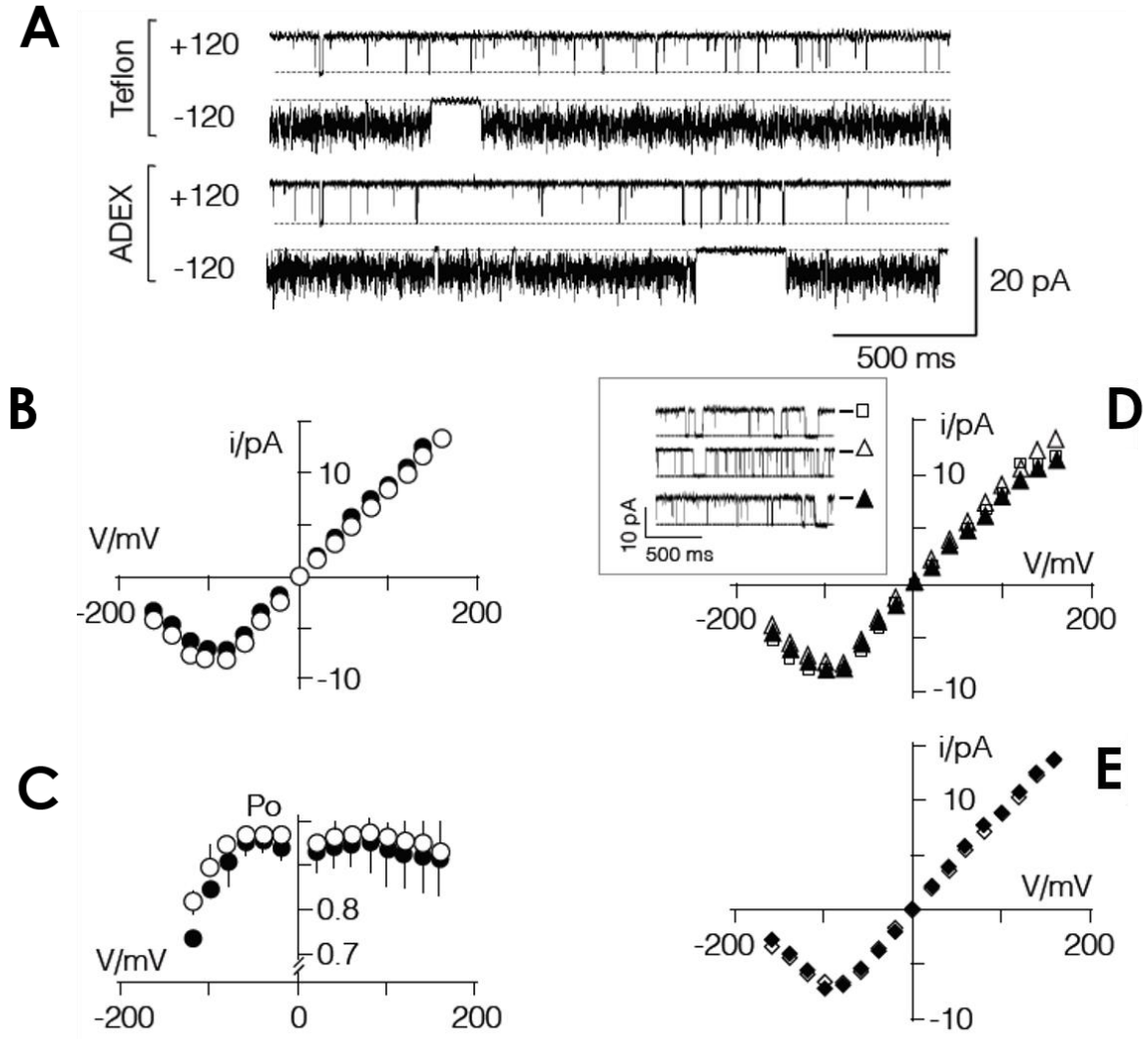

Figure 4.3: Comparative recordings of channel activity in septa from Teflon and ADEX films. (A) Typical channel fluctuations of Kcv_{NTS} channel at ±120 mV in symmetrical solution with 100 mM KCl. Data were measured in DPhPC bilayer painted over an aperture in Teflon (open circles) or ADEX (closed circles) foils with apertures of 100 µm and 50 µm respectively. (B) Mean I/V relation (± s.d.) of unitary Kcv_{NTS} currents from recordings as in (A) in Teflon (black circles; n=4) or in ADEX foil (open circles; n=3). (C) Mean open probability/voltage (P_o/V) relation (mean± s.d.) of Kcv_{NTS} channel from recordings as in (B). (D) I/V relations of Kcv_{NTS} channel reconstituted in bilayers in ADEX foils as in (A) with apertures of 100 (□) 50 (△) or 30 (▲) µm diameter; *inset*: representative current traces at -120 mV for three different apertures in ADEX foil. (E), I/V relations of Kcv_{NTS} channel in ADEX foil with 100 µm diameter as in A before (◆) and after (◇) cleaning septum in Acetone.

In subsequent experiments, we compared the functional properties of a reference K^+ channel, the small viral protein Kcv_{NTS} (Rauh et al., 2018), that has been reconstituted in lipid bilayers formed over ADEX- and Teflon-based septa. Representative recordings of single channel fluctuations in a DPhPC bilayer generated over an approx. 100 µm large hole in Teflon foil or over approx. 50 µm large hole in ADEX foil are shown in Fig. 4.3 In both cases, we measured the same type of channel activity. At positive voltages, the channel exhibits well-resolved channel openings and closings. At negative voltages of approx. -100 mV, the

unitary openings become increasingly noisy; the latter is caused by a typical fast gating at negative voltages, which cannot be resolved in conventional recording set-up (Rauh et al., 2018). From the unitary channel fluctuations, we constructed the current/voltage relation as well as the open probability/voltage in both recording conditions (Fig. 4.3B&C). A comparison of the data shows that the basic functional features of the K^+ channel can be measured in both recording set-ups and independently of the size of the aperture in the ADEX septum (Fig. 4.3B&D). It is also worth mentioning that the insertion of a channel into a bilayer formed over the ADEX septum occurs with the same bias as for a Teflon septum (Winterstein et al., 2018).

To test the stability of recordings in ADEX-based septa, measurements as in Fig. 4.4 were kept for as long as 48 h before they were actively terminated. In all cases, the recordings proceeded without experiencing any instability of the bilayer. This suggests that bilayers formed over ADEX septa are very stable. In a next set of experiments, we further examined the stability of channel recordings in ADEX- and Teflon septa. To this end, we periodically removed the medium in the *trans* chamber of the bilayer set-up. This operation generally destroys the bilayer over a Teflon septum (not shown). In other cases, the bilayer is first destroyed and then spontaneously reforming during the refilling of the measuring chamber. Since this newly formed bilayer does no longer contain the channel of interest (Fig. 4.4A) the procedure does not fulfill the purpose of a solution exchange.

The situation is very different for lipid bilayers formed over a septum in ADEX foil; the representative example in Fig. 4.4B shows that the chamber could be frequently emptied and refilled without compromising the quality of the bilayer. The results of these experiments demonstrate that lipid bilayer membranes formed over ADEX septa are mechanically much more stable compared to those in Teflon.

ADEX films are also resistant to acetone, which provides the possibility of cleaning them from lipids and proteins. To test the possibility of reusing ADEX septa for bilayer recordings, we measured channel activity as in Fig. 4.3 in an ADEX film with a 30 µm pore. The septum was then washed for 1 min with acetone, for 5 min with isopropanol and subsequently rinsed twice in distilled water. After painting a new bilayer over the aperture, the same type of K^+ channel was reconstituted and measured. The functional data, which are here represented by the unitary I/V relation in Fig. 4.3E, show no difference between the channel performance in fresh or recycled septum. The results of these experiments show that ADEX foils can be easily reused after cleaning with acetone for channel recordings, and provides a critical property for the design and handling of sensor devices based on ADEX foils.

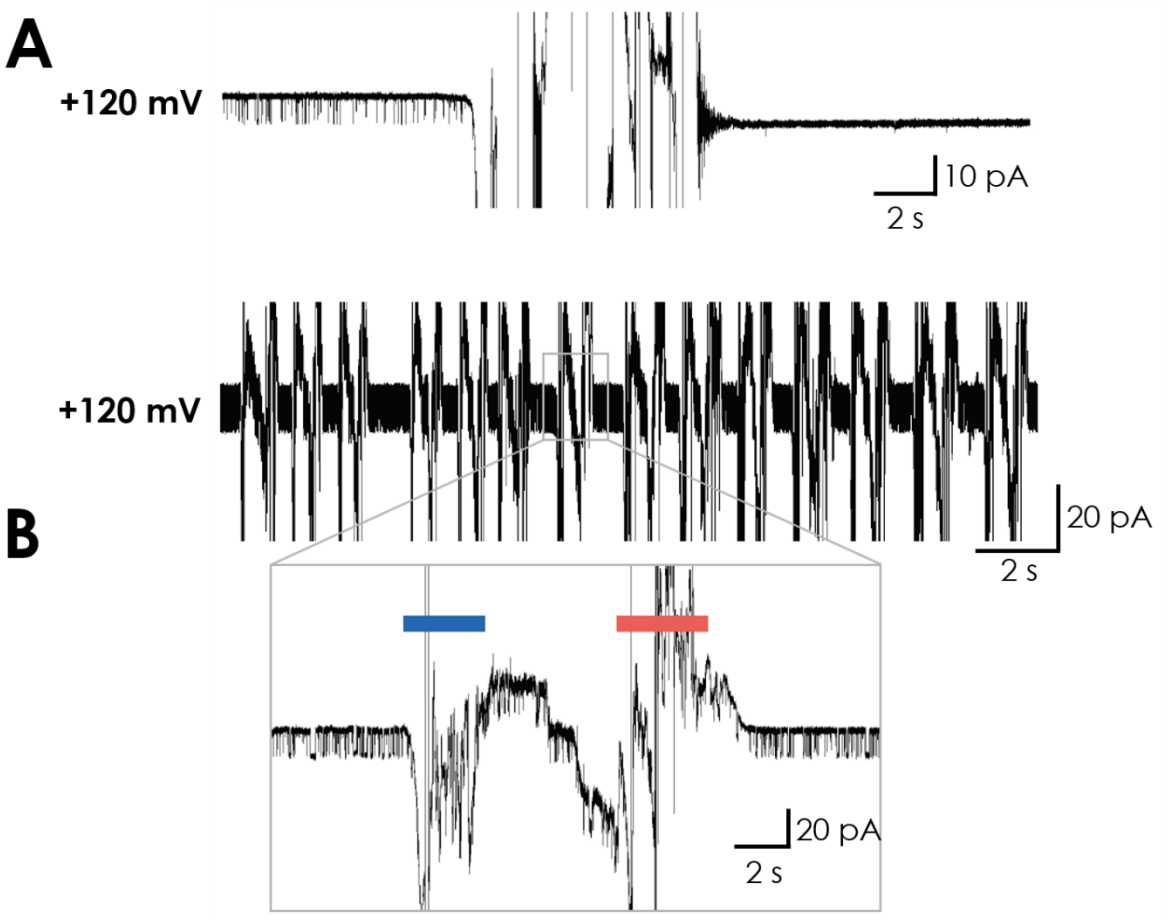

Figure 4.4: Sensitivity of bilayers in Teflon and ADEX septa to solution exchange. Continuous recordings of Kcv_{NTS} channel activity at +120 mV in symmetrical solution with 100 mM KCl in Teflon (A) and ADEX (B) foil. During the recording the solution of the *trans* chamber was removed and resupplied from a 5000 µl pipette. This procedure resulted in a destruction and reformation of the bilayer. While the original bilayer (left) exhibited an active channel the reformed bilayer (right) did not. The same procedure could be frequently repeated with the ADEX septum (B) without losing the bilayer with the active channel. One cycle of removing (blue bar) and resupplying of the solution (red bar) in B is magnified.

4.4 Conclusion

In conclusion we find that 50 µm thick ADEX foils provide a suitable material for micro-machining small and reproducible apertures by lithography. They can host stable membranes in conventional free-standing vertical planar lipid bilayers set-ups. Comparative analysis of channel activity reveals that the basic functional features of a model K^+ channel are indistinguishable between recordings in a conventional septum from Teflon or in ADEX films with different size apertures. The epoxy-based septa show no particular electrical advantage, which would improve the signal to noise ratio in channel recordings. But the material guarantees long lasting measurements of channel activity and allows an easy exchange of the buffer solution in the recording chambers without compromising the stability of the bilayer.

This stability of bilayers in ADEX septa together with the resistance of the material to acetone for cleaning and the quasi-unlimited possibility of fabricating complex apertures suggests that this material provides a promising basis for multiplexing septa in devices for high throughput bilayer recordings.

4.5 Methods

Preparation of single micropore epoxy films

The single micropore ADEX foils used in this work are fabricated from a 50 µm photoimageable thin-film resist made of epoxy (ADEX TDFS A 50). They are prepared as follows (Fig. 4.5): A layer of 7 µm thick photoresist (AZ® 9260) is deposited on a 100 mM Borosilicate glass substrate (Schott BOROFLOAT® 33) and baked for 20 min at 100 °C on a flat hotplate. After a soft bake, a layer of 200 nm Aluminum is sputtered on top of the wafer where it acts as a barrier between the AZ photoresist and the ADEX functional layer. The ADEX Layer is laminated on the Aluminum surface with a laminator (GBC HeatSeal ProSeries 3500LM) at a temperature of 75 °C and a lamination speed of 160 mm/min. The wafer is then baked for 5 min on a hot plate at 95 °C to eliminate material defects. To form the aperture foil, the ADEX polymer is in the next patterned by UV photolithography (200 mJ/cm2; wavelength: 365 nm). The exposed wafer is post-baked at 95 °C for 90 min with a heating and cooling ramp of 1 K/min. The ADEX is then developed with the SU-8 developer propylene glycol methyl ether acetate (PGMEA) for 10 min. To release the single pore ADEX film, the backside of the wafer is exposed to UV light (800 mJ/cm^2, wavelength: 436 nm); the sacrificial layer (AZ® 9260 + Aluminum) is then removed with the AZ® 400 K developer. The resist AZ® 9260 and the Aluminum are removed in the same step. The ADEX foils are subsequently cleaned with isopropanol and deionized water. The procedure is schematically summarized in Fig. 4.5.

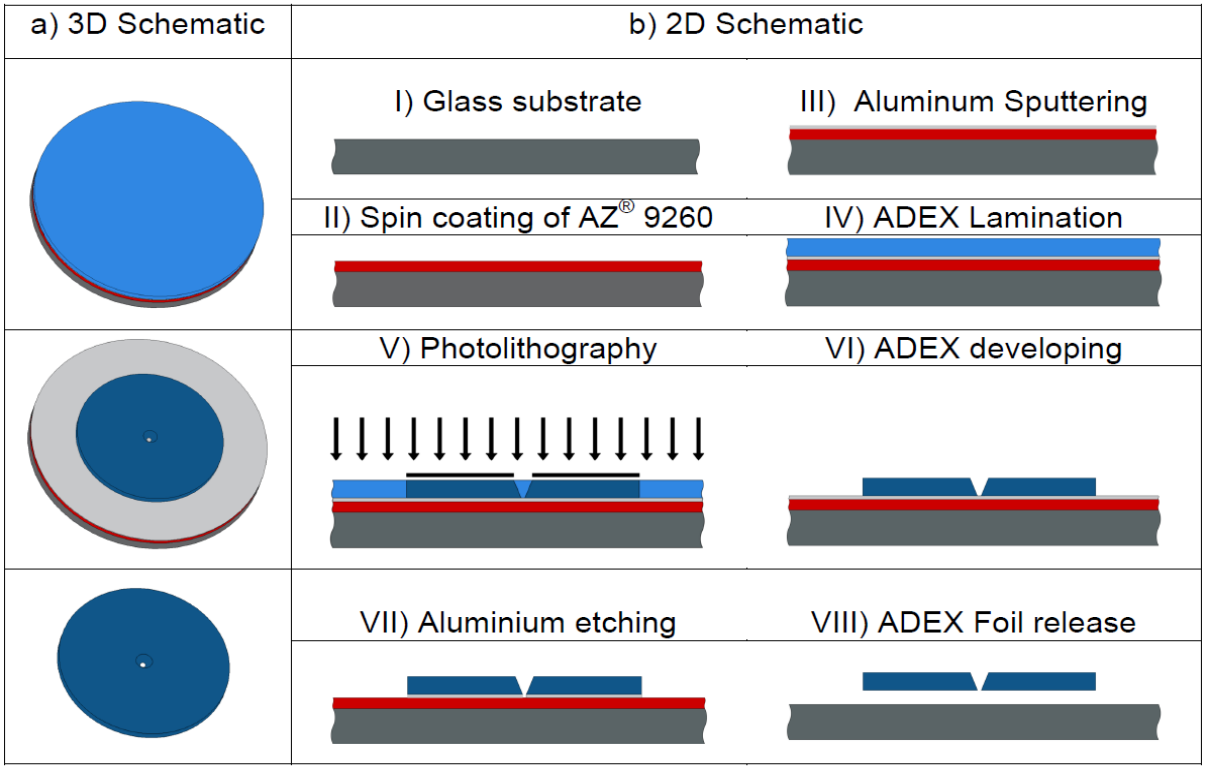

Figure 4.5: Microfabrication process for freestanding ADEX foils. (Step I) A Borosilicate glass substrate (Schott BOROFLOAT® 33) is cleaned with acetone and isopropanol; (Step II) A photoresist layer of 7 µm AZ® 9260 was applied on the substrate; (Step III) 200 nm Aluminum was sputtered on the photoresist; (Step IV) 50 µm ADEX layer was laminated on the Aluminum; (Step V) Photolithography: Exposure to UV light and post exposure bake of ADEX; VI) ADEX developing with PGMEA; VII) Backside exposure of AZ® 9260; VIII) ADEX foil is released: The Aluminum is etched and the photoresist AZ® 9260 is developed with AZ® 400K.

CLSM Measurements

Confocal laser scanning microscope (CLSM) measurements were performed on a LEICA TCS SP (Leica Microsystems, Mannheim, Germany) equipped with L20 x HCX APO 0.5 objective. For imaging of apertures in a foil, the latter was fixed with a thin agarose film support (1% in H2O) on the coverslips. The fluorescent probe Fluorescein isothiocyanate (FITC, 0.1 mg/mL in 8% EtOH) was added on top of the foil from where it was sucked *via* the pore into the agarose bed. Images were taken with a 488 nm laser (emission range of 510 nM – 530 nm) for FITC and a 633 nm laser (emission also 633 nm) for self-reflection of the foil surface. Analysis of the images was performed with Fiji – ImageJ (Schindelin et al., 2012).

Protein expression, purification

In vitro expression of the K^+ channel proteins was performed with the MembraneMax HN Protein Expression Kit (Invitrogen, Carlsbad, CA, USA) as described previously (Winterstein et al., 2018). The expression took place in the presence of different nanolipoproteins, so called nanodiscs (NDs). For the experiments described below, we used NDs provided with the commercial cell-free expression kit (MM, containing DMPC lipids) or MSP1D1-His discs ordered from Cube Biotech (Monheim, Germany). The latter were pre-assembled with DMPC, DMPG and POPC lipids. The scaffold proteins of all NDs were His-tagged to allow the purification of channel/NDcomplexes *via* metal chelate affinity chromatography. The concentration of MSP1D1- His NDs in the reaction mixture was adjusted to 30 µM. To purify the channel/ND-complexes, the crude reaction mixture was adjusted to 400 µL with equilibration buffer (10 mM imidazole, 300 mM KCl, 20 mM NaH_2PO_4, pH 7.4 with KOH) and subsequently loaded on an equilibrated 0.2 mL HisPur Ni-NTA spin column (Thermo Scientific). To allow the binding of the His-tagged NDs to the Ni- NTA resin, the columns were incubated for 45 min at room temperature and 200 rpm on an orbital *Shaker*. Afterwards the buffer was removed by centrifugation. To eliminate unspecific binders, the column was washed three times with 400 µL of a 20 mM imidazole solution. Finally, the His-tagged NDs were eluted in three fractions with 200 µL of a 250 mM imidazole solution. All centrifugation steps were performed at 700 g for 2 minutes.

Lipid bilayer experiments

Vertical lipid bilayer measurements were performed at RT (20-25°C) in 1,2-diphytanoyl-*sn*-glycero-3-phosphocholine (DPhPC, Avanti Polar Lipids, Alabaster, AL, USA) membranes in symmetrical potassium chloride solutions (100 mM KCl, 10 mM Hepes, pH 7). The recording chambers were prepared as described previously (Braun et al., 2014a&b). In the present experiments, the 25 µm thick Teflon septum was replaced by a 50 µm thick ADEX foil, which was prepared as described before. Lipid bilayers were formed inside the apertures in both types of septa by means of painting or pseudo painting/air bubble technique (Müller et al., 1967; Braun et al., 2014b). To incorporate channel proteins into the lipid bilayer, a small amount (~2 µL) of the purified channel/ND-conjugates was added directly below the bilayer in the *trans* compartment with a bent 25 µL Hamilton syringe (Hamilton Company, Rene, NV, USA). For the reconstitution of single channel proteins, the first elution fraction was diluted with a 250 mM imidazole solution by a factor of 10^3 to 10^6 (Winterstein et al., 2018). After channel incorporation in the lipid bilayer, constant voltages between +160 mV and -160 mV were applied for 10 seconds to several minutes. Both compartments of the bilayer chamber were

connected with Ag/AgCl electrodes to the headstage of a patch-clamp amplifier (L/M-EPC-7, List-Medical, Darmstadt, Germany). The electrode in the *trans* compartment served as ground. Currents were filtered with a 1 kHz 4-pole Bessel filter and digitized with a sampling frequency of 5 kHz by a 16-bit A/D-converter (LIH 1600, HEKA Elektronik, Lambrecht, Germany).

4.6 References

Ashcroft FM (2006) From molecule to malady. Nature 440:440–447. https ://doi.org/10.1038/natur e0470 7

Ayub A, Bayley H (2016) Engineering transmembrane pores. Curr Opin Chem Biol 34:117–126. https ://doi.org/10.1016/j. cbpa.2016.08.005

Baaken G, Sondermann M, Schlemmer C, Rühe J, Behrends JC (2008) Planar microelectrode-cavity array for high-resolution and par- allel electrical recording of membrane ionic currents. Lab Chip 8:938–944. https ://doi.org/10.1039/b8004 31e

Bartsch P, Walter C, Selenschik P, Honigmann A, Wagner R (2012) Horizon Bilayer Electr Opt Rec. Materials 5:2705–2730. https :// doi.org/10.1016/j.bbrc.2012.09.069

Bayley H, Cremer PS (2001) Stochastic sensors inspired by biology. Nature 413:226–230. https ://doi.org/10.1038/35093 038

Braun C, Lachnit C, Becker P, Henkes LM, Arrigoni C, Kast SM, Moroni A, Thiel G, Schroeder I (2014a) Viral potassium chan- nels as a robust model system for studies of membrane-protein interaction. Biochim Biophys Acta 1838:1096–1103. https ://doi. org/10.1016/j.bbame.2013.06.010

Braun C, Baer T, Moroni A, Thiel G (2014b) Pseudo painting/air bubble technique for planar lipid bilayers. J Neurosci Methods 233C:13–17. Doi. https ://doi.org/10.1016/j.jneum eth.2014.05.031

Buchholz K, Tinazli A, Kleefen A, Dorfner D, Pedone D, Rant U, Tampé R, Abstreiter G, Tornow M (2008) Silicon-on-insulator based nano- pore cavity arrays for lipid membrane investigation. Nanotechnology 19:445305. https ://doi.org/10.1088/0957-4484/19/44/44530 5

Castellana ET, Cremer PS (2006) Solid supported lipid bilayers: From biophysical studies to sensor design. Surf Sci Rep 61:429–444. https ://doi.org/10.1016/j.surfr ep.2006.06.001

Catterall WA, Wisedchaisri G, Zheng N (2017) The chemical basis for electrical signaling. Nat Chem Biol 13:455–463. https ://doi. org/10.1038/nchem bio.2353

Cheng Y, Bushby RJ, Evans SD, Knowles PF, Miles RE, Ogier SD (2001) Single ion channel sensitivity in suspended bilayers on microma- chined supports. Langmuir 17:1240–1242. https ://doi.org/10.1021/ la001 423h

Coronado R, Latorre R (1983) Phospholipid bilayers made from mon- olayers on patch-clamp pipettes. Biophys J 43:231–236. https ://doi. org/10.1016/S0006 -3495(83)84343 -4

Delcour AH (2002) Structure and function of pore-forming beta-barrels from bacteria. J Mol Microbiol Biotechnol 4:1–10. https ://doi. org/10.1038/natur e0470 7

Dilger JP, Benz R (1985) Optical and electrical properties of thin mono- olein lipid bilayers. J Membr Biol 85:181–189

Fertig N, Meyer C, Blick RH, Trautmann C, Behrends JC (2001) Micro- structured glass chip for ion-channel electrophysiology. Phys Rev E 64:040fcremer901. https ://doi.org/10.1103/PhysR evE.64.04090 1

Fraiture MA, Saltykova A, Hoffman S, Winand R, Deforce D, Vanneste K, De Keersmaecker SCJ, Roosens NHC (2018) Nanopore sequenc- ing technology: a new route for the fast detection of unauthorized GMO. Sci Rep 8:7903. doi. https ://doi.org/10.1038/s4159 8-018- 26259 -x

Groves JT, Ulman N, Boxen SG (1997) Micropatterning fluid lipid bilayers on solid supports. Science 275:651–653. doi. https ://doi. org/10.1126/scien ce.275.5300.651

Gu LQ (2009) A smart nanopore for bio-detection. ECS Trans 16:1–8. doi. https ://doi.org/10.1149/1.31047 04

Gu LQ, Shim JW (2010) Single molecule sensing by nanopores and nanopore devices. Analyst (Lond) 135:441–451. doi. https ://doi. org/10.1039/b9077 35a

Hamill OP, Marty A, Neher E, Sakmann B, Sigworth FJ (1981) Improved patch-clamp technique for high resolution current recordings from cells and cell- free membrane patches. Pflüg Arch Eur J Physiol 391:85–100

Hartel AJW, Ong P, Schroeder I, Giese MH, Shekar S, Clarke O, Marks AR, Hendrickson W, Shepard KL (2018) Ion channel recordings of the ryanodine receptor RyR1 at microsecond temporal resolu- tion. Proc Natl Acad Sci USA 115:1789–1798. doi. https ://doi. org/10.1073/pnas.17123 13115

Heginbotham L, LeMasurier M, Kolmakova-Partensky L, Miller C (1999) Single streptomyces lividans K+ channels: functional asymmetries and sidedness of proton activation. J Gen Physiol 114:551–560

Hille B (2001) Ion channels of excitable membranes, 3rd edn. Sinauer Associates Inc., Sunderland

Huxley A (2002) From overshoot to voltage clamp. Trends Neurosci 25:553–558

Iwamoto M, Oiki S (2015) Contact bubble bilayers with flush drainage. Sci Rep 5:9110. https ://doi.org/10.1038/srep0 9110

Kalsi S, Powl AM, Wallace BA, Morgan H, de Planque MRR (2014) Shaped apertures in photoresist film enhance the lifetime and mechanical stability of suspended lipid bilayers. Biohys J 106:1650– 1659. https ://doi.org/10.1016/j.bpj.2014.02.033

Kawano R, Tsuji Y, Sato K, Osaki T, Kamiya K, Hirano M, Ide T, Miki N, Takeuchi S (2013) Automated parallel recordings of topologi- cally identified single ion channels. Sci Rep 3: 1995. https ://doi. org/10.1038/srep0 1995

Kurachi Y, North A (2004) Ion channels: their structure, function and con- trol – an overview. J Physiol 554:245–247. https ://doi.org/10.1113/ jphys iol.2003.05770 3

Lee SW, Lee HH, Thiel G, Van Etten JL, Saraf RF (2016) Noninva- sive measurement of a single viral infection in a cell. ACS Nano 10:5123–1230. https ://doi.org/10.1021/acsna no.6b002 99

Mach T, Chimerel C, Fritz J, Fertig N, Winterhalter M, Fütterer C (2008) Miniaturized planar lipid bilayer: increased stability, low electric noise and fast fluid perfusion. Anal Bioanl Chem 390:841–846. https ://doi.org/10.1007/s0021 6-007-1647-7

Müller P, Rudin DO, Tien HT, Wescott WC (1962) Reconstitution of cell membrane structure in vitro and its transformation into an excitable system. Nature 194:979–980

Montal M, Müller P (1972) Formation of bimolecular membranes from lipid monolayers and a study of their electrical properties. Proc Natl Acad Sci USA 69:3561–3566

Pantoja R, Sigg D, Blunck R, Bezanilla F, Heath JR (2001) Bilayer recon- stitution of voltage-dependent ion channels using a microfabricated silicon chip. Biophys J 81:2389–2394. https ://doi.org/10.1016/ S0006 -3495(01)75885 -7

Peterman MC, Ziebarth JM, Braham O, Bayley H, Fishman HA, Bloom DM (2002) Ion channels and lipid bilayer membranes under high potentials using microfabricated apertures. Biomed Microdev 4:231–236

Prokofyev AV, Stimberg VC, Bomer JG, de Boer H, van den Berg A, Le Gac S (2014) Multiplexed microfluidic platform for electrophysi- ological measurements on ion channels in a unctional environment. In: 18th International Conference On Miniaturized Systems For Chemistry and Life Sciences, Microtas. pp 698–700

Rauh O, Hansen UP, Scheub DD, Thiel G, Schroeder I (2018) Site- specific ion occupation in the selectivity filter causes voltage- dependent gating in a viral K+ channel. Sci Rep 8:10406. https :// doi.org/10.1038/s4159 8-018-28751 -w

Schindelin J, Arganda-Carreras I, Frise E, Kaynig V, Longair M, Pietzsch T, Preibisch S, Rueden C, Saalfeld S, Schmid B, Tinevez JY, White DJ, Hartenstein V, Eliceiri K, Tomancak P, Cardona A (2012) Fiji: an open-source platform for biological-image analysis. Nat Methods 28:676–682. https ://doi.org/10.1038/nmeth .2019

Sugawara M, Hirano A (2005) Design and application of planar bilayer lipid membranes containing biological ion channels for chemical sensing. Adv Planar Lipid Bilayers Liposomes 1:221–245

Terstappen G, Roncarati R, Dunlop J, Peri R (2010) Screening technolo- gies for ion channel drug discovery. Future Med Chem 2:715–730. doi. https ://doi.org/10.4155/fmc.10.180

Tien HT, Salamon Z, Ottava A (1991) Lipid bilayer-based sensors and biomolecular electronics. Crit Rev Biomed Eng 18:323–340

Williams AJ (1994) An introduction to the methods available for ion channel reconstitution. In: Odgen DC (ed) Microelectrode tech- niques. The Company of Biologists, Cambridge

Winterstein LM, Kukovetz K, Rauh O, Turman DL, Braun C, Moroni A, Schroeder I, Thiel G (2018) Reconstitution and functional char- acterization of ion channels from nanodiscs in lipid bilayers. J Gen Physiol 150:637–646. https ://doi.org/10.1085/jgp.20171 1904

White SH (1985) The physical nature of planar bilayer membranes. In: Ion channel reconstitution, Miller C (ed) Plenum Press, New York. pp 3–35

Yu HB, Li M, Wang XL (2016) High throughput screening technolo- gies for ion channels. Acta Pharmacol Sin 37:34–43. https ://doi. org/10.1038/aps.2015.108

Zakharian E (2013) Recording of ion channel activity in planar lipid bilayer experiments. Methods Mol Biol 998:109–118. doi. https :// doi.org/10.1007/978-1-62703 -351-0_8

5 General Discussion

Viral potassium channels are small robust model systems. Despite their small size, they possess the fundamental properties of complex channel proteins involved in a variety of cellular and physiological processes. As a result, they are excellent for investigating structure function correlations. These include gating mechanisms and sensitivity to common blocking molecules. In this study Kcv_{ATCV-1} like K^+ channels were investigated regarding their block properties against quaternary ammonium cations.

QAs are a useful tool to examine viral K^+ channels

QA ions have been useful tools for the examination of the cytosolic K^+ channel pore opening and the cavity in the absence of crystallization data (Li & Aldrich, 2004; Jara-Oseguera et al., 2007; Piechotta et al., 2011).

In this work QAs were used to identify structural differences at the intracellular pore entrance and the cavity between the two viral potassium channels Kcv_S and Kcv_{NTS}. They differ by an additional inner gate in Kcv_S, which reduces the open probability due to longer closed phases (Rauh et al., 2017). Because of their small size and high hydrophobicity, it has not been possible to reveal the crystal structure of these channels. Thus, other methods have to be used for the resolving of structural differences.

The block by the different QAs is voltage dependent for both channels. Thus, the relative inhibition increases from near zero at negative voltages to almost 100% at positive voltages. In addition, the K_D values decrease at 100 mV with increasing blocker diameter. Surprisingly, the K_D values of TPeA and THxA are almost identical at Kcv_{NTS}. This phenomenon was observed in the K2P TRESK channel as well (Piechotta et al., 2011). Other K^+ channels do not show the same strong voltage dependence. For example, the TPeA block of the Kv channel *Shaker* Δ6-46 is only partially voltage dependent (Piechotta et al., 2011), which seems to be a general characteristic of Kv channels (Hille, 1992; Oliver et al., 1998). Also, the TRESK and TREK1, belonging to the family of K2P channels, show a voltage independent block (Piechotta et al., 2011). Kir channels and Ca^{2+}-activated channels, on the other hand, have a similar voltage dependence as Kcv channels, which suggests a similar architecture of the binding site (Guo & Lu, 2001; Villarroel et al., 1988).

Compared to each other, the voltage dependence of the different QAs in Kcv_{NTS} seems to be identical. The larger the blocker, the greater the affinity to the channel. The explanation for this can be found in the increasing hydrophobicity of bigger QAs. This allows them to bind more strongly within the hydrophobic binding pocket inside the cavity. This hypothesis is supported by the discovery of a hydrophobic pore in the KcsA channel (Doyle et al., 1998).

Furthermore, the results of this thesis show the significantly higher voltage dependence of the blocker dissociation compared to the association. Heginbotham & Kutluay (2004) have shown in experiments with other channels that the voltage-dependence of the block can be altered drastically by an interaction between the blocker and the permeant ions.

To address the question of an interaction of permeant ion and blocker, experiments were performed by Tobias Gabriel (Gabriel, 2018) with Kcv_{NTS} and TPrA under asymmetric KCl concentrations. These experiments show that an increase of the intracellular KCl concentration from 100 mM to 500 mM leads to a shift of the Nernst potential from 0 to -41.35 mV. After correcting the currents for differences in the driving force a reduction of the relative inhibition was observed for increased K^+ concentrations. In contrast, when the extracellular K^+ concentration was increased from 100 mM to 500 mM the reversal voltage shifted, as expected for a K^+ channel, to a positive value of 41.35 mV. However, in this condition no change in the relative inhibition was detectable. These experiments strongly suggest that the blocker and the K^+ ions compete for the same binding site, which is only accessible from the cytosolic side of the channel.

In further experiments, data from the block of Kcv_{NTS} with TPrA were used (Gabriel et al., in preparation). Here the voltage dependence of the block was compared with the probability that an ion is at the S4 site. Hence, the blocker is pushed away from its binding site from the charge of the next K^+ ion. In addition, the previous numerical determination of the ion occupation in the selectivity filter could be confirmed and can subsequently be used for predictions of computational models. This finding was already presumed in the last decade (Faraldo-Gómez et al., 2007).

The block by TEA shows an anomaly compared to the other QAs. Although it is one of the fast blockers which normally causes an apparent decrease of the amplitude, TEA also reduces the open probability. TEA should actually even increase the duration of bursts (Kutluay et al., 2005). Accordingly, TEA does not act like a strict open channel blocker. Either the channel can close around the blocker (Li & Aldrich, 2004), or the channel enters a second, long-lived, blocked state. Another possibility would be the presence of another binding site for TEA. In the *Shaker* K^+ channel, residue Thr^{441} is responsible for the TEA binding site (Heginbotham & MacKinnon, 1992). Mutations at this position lead to a reduction in TEA affinity. The homologous residue in Kcv_{NTS} is Thr^{45}. While KcsA T441S is significantly less sensitive than wt-KcsA (Yellen et al., 1991), Kcv_{NTS} T45S is even more affine to TEA than the wt-channel (not depicted). Accordingly, the binding site in Kcv channels is structurally different from KcsA.

In order to investigate the possibility of several binding sites for TEA in further experiments, one could first add TPrA intracellularly and afterwards TEA. With this method, it could be examined whether it is still possible to reduce the open probability by TEA after the block of

TPrA. If this experiment is positive, one could conclude that TEA can bind to the channel at two different positions.

The results presented in this work indicate that the quaternary ammoniums TEA, TPrA, TBA, TPA, and THxA interact with viral K^+ channels through different mechanisms, depending on the size of the blocker.

Comparing the affinity of the two viral K^+ channels it becomes clear that the affinity of Kcv_S towards the smaller QAs is significantly higher. The difference decreases with increasing molecular size. While the K_D values for TPrA at 100 mV are twice as high for Kcv_{NTS} as for Kcv_S, they are almost identical for TPeA. Reason for the difference are higher association and dissociation rates for Kcv_S because of structural differences due to the intrahelical hydrogen bond of Ser^{77} with the protein backbone. But these differences are of such small scale that only the block of small QAs is affected.

Kcv channels can be used for modular protein design

More than 50 years ago Armstrong & Binstock (1965) started investigating the effect of Tetraethylammonium (TEA) on potassium channels. By using TEA, it was found that the extracellular and intracellular sides of potassium channels must differ from each other. The squid axon reacted differently depending on which side was exposed to TEA. In the following decades, TEA was increasingly used to measure the overall pore length (Coronado & Miller, 1982) or to investigate the slow inactivation of voltage-dependent K^+ channels (Choi et al., 1991). While all QAs can block ion channels from the intracellular side, only TEA is able to specifically block potassium channels extracellularly. Mutagenesis studies demonstrated that the amino acid residue at *Shaker* position 449 had a dramatic impact on the blocking potency of external TEA (MacKinnon & Yellen, 1990). All four subunits form a kind of pocket at this position, which has an ideal dimension for TEA (Heginbotham & MacKinnon, 1990). The two similar sized molecules TMA and TPrA, however, are not able to fit into this pocket to block ion current through the channel pore (Villarroel et al., 1988; Meuser et al., 1999).

Most studies on external TEA were conducted in the 1980s and 1990s. Since viral potassium channels first became known after the turn of the millennium (Plugge et al., 2000), there are barely any studies on the sensitivity of viral K^+ channels against TEA. Tan et al. (2012) tuned the sensitivity of $Kcv_{PBCV\text{-}1}$ with point mutations at the extracellular pore entrance identical to *Shaker* 449. Concerning ATCV-1 like channels, measurements by Greiner (2011) exist, which attests Kcv_{NTS} only a low sensitivity to TEA. The reason for this is a variation in the amino acid responsible for TEA sensitivity. By mutating Thr^{53} to Leu, Kcv_{NTS} shows a significant increase in sensitivity to TEA. Leu is likely to ensure an optimal conformation of the extracellular mouth that confers high TEA affinity. However, this mutation leads to a drastically reduced single channel conductivity.

According to Rauh et al. (2018), the reduced amplitude could be increased by replacing the Ser^{42} to Thr. The conductance is 60% higher at positive voltages than for the wt-channel. Furthermore, an increase of the open probabilities after the addition of external TEA can be observed for this mutant. The reason for this is the temporal reduction of the interburst phases. Through a kind of foot-in-the-door mechanism, TEA is able to compensate these longer closed events, which could be a kind of C-type inactivation. It was not possible to deal with this phenomenon in detail during this work. However, it would be worthwhile to investigate it more closely, since C-type inactivation is untypical for viral potassium channels. In addition, other studies have already identified amino acids that lead to long interburst phases (Rauh et al., 2018).

Particularly to the family of the ATCV-1 belong a large variety of channels, which differ mostly only by few amino acids (Siotto et al., 2017). Due to their small size, these differences usually have only a minor influence on the channel properties. Therefore, if there are differences, they can be directly assigned to a certain structure within the protein. In the past, specific electrophysiological properties could therefore be assigned to individual amino acids. To name a few examples, the mutation S77G in Kcv_S leads to a dramatic increase of the mean open probability (Rauh et al., 2017). Kcv_{NH} S42T increases single channel conductivity enormously (Rauh et al., 2018). If Asn^{28} in Kcv_{NH} is replaced with a Tyr, it gets an outward rectifier (D'Arco, 2016). If one would like to express a viral potassium channel in E. coli, the insertion into the membrane is toxic for the bacteria. Kcv_{NH} can be almost completely inactivated by a point mutation (Rösser, 2017). Thus, significantly more bacteria would survive despite the insertion of a functional channel into the membrane.

As a result, there is now a kind of database of many members of this family. This database illustrates which amino acid generates or is responsible for which properties. This knowledge can thereafter be used as a toolkit, just like in this work. If an experiment requires a K^+ channel with very specific properties, it is now possible to assemble it using the database.

Despite all positive previous experiments, it was not possible to switch Kcv_{NTS} by light. Firstly, using mass spectrometry, the mass of the MAL-AZO-QA molecule was confirmed. As a result, the conformation should be correct, too. Secondly, it was investigated whether the used LEDs were sufficient to photoisomerize the molecule. With UV-Vis spectroscopy this could be confirmed. The spectra display the two characteristic peaks as illustrated by Banghart et al. (2004). Thirdly, it was possible to perform photoisomerization inside the bilayer chamber. The open channel noise changed after irradiation with the 380 nm LED. Finally, also the maleimide coupling inside the bilayer chamber with N-ethylmaleimide confirmed the hypothesis that this required reaction is possible.

Why the MAL-AZO-QA did not bind to the channel could not be clarified. Perhaps the chosen distance between the maleimide binding site of the loop and the TEA binding site of

the pore entrance was not optimal. Due to the small size of Kcv_{NTS}, the loop could also not rise far enough out of the membrane, which could have made coupling impossible (Braun et al., 2014).

References

Armstrong C.M., L. Binstock (1965) Anomalous rectification in the squid giant axon injected with tetraethylammonium chloride. *J Gen Physiol 48 (5), 859–872.*

Banghart M., K. Borges, E. Isacoff, D. Trauner, and R. H. Kramer (2004) Light-activated ion channels for remote control of neuronal firing. *Nat Neurosci.*, *7*(12), 1381–1386.

Braun C. J., C. Lachnit, P. Becker, L. M. Henkes, C. Arrigoni, S. M. Kast, A. Moroni, G. Thiel, and I. Schroeder (2014) Biochimica et Biophysica Acta Viral potassium channels as a robust model system for studies of membrane – protein interaction ☆ , ☆☆. *BBA - Biomembr.*, *1838*(4), 1096–1103.

Choi K. L., R. W. Aldricht, and G. Yellen (1991) Tetraethylammonium blockade distinguishes two inactivation mechanisms in voltage-activated Ki channels. *Proc. Natl. Acad. Sci U.S.A.*, *88*(June), 5092–5095.

Coronado R., and C. Miller (1982) Conduction and block by organic cations in a K1-selective channel from sarcoplasmic reticulum in- corporated into planar bilayer membranes. *J. Gen. Physiol. 79:529–547.*

D'Arco F. (2016) Viral K + channels Kcv NH and Kcv NH S77G : Investigation of their gating mechanism. *Master Thesis Tech. Univ. Darmstadt.*

Doyle D. A., J. Morais Cabral, R. A. Pfuetzner, A. Kuo, J. M. Gulbis, S. L. Cohen, B. T. Chait, and R. MacKinnon (1998) The structure of the potassium channel: molecular basis of K+ conduction and selectivity. *Science*, *280*(5360), 69–77.

French R. J., and J. J. Shoukimas (1981) Blockage of squid axon potassium conductance by internal tetra-N-alkylammonium ions of various sizes. *Biophys. J.*, *34*(2), 271–291.

Gabriel T. (2018) Measurement of the Kcv NTS inner gate diameter with quaternary ammonium. *Master Thesis Tech. Univ. Darmstadt.*

Gazzarrini S., M. Severino, M. Lombardi, M. Morandi, D. DiFrancesco, J. L. Van Etten, G. Thiel, and A. Moroni (2003) The viral potassium channel Kcv: Structural and functional features. In *FEBS Letters* (Vol. 552, pp. 12–16).

Greiner T. (2011) Characterization of novel potassium transport proteins from Chlorella viruses. *Diss. Tech. Univ. Darmstadt.*

Guo D., and Z. Lu (2001) Kinetics of inward-rectifier K+ channel block by quaternary alkylammonium ions. dimension and properties of the inner pore. *J. Gen. Physiol.*, *117*(5), 395–406.

Heginbotham L., and E. Kutluay (2004) Revisiting Voltage-Dependent Relief of Block in Ion Channels : A Mechanism Independent of Punchthrough. *Biophys. J.*, *86*(6), 3663–3670.

Heginbotham L., and R. MacKinnon (1992) The aromatic binding site for tetraethylammonium ion on potassium channels. *Neuron*, *8*(3), 483–491.

Hille B (1992) Ionic channels of excitable membranes, *2nd ed. Sinauer Associates, Sunderland, Mass.*

Jara-Oseguera A., I. Llorente, T. Rosenbaum, and L. D. Islas (2008) Properties of the Inner Pore Region of TRPV1 Channels Revealed by Block with Quaternary Ammoniums. *J. Gen. Physiol.*, *132*(5), 547–562.

Kutluay E., B. Roux, and L. Heginbotham (2005) Rapid intracellular TEA block of the KcsA potassium channel. *Biophys. J.*, *88*(2), 1018–1029.

Li W., and R. W. Aldrich (2004) Unique Inner Pore Properties of BK Channels Revealed by Quaternary Ammonium Block. *J. Gen. Physiol.*, *124*(1), 43–57.

MacKinnon R., and G. Yellen (1990) Mutations Affecting TEA Blockade and Ion Permeation in Voltage-Activated K + Channels m). *Sciene*, *250*(4978), 276–279.

Meuser D., H. Splitt, R. Wagner, and H. Schrempf (1999) Exploring the open pore of the potassium channel from Streptomyces lividans. *FEBS Lett.*, *462*(3), 447–452.

Oliver D., H. Hahn, C. Antz, J.P. Ruppersberg, B. Fakler (1998) Interaction of permeant and blocking ions in cloned inward-rectifier K+ channels. *Biophysical Journal 74 (5), 2318–2326. 10.1016/S0006-3495(98)77941-X.*

Piechotta P.L., M. Rapedius, P.J. Stansfeld, M.K. Bollepalli, G. Ehrlich, I. Andres-Enguix, H. Fritzenschaft, N. Decher, M.S.P Sansom, S.J. Tucker, T. Baukrowitz (2011) The pore structure and gating mechanism of K2P channels. *The EMBO journal 30 (17), 3607–3619. 10.1038/emboj.2011.268.*

Plugge B., S. Gazzarrini, M. Nelson, R. Cerana, J. L. Van Etten, C. Derst, D. Difrancesco, and A. Moroni (2000) R EPORTS Encoded by Chlorella Virus PBCV-1. *Science (80-.).*, *287*(March), 1641–1644.

Rauh O., U. P. Hansen, D. D. Scheub, G. Thiel, and I. Schroeder (2018) Site-specific ion occupation in the selectivity filter causes voltage-dependent gating in a viral K+channel. *Sci. Rep.*, *8*(1), 1–15.

Rauh O., M. Urban, L. M. Henkes, T. Winterstein, T. Greiner, J. L. Van Etten, A. Moroni, S. M. Kast, G. Thiel, and I. Schroeder (2017) Identification of Intrahelical Bifurcated H-Bonds as a New Type of Gate in K+Channels. *J. Am. Chem. Soc.*, *139*(22), 7494–7503.

Rösser S. (2017) Influence of the outer pore mouth on the voltage dependence of the viral potassium channel Kcv NH. *Bachelor Thesis Tech. Univ. Darmstadt.*

Siotto F., C. Martin, O. Rauh, J. L. Van Etten, I. Schroeder, A. Moroni, and G. Thiel (2014) Viruses infecting marine picoplancton encode functional potassium ion channels. *Virology*, *466–467*, 103–111.

Tan Q., B. Ritzo, K. Tian, and L.-Q. Gu (2012) Tuning the tetraethylammonium sensitivity of potassium channel Kcv by subunit combination. *J. Gen. Physiol.*, *139*(4), 295–304.

Villarroel A., O. Alvarez, A. Oberhauser, R. Latorre (1988) Probing a Ca2+-activated K+ channel with quaternary ammonium ions. Pflugers Archiv: *European journal of physiology 413 (2), 118–126.*

Yellen G., M. E. Jurman, T. Abramson, and R. MacKinnon (1991) Mutations affecting internal TEA blockade identify the probable pore-forming region of a K+ channel. *Science*, *251*(4996), 939–942

6 Appendix

Table 6.1: Size of tetraalkylammonium ions presented as diameters. The diameter values for the cations are the doubled corresponding radii values. Ion diameter for QAs (Lagowski, 1976; Robinson & Stokes, 1959). Stokes diameter and standard partial molar diameter calculated with values and formulas from (Bondi, 1964; King, 1970; Marcus, 2008). ~ symbolizes that these values were calculated with fit-functions.

abbreviation	estimated ion diameter in Å	Stokes diameter in Å	std. partial molar diameter in H_2O in Å
TMA	6.94	2.68	6.44
TEA	8	4.12	7.69
TPrA	9.04	5.66	8.72
TBA	9.88	7.88	9.5
TPeA	10.58	9.54	10.19
THxA	11.22	10.58	~10.79
THpA	11.78	~11.36	~11.33
TOA	~14.29	~10.62	~11.82

Table 6.2: Solubilities of different QA chlorides. The solubility values in 0.1 M KCl solution were calculated with solubility products for the QA chlorides. The solubility products were calculated by simply squaring the QACl solubilities in water in accordance with their dissociation stoichiometries (only concentrations and no activities were used for calculation).

abbreviation	Solubility in M	Solubility in 0.1 M KCl in M	Source
$TMA^+ Cl^-$	19.06	19.01	(Lindenbaum & Boyd, 1964)
$TEA^+ Cl^-$	9.47	9.42	(Lindenbaum & Boyd, 1964)
$TPrA^+ Cl^-$	19	18.95	(Nakayama, 1981)
$TBA^+ Cl^-$	20.53	20.48	(Nakayama, 1981)
$TPeA^+ Cl^-$	40.2	40.15	(Nakayama, 1981)
$THxA^+ Cl^-$	0.088	0.051	(Nakayama et al., 1989)
$THpA^+ Cl^-$	$7.0*10^{-4}$	$4.8*10^{-6}$	(Dubini-Paglia et al., 1970)
$TOA^+ Cl^-$	$5.7*10^{-4}$	$3.2*10^{-6}$	(Nakayama et al., 1989)

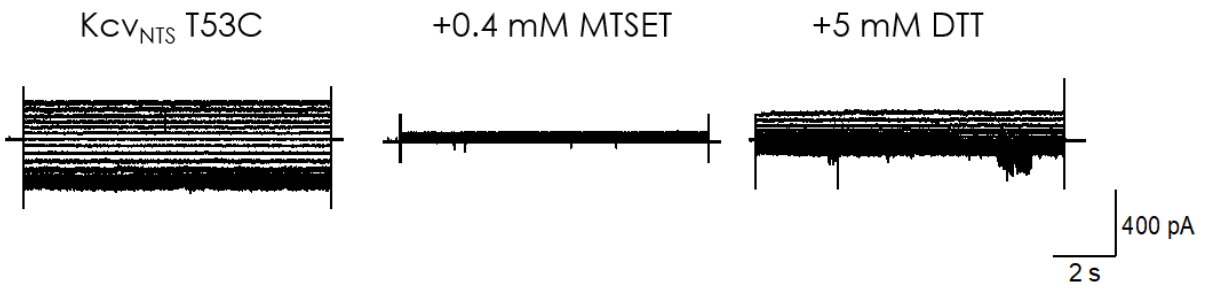

Figure 6.1: Orientation of Kcv channels in planar lipid bilayers. Raw data of I/V relations from multichannel measurements of Kcv$_{NTS}$ T53C in Fig 2.2D. MTSET blocks the channel when added into the *trans* chamber. With DTT, the block can be disrupted.

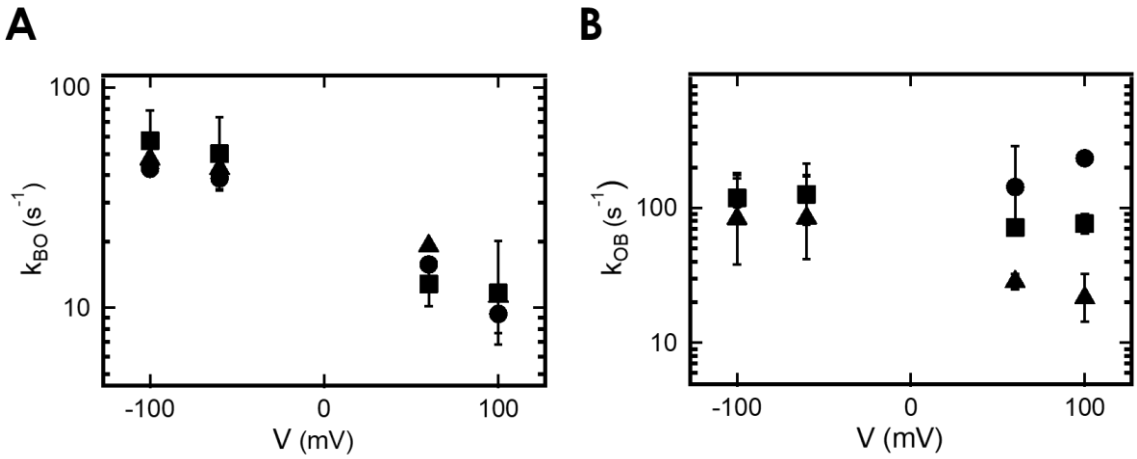

Figure 6.2: Kinetics of TPeA block of Kcv$_S$. (A) Dissociation rate (k_{BO}) and (B) Association rate (k_{OB}) of block with different TPeA concentrations determined from fits of dwell-time histograms. The concentrations are 50 nM (triangles), 100 nM (squares), and 1 µM (circles). Mean data ± s.d. are from 3 independent recordings. The dissociation is concentration independent, while the association depends on the blocker concentration. Besides that, only k_{BO} is voltage dependent.

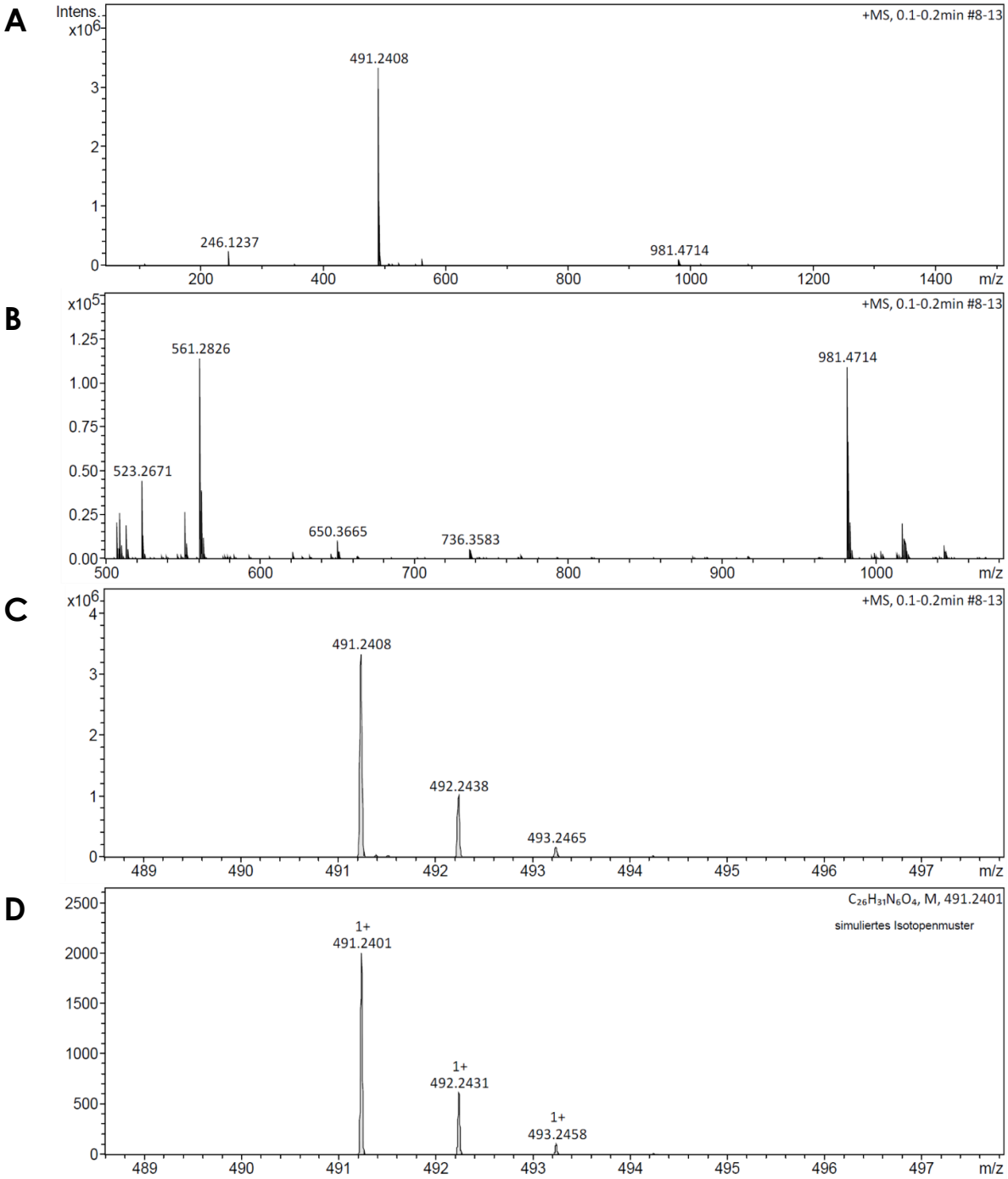

Figure 6.3: Complete mass spectrum of MAL-AZO-QA. (A) Measured isotope distribution of the sample containing the synthesized MAL-AZO-QA molecule. (B) Enlarged version of contamination at 500 m/z and above. (C) Enlarged version of the molecule peak at 490 m/z. (D) Simulated isotope distribution. Shown are the intensities above the mass per charge.

List of abbreviations

Å	Ångstöm
A/D	analog/digital
ATCV-1	Acanthocystis turfacea chlorella virus 1
BK	Big K^+ channel
C	closed state
C. elegans	Caenorhabditis elegans
ddH_2O	double-distilled water
DH5α	E. coli strain useful for recombinant DNA methods
DNA	desoxyribonucleic acid
DPhPC	1,2-diphytanoyl-sn-glycero-3-phosphocholine
DTT	dithiothreitol
e	Euler´s number (e ≈ 2.718)
E. coli	Escherichia coli
ec	extracellular
HEPES	4-(2-hydroxyethyl)-1-piperazineethanesulfonic acid
i	open-channel amplitude
I	macroscopic current
ic	intracellular
k	rate constant
$[K^+]$	potassium concentration
Kcv	K^+ channel chlorella virus
KcsA	K^+ channel from Streptomyces lividans
K_D	apparent dissociation constant
Kir	inwardly rectifying K^+ channel
KirBac	bacterial inwardly rectifying K^+ channel
Kv	voltage-gated K^+ channel
K2P	two-pore domain K^+ channel
N	number of experiments or number of events
NLP	nanolipoprotein
O	open state
P	probability of occupancy
PCR	polymerase chain reaction
PBCV-1	Paramecium bursaria chlorella virus 1
pH	potential of hydrogen
QA	quaternary ammonium

rpm	rounds per minute
s.d.	standard deviation
std.	standard
t	time
T	absolute temperature
TAA^+	Tetraalkylammonium cations
TBA^+	Tetrabutylammonium
TEA^+	Tetraetylammonium
$THpA^+$	Tetraheptylammonium
$THxA^+$	Tetrahexhylammonium
TMA^+	Tetrametylammonium
TOA^+	Tetraocthlammonium
$TPeA^+$	Tetrapentylammonium
$TPrA^+$	Tetrapropylammonium
TM	transmembrane
τ	time constant
V	voltage
wt	wildtype

Amino acids and codes

Alanine	A	Ala
Arginine	R	Arg
Asparagine	N	Asn
Aspartic acid	D	Asp
Cysteine	C	Cys
Glutamine	Q	Gln
Glutamic acid	E	Glu
Glycine	G	Gly
Histidine	H	His
Isoleucine	I	Ile
Leucine	L	Leu
Lysine	K	Lys
Methionine	M	Met
Phenylalanine	F	Phe
Proline	P	Pro
Serine	S	Ser
Threonine	T	Thr
Tryptophan	W	Trp
Tyrosine	Y	Tyr
Valine	V	Val

Own work

Experiments, data analysis and writing were exclusively done by myself, with exception of:

- The generation of the channel mutant Kcv_{NTS} T53C by site-directed mutagenesis (section 2.3) was performed by Oliver Rauh.
- The single-channel measurements of the viral potassium channel Kcv_{NTS} with TPrA, TPeA and THxA in section 2.3 were performed by Tobias Sebastian Gabriel (Master student) under my supervision.
- The beta-distribution analysis in section 2.3 was performed by Ulf-Peter Hansen (CAU Kiel) and Indra Schroeder.
- The generation of the channel mutants and Kcv_{NTS} S42T T53L, M25C S42T T53L, S26C S42T T53L, and F27C S42T T53L by site-directed mutagenesis and their electrophysiological examination (section 3.3) were performed by René Lautenschläger (Master student) under my supervision.
- Fabrication of the ADEX foils, which were used in El Khoury et al., (2018) The Journal of Membrane Biology https://doi.org/10.1007/s00232-019-00062-9, were performed by Mario El Khoury. The CLSM measurements and the analysis of the images were performed by Wadim Weber. Prof. Gerhard Thiel contributed to the design of experiments and interpretation of data. Prof. Gerhard Thiel, Prof. Viktor Stein, and Prof. Helmut F. Schlaak supported writing of the manuscript.

Declaration – Ehrenwörtliche Erklärung

Ich erkläre hiermit ehrenwörtlich, dass ich die vorliegende Arbeit entsprechend den Regeln guter wissenschaftlicher Praxis selbstständig und ohne unzulässige Hilfe Dritter angefertigt habe.

Sämtliche aus fremden Quellen direkt oder indirekt übernommenen Gedanken sowie sämtliche von Anderen direkt oder indirekt übernommenen Daten, Techniken und Materialien sind als solche kenntlich gemacht. Die Arbeit wurde bisher bei keiner anderen Hochschule zu Prüfungszwecken eingereicht.

Darmstadt, den ……

.....

Tobias Winterstein

Acknowledgements – Danksagung

An dieser Stelle möchte ich mich bei allen Personen bedanken, die mich in den letzten Jahren unterstützt haben. Mein besonderer Dank gilt:

Prof. Dr. Gerhard Thiel, für die Bereitstellung dieses Themas, die Freiheit eigenen Ideen nachzugehen, die freundliche Unterstützung und den offenen Umgang.

Prof. Dr. Adam Bertl, für die Übernahme des Koreferats

PD Dr. Indra Schröder, für die unendlichen Befreiungen aus jeglichen verzweifelten Lagen im Labor und am Schreibtisch, sogar während der Rettung deiner eigenen wissenschaftlichen Karriere.

Prof. Dr. Ulf-Peter Hansen, für die Auswertung, die Korrekturen dieser Arbeit und die Strukturierung des Chaos.

Barbara Reinhards und **Tanja Musielak** für die Erledigung des bürokratischen Wahnsinns dieser Welt.

Dr. Brigitte Hertel, **Brigitte Hehl**, **Silvia Haase**, **Sylvia Lenz**, **Mirja Manthey** und **Ulrike Burk** für den organisierten und funktionierenden Laboralltag.

René Lautenschläger und **Tobias Gabriel**, die als meine beiden Masterstudenten Unmengen an Daten erhoben und ausgewertet haben.

Dr. Oliver Rauh, **Dr. Laura-Marie Winterstein**, **Tobias Schulze** und **Dominique Tandl,** für die Unterstützung und die Beantwortung von Fragen aller Art während der Zeit im Labor und beim Schreiben.

Dem restlichen alten und neuen **Kinderzimmer** für die angenehme Arbeitsatmosphäre, auch wenn man zum "Arbeiten" besser Home-Office gemacht hat.

Kerri Kukovetz und **Sebastian Mach** für die *locker-easy* Zeit am Bilayer. 🤌

Robert Lehn und **Alex Krömmelbein** für die Versüßung der Pausen.

Der gesamten **AG Thiel** für die schöne Zeit, die Kegelabende, das wöchentliche Kicken und natürlich für Bier um 4.

Allen die bei ***iNAPO*** mitgewirkt haben, vor allem **Wadim Weber**, **Mario El Khoury**, **Robert Brilmayer**, **Lena Müller**, **Ivana Duznovic** und **Sarah Schneider** für die gemeinsamem Experimenten, die Stammtische und die Klassenfahrt nach Bremen.

Meine Eltern **Sylvia** und **Detlef Winterstein**, für die fortwährende Hilfe und Unterstützung.

Meiner Verlobten **Steffi Korn**; Danke, dass du immer für mich da bist!